

**A Study on the Relaxation Phenomena and Pattern Formation  
of Nematic Polymers after Cessation of Shear Flow**

by

**Philip Kwok-Kiou Chan**

**Department of Chemical Engineering**

**McGill University, Montreal**

**August 1992**

**A Thesis submitted to the Faculty of Graduate Studies and Research**

**in partial fulfillment of the requirements of the degree of**

**Master of Engineering**

**© Philip Chan, 1992**

**Shortened version of thesis title:**

**Relaxation Phenomena of Nematic Polymers after Cessation of Shear Flow**

**by Philip Kwok-Kiou Chan**

## Abstract

Nematic polymers are a new class of advanced materials that have excellent mechanical properties because of their anisotropic structure. Successful manufacturing of high performance materials from these polymers depends on control of molecular orientation. A crucial step is then to understand the relaxation phenomena after cessation of shear flow deformations.

The first part of this thesis studies numerically the effects that the surface conditions, defects and backflow have on the relaxation phenomena after cessation of simple shear flow for a typical rigid rod nematic polymer. The Leslie-Ericksen continuum theory and the Euler-Lagrange equations for surface motion are derived and used for this purpose. Predictions are found to be physically consistent.

Nematic polymers, under certain conditions, develop a transient banded texture after cessation of shear flow when observing the sheared sample between crossed polars. The second part of this thesis presents a viscoelastic model that describes the formation mechanism of this well characterized but yet unexplained phenomenon for a typical rigid rod nematic polymer. This model is composed of the Ericksen and Landau-de Gennes continuum theories, and predicts that the relaxation of periodic spatial variations of the scalar order parameter produces spatially periodic torques on the director. Consequently, a transient banded texture is seen when viewing the sample between crossed polars. The numerical results and digitized optical patterns are in good agreement with reported experimental observations, and are used to explain these observations.

## Résumé

Les polymères nématiques sont une nouvelle classe de matériaux perfectionnés présentant d'excellentes propriétés mécaniques dues à leur structure anisotrope. La réussite de la fabrication de matériel de haute performance à partir de ces polymères dépend du contrôle de l'orientation moléculaire. Dès lors, une étape cruciale est de comprendre les phénomènes de relaxation après l'arrêt des déformations d'écoulement par cisaillement.

La première partie de cette thèse étudie numériquement les effets que les conditions de la surface, les défauts et l'écoulement en retour ont sur les phénomènes de relaxation après arrêt de l'écoulement par cisaillement simple pour un polymère linéaire rigide nématique typique. La théorie du continuum de Leslie-Ericksen et les équations de Euler-Lagrange sur le mouvement de la surface sont dérivées et utilisées dans ce but. Les prédictions se sont montrées physiquement cohérentes.

Lorsqu'on observe l'échantillon cisailé en nicols croisés, on constate que les polymères nématiques développent, dans certaines conditions une texture à bandes transitoires après l'arrêt de l'écoulement par cisaillement. La deuxième partie de cette thèse présente un modèle viscoélastique qui décrit le mécanisme de formation de ce phénomène bien caractéristique et pourtant inexplicable dans le cas d'un polymère linéaire rigide nématique. Ce modèle fait appel aux théories du continuum d'Ericksen et de Landau-de Gennes et prédit que la relaxation des variations spatiales périodiques du paramètre d'ordre scalaire produit dans l'espace, des moments de torsion périodiques sur la directrice. En conséquence, on peut voir une texture à bandes transitoires lorsque l'échantillon cisailé est observé en nicols croisés. Les résultats numériques et les modèles optiques digitalisés sont en accord avec les observations expérimentales rapportées et sont utilisés pour expliquer ces observations.

## Acknowledgments

It is with great pleasure that I acknowledge the constant guidance, support and motivation which my research supervisor, Professor Alejandro D. Rey, has given me throughout the course of this thesis. His continuous strive to teach me on how to become a good researcher is also greatly appreciated.

A postgraduate scholarship from the Natural Sciences and Engineering Research Council of Canada, financial support from the Department of Chemical Engineering, and free computing time from the McGill University Computing Center are all gratefully acknowledged.

I like to thank my colleagues in the Workman Wing for making the last two years very enjoyable. Special thanks goes to my officemates, Yalda Farhoudi and Won Hee Han, for our enlightening discussions on liquid crystals and for keeping me informed on their research findings.

I wish to express my heartfelt appreciation to my sister-in-law, Molly Tam, for her kindness during the past many years. Her thoughtfulness has made my studies a lot easier and will always be remembered.

Lastly, I wish to thank my family for their love, support, encouragement, and for always looking out for the baby of the family.

# Table of Contents

<b>Abstract.....</b>	<b>i</b>
<b>Résumé.....</b>	<b>ii</b>
<b>Acknowledgments.....</b>	<b>iii</b>
<b>Table of Contents.....</b>	<b>iv</b>
<b>Nomenclature.....</b>	<b>vii</b>
<b>Chapter 1</b>	
<b>Introduction</b>	
<b>1.1 Historical Note and Introductory Comments.....</b>	<b>1</b>
<b>1.2 Definition of Liquid Crystalline Phases.....</b>	<b>2</b>
<b>1.3 Types of Liquid Crystals.....</b>	<b>3</b>
<b>1.4 Classification of Liquid Crystalline Phases.....</b>	<b>3</b>
<b>1.4.1 Nematic Order.....</b>	<b>3</b>
<b>1.4.2 Cholesteric Order.....</b>	<b>4</b>
<b>1.4.3 Smectic Order.....</b>	<b>4</b>
<b>1.5 Orientational Order.....</b>	<b>5</b>
<b>1.6 Frank-Oseen-Zocher Static Elastic Continuum Theory.....</b>	<b>6</b>
<b>1.7 Orientational Slip.....</b>	<b>10</b>
<b>1.8 Leslie-Ericksen Continuum Theory.....</b>	<b>13</b>
<b>1.9 Landau-de Gennes Nematic Continuum Theory.....</b>	<b>15</b>
<b>1.10 Ericksen Continuum Theory for Nonhomogeneously Ordered Nematic Phases.....</b>	<b>17</b>
<b>1.11 Liquid Crystal Optics.....</b>	<b>18</b>
<b>1.11.1 Birefringence.....</b>	<b>18</b>
<b>1.11.2 Polarized Light Microscopy of Nematic Phases.....</b>	<b>19</b>

1.12	<b>Banded Texture Formed after Cessation of Shear Flow.....</b>	<b>22</b>
1.12.1	<b>Characteristics of the Banded Texture Formed after Cessation of Shear Flow.....</b>	<b>22</b>
1.12.2	<b>Director Structure Exhibiting the Banded Texture after Cessation of Shear Flow.....</b>	<b>26</b>
1.12.3	<b>Possible Explanations for the Formation of the Banded Texture after Cessation of Shear Flow.....</b>	<b>26</b>
1.12.4	<b>Importance of the Banded Texture Formed after Cessation of Shear Flow in Materials Processing.....</b>	<b>26</b>
1.13	<b>Thesis Outline and Objectives.....</b>	<b>27</b>

## **Chapter 2**

### **Relaxation Phenomena after Cessation of Simple Shear Flow for Perfectly Ordered Nematic Polymers**

2.1	<b>Introduction.....</b>	<b>29</b>
2.2	<b>Balance Equations.....</b>	<b>30</b>
2.3	<b>Results and Discussion.....</b>	<b>36</b>
2.3.1	<b>Effects of Surface Conditions.....</b>	<b>36</b>
2.3.2	<b>Effects of Defects.....</b>	<b>44</b>
2.3.3	<b>Effects of Backflow.....</b>	<b>51</b>
2.4	<b>Summary and Concluding Remarks.....</b>	<b>51</b>

## **Chapter 3**

### **Relaxation Phenomena after Cessation of Shear Flow for Partially Ordered Nematic Polymers**

3.1	<b>Introduction.....</b>	<b>54</b>
3.2	<b>Balance Equations.....</b>	<b>55</b>
3.3	<b>Results and Discussion.....</b>	<b>63</b>
3.3.1	<b>Typical Results on the Relaxation Phenomena and Pattern Formation.....</b>	<b>63</b>
3.3.2	<b>Effects of the Base Value and Amplitude of the Initial Periodic</b>	

	<b>Scalar Order Parameter Spatial Variation on Pattern Formation.....</b>	<b>74</b>
<b>3.4</b>	<b>Summary and Concluding Remarks.....</b>	<b>79</b>

## **Chapter 4**

### **Thesis Summary, Conclusions and Recommendations**

<b>4.1</b>	<b>Thesis Summary.....</b>	<b>86</b>
<b>4.2</b>	<b>Conclusions.....</b>	<b>87</b>
<b>4.3</b>	<b>Recommendations.....</b>	<b>89</b>

	<b>References.....</b>	<b>90</b>
--	------------------------	-----------

### **Appendix A**

	<b>Equations for Chapter 2.....</b>	<b>94</b>
--	-------------------------------------	-----------

### **Appendix B**

	<b>Equations for Chapter 3.....</b>	<b>102</b>
--	-------------------------------------	------------

## Nomenclature

### Roman Symbols

<b>a</b>	see equation (1.24e)
<b>A</b>	Landau-de Gennes free energy density coefficient
<b><math>A_L</math></b>	amplitude of linearly polarized light wave
<b><math>A_S</math></b>	amplitude of the scalar order parameter periodic spatial variation
<b><math>A_\phi</math></b>	amplitude of the twist periodic spatial variation
<b>A</b>	rate of deformation tensor
<b>b</b>	see equation (1.24f)
<b>B</b>	Landau-de Gennes free energy density coefficient
<b>c</b>	concentration
<b><math>c_c</math></b>	critical concentration
<b><math>c_L</math></b>	speed of light in vacuum
<b>C</b>	Landau-de Gennes free energy density coefficient
<b>D'</b>	vibration direction of the ordinary light wave
<b>D''</b>	vibration direction of the extraordinary light wave
<b>E</b>	total free energy

$f_0(T)$	isotropic free energy density at temperature $T$
$F_d$	elastic free energy density
$F_m$	magnetic free energy density
$F_t$	total free energy density
$F_L$	Landau-de Gennes free energy density
$F_S$	see equation (3.4)
$F$	external body force per unit volume
$h$	sample thickness; plate spacing
$h_L$	distance light ray travels in a medium
$h$	molecular field
$h_B$	bend component of $h$
$h_S$	splay component of $h$
$h_T$	twist component of $h$
$H_c$	critical magnetic field
$H$	magnetic field
$I$	light intensity
$I_r$	relative light intensity
$k_B$	Boltzmann constant

$k_S$	length scale of the scalar order parameter periodic spatial variation
$k_\phi$	length scale of the twist angle periodic spatial variation
$k_q$	wavevector of a cholesteric phase
$K$	elastic constant
$K_5$	elastic constant
$K_6$	elastic constant
$K_{11}$	splay elastic constant
$K_{22}$	twist elastic constant
$K_{33}$	bend elastic constant
$L$	plate length
$L_1$	Landau-de Gennes elastic constant
$L_2$	Landau-de Gennes elastic constant
$n_o$	ordinary refractive index
$n_e$	extraordinary refractive index
$\mathbf{n}$	director field
$\Delta n$	measure for birefringence
$\bar{n}$	mean value of the two indices of refraction
$N$	angular velocity of the director relative to that of the fluid

<b>p</b>	<b>pressure</b>
<b>P</b>	<b>spatial period, or half pitch, of a cholesteric phase</b>
<b>P</b>	<b>wave normal of incident light ray</b>
<b>q</b>	<b>see equation (1.2)</b>
<b>Q</b>	<b>tensor order parameter</b>
<b>r</b>	<b>cylindrical coordinate</b>
<b>R</b>	<b>surface area</b>
<b>R<sup>s</sup></b>	<b>Rayleigh dissipation function</b>
<b>S</b>	<b>scalar order parameter</b>
<b>S<sub>eq</sub></b>	<b>equilibrium value of the scalar order parameter</b>
<b>S<sub>f</sub></b>	<b>flow value of the scalar order parameter</b>
<b>S<sub>0</sub></b>	<b>base value of the scalar order parameter periodic spatial variation</b>
<b>t</b>	<b>time</b>
<b>t<sub>b</sub></b>	<b>time for banded texture formation</b>
<b>t<sub>d</sub></b>	<b>life span of the banded texture</b>
<b>t<sub>s</sub></b>	<b>shearing time</b>
<b>t<sub>s,c</sub></b>	<b>critical shearing time</b>
<b>t<sub>φ,m</sub></b>	<b>time to reach maximum twist angle</b>

$t^*$	dimensionless time
$T$	temperature
$T_c$	clearing temperature
$T_c^*$	temperature slightly below the clearing temperature
$U$	dimensionless nematic potential
$v_e$	velocity of the extraordinary light ray
$v_o$	velocity of the ordinary light ray
$V$	volume
$V_x$	x-component of $V$
$V_y$	y-component of $V$
$V_z$	z-component of $V$
$V_y^*$	dimensionless y-component of $V$
$V_{y,m}^*$	dimensionless maximum y-component of $V$
$V$	velocity field
$W$	anchoring strength
$x$	Cartesian coordinate
$x^*$	dimensionless length coordinate
$\mathbf{x}$	position vector

$y$	Cartesian coordinate
$z$	Cartesian coordinate; cylindrical coordinate
$z^*$	dimensionless height coordinate
<b>Greek Symbols</b>	
$\alpha_i, i = 1, \dots, 6$	Leslie viscosities
$\alpha_i^S, i = 1, \dots, 6$	Leslie viscosities that are dependent on $S$
$\beta_i, i = 1, 2$	viscosities in equation (1.26), but are not dependent on $S$
$\beta_i^S, i = 1, 2$	viscosities in equation (1.26)
$\gamma_1$	rotational viscosity
$\gamma_2$	irrotational viscosity
$\gamma_1^S$	rotational viscosity that is dependent on $S$
$\gamma_2^S$	irrotational viscosity that is dependent on $S$
$\dot{\gamma}$	shear rate
$\dot{\gamma}_c$	critical shear rate
$\Gamma_e$	elastic torque on the director per unit volume
$\Gamma_v$	viscous torque on the director per unit volume
$\delta$	variation
$\delta_L$	phase lag between the ordinary and extraordinary light rays

$\delta$	identity tensor; unit tensor
$\zeta$	angle between the polarizer and ordinary ray vibration direction
$\eta_i, i = 1, \dots, 38$	angle-dependent viscosity functions
$\eta_i^*, i = 1, \dots, 38$	dimensionless angle-dependent viscosity functions
$\theta$	tilt angle
$\theta_{eq}$	equilibrium value of $\theta$
$\theta_i$	initial condition for $\theta$
$\Theta$	cylindrical coordinate
$\kappa_i, i = 1, \dots, 44$	angle-dependent elastic functions
$\kappa_i^*, i = 1, \dots, 44$	dimensionless angle-dependent elastic functions
$\lambda_b$	wavelength of the director field exhibiting the banded texture
$\lambda_L$	incident light wavelength
$\lambda^s$	surface viscosity
$\lambda^{s*}$	dimensionless surface viscosity
$v_z$	z-component of the outward unit normal vector
$\mathbf{v}$	outward unit normal vector
$\xi$	Lagrange multiplier
$\pi$	pi

$\rho$	density
$\tau_\theta$	tilt angle relaxation time
$\tau_\phi$	twist angle relaxation time
$\tau$	stress tensor
$\phi$	twist angle
$\phi_{eq}$	equilibrium value of $\phi$
$\phi_i$	initial condition for $\phi$
$\phi_m$	maximum twist angle in periodic director field
$\Phi_\phi$	generalized elastic force
$\chi$	angle between the polarizer and analyzer
$\chi_a$	anisotropic magnetic susceptibility
$\psi$	angle between a molecule and the director
$\Psi$	angle between the incident light ray and optic axis
$\Omega$	vorticity tensor
$\varphi$	phase angle in a cholesteric phase
$\vartheta$	rod concentration
$\infty$	infinity

$\frac{\delta}{\delta(*)}$ 

functional derivative with respect to (\*)

 $\nabla$ 

gradient field

# Chapter 1

## Introduction

### 1.1 Historical Note and Introductory Comments

Although there is a great wealth of information about low molecular weight liquid crystals (LMLC's), the opposite is true for the polymeric ones. The reason for this is that the study of LMLC's began as early as 1888 with Reinitzer. Research, however, on liquid crystalline polymers (LCP's) received its rightful attention only after the commercialization of Kevlar in the early 1970's while their synthesis intensified just a decade later. Despite this fact, LCP's, especially nematic polymers, are gaining wide usage in a variety of applications. For instance, they are used to make bullet proof vests, radial tires, brake linings, tennis rackets, golf clubs, fishing rods and pressure vessels.

Successful manufacturing of products from nematic polymers depends on control of molecular orientation. A crucial step is then to understand the relaxation phenomena after cessation of shear flow deformations, because it is the shear flow-induced molecular orientation that gives these products their excellent mechanical properties. This understanding is the goal of this thesis.

The rest of this chapter outlines briefly concepts of liquid crystal physics that are needed subsequently in the thesis. There is also a review of the ubiquitous banded texture that LCP's exhibit after cessation of shear flow.

## 1.2 Definition of Liquid Crystalline Phases

Many organic materials do not undergo a single transition between the solid and liquid phases, but assume one or more intermediate phases. These phases, called mesophases, have both solid-like molecular order and liquid-like fluidity.

Mesophases possessing a crystal lattice structure but no rotational order are known as disordered crystal mesophases, or plastic crystals [1], and are generally composed of globular molecules. In these phases, the thermal energy overcomes the rotational barrier but not the lattice energy. On the other hand, if the thermal energy destroys the crystal lattice but does not overcome the rotational barrier, there is positional disorder and rotational order [2]. Mesophases having this kind of order are known as ordered fluid mesophases, or liquid crystals, and are generally composed of anisodiametric molecules or monomers as shown in Figure 1.1.

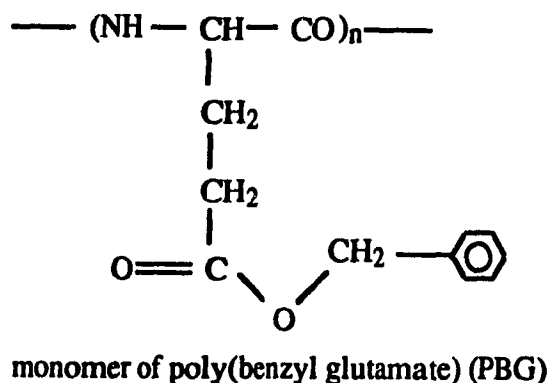
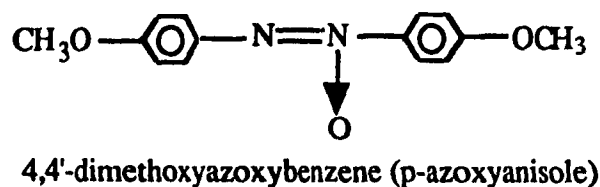
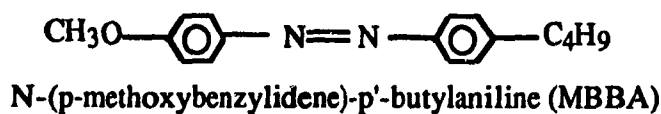


Figure 1.1. Some examples of liquid crystals.

### 1.3 Types of Liquid Crystals

Ordered fluid mesophases are differentiated by how the phase transition is effected. Lyotropic liquid crystals are obtained by concentration changes. Poly(benzyl-L-glutamate) (PBLG), hydroxypropylcellulose (HPC) and deoxyribonucleic acid (DNA) are examples of solutes that form lyotropic ordered fluid mesophases when dissolved at sufficiently high concentrations in the appropriate mediums. Hence, the long range molecular ordering is due to solute-solute interactions. On the other hand, thermotropic liquid crystals are obtained through temperature changes. Since these liquid crystals are melts, they can be processed by fiber spinning and injection molding.

### 1.4 Classification of Liquid Crystalline Phases

A scheme, devised by Friedel [3] in 1922 according to their symmetry, classifies liquid crystals into the three main classes: nematic, cholesteric and smectic.

#### 1.4.1 Nematic Order

In a nematic phase the molecules tend to align parallel to each other and with the director  $\mathbf{n}$  as shown in Figure 1.2. The director is a unit vector that gives the preferred average molecular orientation in the neighborhood of any point  $\mathbf{x}$  [4]. Because of this tendency, long range orientational order and cylindrical (or uniaxial) symmetry are exhibited in this phase. Long range translational disorder (or fluidity), however, is present because there is no correlation of the molecular center of mass positions.



Figure 1.2. The nematic phase of rod-like molecules.

### 1.4.2 Cholesteric Order

As shown in Figure 1.3, cholesteric order is very similar to nematic order on a local level; i.e., the molecules tend to align with the director. The underlying reason for this is that cholesteric phases are obtained from chiral nematic molecules; thus, the terms cholesteric and chiral nematic are synonymous. On a larger scale, however, the director follows a helical path given in Cartesian coordinates as

$$\mathbf{n} = \{ \cos (k_q \cdot \mathbf{x} + \varphi), \sin (k_q \cdot \mathbf{x} + \varphi), 0 \} \quad (1.1)$$

where  $k_q$  is the wavevector and  $\varphi$  is the phase angle. The spatial period, or half-pitch, is given by

$$P = \frac{\pi}{|q|} \quad (1.2)$$

and, for a nematic phase,  $P$  goes to infinity because  $q$  is zero.

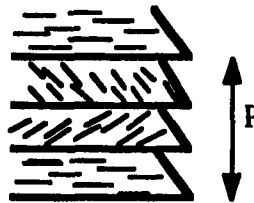


Figure 1.3. The cholesteric phase.

### 1.4.3 Smectic Order

A smectic phase has one degree of translational order which provides a layered structure. There are at least ten identified smectic phases, and the best known are the smectic-A and smectic-C phases. In smectic-A ordering, the molecules are aligned parallel to the layer normal within each layer (Figure 1.4a). If the molecules, however, are uniformly tilted away from the layer normal in each layer, smectic-C ordering results (Figure 1.4b).

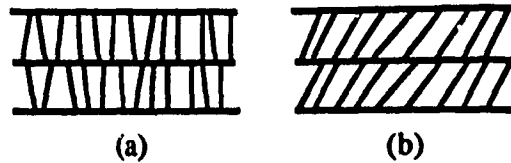


Figure 1.4. The (a) smectic-A and (b) smectic-C phases.

### 1.5 Orientational Order

As mentioned above, in a nematic phase the molecules tend to align parallel to the director  $\mathbf{n}$ . If all the molecules are aligned perfectly parallel to  $\mathbf{n}$ , then a completely ordered nematic phase is present. This, however, is an ideal case since a molecule is usually oriented at an angle  $\psi$  to  $\mathbf{n}$  because of thermal motion at finite temperatures. Since  $\psi$  is not the same for all the molecules oriented about a director, the average value over all these molecules (i.e.,  $\langle \cos^2 \psi \rangle$ ) must be considered. Hence, the scalar order parameter  $S$ , which is a measure of the degree of molecular alignment along  $\mathbf{n}$ , is expressed as [5]

$$S = \frac{1}{2}(3\langle \cos^2 \psi \rangle - 1) \quad (1.3)$$

with

$$-\frac{1}{2} \leq S \leq 1 \quad (1.4)$$

A value of  $S = 1$  defines a perfectly aligned nematic phase, a value of  $S = 0$  defines the isotropic liquid phase, and a value of  $S = -\frac{1}{2}$  defines a nematic phase where the molecules are lying in a plane normal to the director. As an example, for N-(p-methoxybenzylidene)-p'-n-butylaniline (MBBA) at room temperature,  $S = 0.64$  [6]. It is interesting to note that equation (1.3) has the form of the second-order Legendre polynomial  $P_2(\cos \psi) = \frac{1}{2}(3\cos^2 \psi - 1)$ . Figure 1.5 shows schematically how the scalar order parameter varies in the range  $0 \leq S \leq 1$  for the temperature-effected thermotropic and concentration-effected lyotropic liquid crystals. Nematic phases only have first-order transitions [5], and this is seen with  $S$  at the transition points  $T_c$  and  $c_c$ .

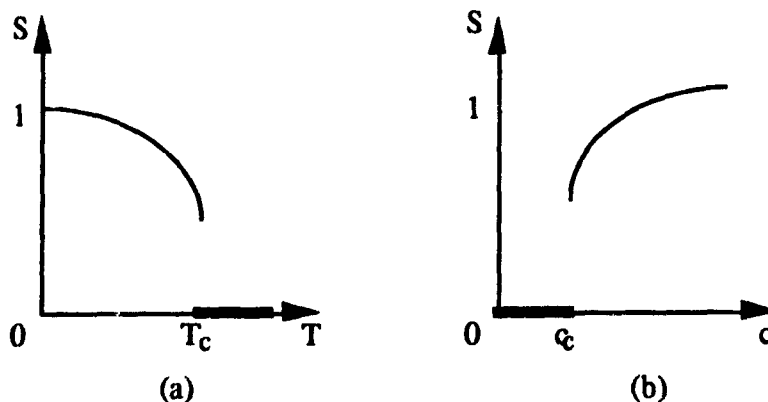


Figure 1.5. Typical variations of the scalar order parameter  $S$  for (a) thermotropic liquid crystals with temperature  $T$  and (b) lyotropic liquid crystals with concentration  $c$ .  $T_c$  and  $c_c$  are the first-order transition points.

The scalar order parameter alone, however, can not describe generally the molecular structure in a nematic phase. The director field must also be included in the general description. Therefore, it is convenient to define the symmetric and traceless tensor order parameter as [7]

$$Q = \frac{1}{2}S(3nn - \delta) \quad (1.5)$$

where  $\delta$  is the unit tensor. The tensor order parameter can be geometrically represented as an ellipsoid in the range  $0 \leq S \leq 1$ . For an unordered uniaxial nematic phase, the two shorter semi-axes are equal and the longer semi-axis is parallel to the director (Figure 1.6a). The ellipsoid gets distorted, however, in the isotropic liquid and perfectly ordered uniaxial nematic phases. When  $S = 0$ , all three semi-axes are equal, and the ellipsoid becomes a sphere (Figure 1.6b). No director is shown in this figure because the phase is an isotropic liquid. When  $S = 1$ , the two shorter semi-axes are zero, and the ellipsoid becomes a line parallel to the director (Figure 1.6c).

## 1.6 Frank-Oseen-Zocher Static Elastic Continuum Theory

In applications, the director is not oriented uniformly in a nematic phase but varies spatially because of electromagnetic body forces, surface forces and/or flow fields. These spatial variations of the average molecular orientation increase the elastic free energy

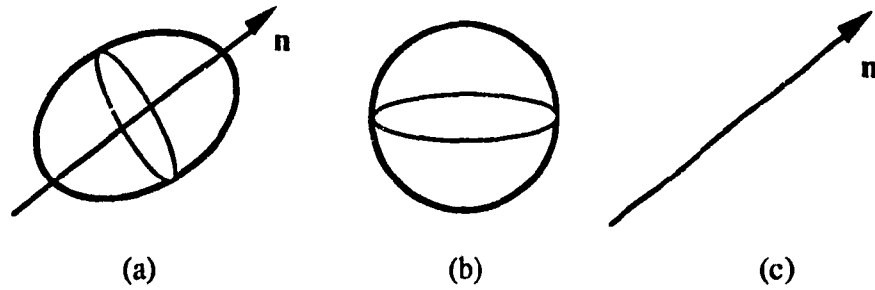


Figure 1.6. Geometrical representations of the tensor order parameter when (a)  $0 < S < 1$ , (b)  $S = 0$ , and (c)  $S = 1$ .

density  $F_d$  of the phase. If the gradient of the director is everywhere small enough such that the change in  $\mathbf{n}$  over the length of a single molecule is insignificant, then  $F_d$  can be derived from a continuum theory [4]. The theory used presently was developed by Oseen [8], Zocher [9], Frank [10] and Ericksen [11]. Frank [10] derived the formula of the elastic free energy density from a variant of Hooke's law using the cylindrical symmetry of nematic phases. The result of the derivation is

$$F_d = \frac{1}{2} \{ K_{11} (\nabla \cdot \mathbf{n})^2 + K_{22} (\mathbf{n} \cdot \nabla \times \mathbf{n})^2 + K_{33} (\mathbf{n} \times \nabla \times \mathbf{n})^2 \} \quad (1.6)$$

where  $K_{11}$ ,  $K_{22}$  and  $K_{33}$  are the splay, twist and bend temperature-dependent elastic constants, respectively, and are known collectively as the Frank elastic constants. These three modes of director deformations are depicted individually in Figure 1.7. A basic mode having a relatively lower elastic constant value predominates in the deformation; i.e., the distortion contains more of this mode. As an order of magnitude, using the intermolecular interaction energy as the characteristic energy and the separation between two molecules as the characteristic length, the elastic moduli are estimated to be approximately  $10^{-12}$  N [12]. This compares very well with the values reported for poly(benzylglutamate) (PBG) [13]:  $K_{11} = 1.21 \times 10^{-11}$  N,  $K_{22} = 7.8 \times 10^{-13}$  N and  $K_{33} = 7.63 \times 10^{-12}$  N. The effects of the long polymeric molecules are shown by these three elastic constants. Since splay deformations require concentrations of molecular ends, it is very unlikely that a LCP phase will have this distortion; therefore,  $K_{11} > K_{22}$  and  $K_{11} > K_{33}$ .

It is often convenient to assume that the nematic phase is elastically isotropic; i.e.,  $\mathbf{K} = K_{11} = K_{22} = K_{33}$  and  $F_d$  simplifies to [14]

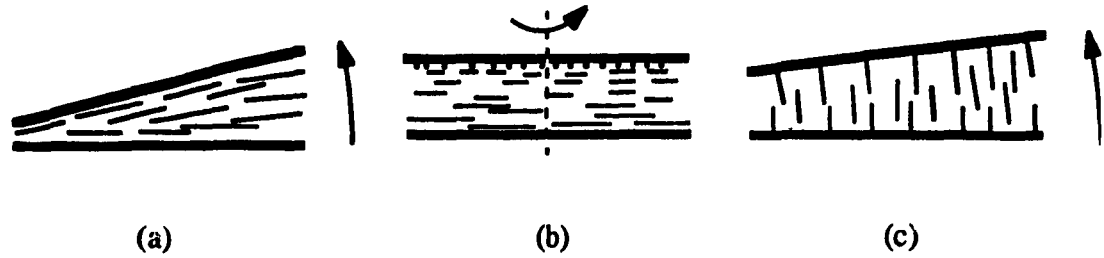


Figure 1.7. Director configurations in (a) splay, (b) twist, and (c) bend deformations.

$$F_d = \frac{1}{2}K[(\nabla \cdot \mathbf{n})^2 + (\nabla \times \mathbf{n})^2] \quad (1.7)$$

This assumption is not quantitatively correct, for instance, if one compares the three elastic constants above for PBG, but it still is a valuable tool to help understand director distortions [14]. The total free energy  $E$  of the distorted configuration, obtained by performing a volume integration of  $F_d$ , is

$$E = \int F_d dV \quad (1.8)$$

The condition for equilibrium is a minimum value for  $E$ ; i.e., [15]

$$-\nabla \cdot \frac{\partial F_d}{\partial \nabla n_i} + \frac{\partial F_d}{\partial n} = \xi n \quad (1.9)$$

where  $\xi$  is a Lagrange multiplier introduced to satisfy the constraint of unit director ( $\mathbf{n} \cdot \mathbf{n} = 1$ ).

Equation (1.6) can not account for any externally applied fields, such as a magnetic field. To include the effects of a magnetic field, the magnetic free energy density  $F_m$ , expressed as

$$F_m = -\frac{1}{2} \chi_a (\mathbf{n} \cdot \mathbf{H})^2 \quad (1.10)$$

is added to the elastic free energy density  $F_d$  to get the total free energy density  $F_t$ ; i.e.,

$$F_t = F_H + F_m \quad (1.11)$$

$\chi_a$  is the anisotropic magnetic susceptibility and  $H$  is the magnetic field. Hence, to determine the equilibrium director configuration,  $F_t$  is used instead of  $F_d$  in equation (1.9).

Magnetic fields are used quite often on liquid crystals, especially in determining the values of the Frank elastic constants. This is done by applying a sufficiently strong magnetic field perpendicularly to a uniformly aligned nematic phase confined in a cell. Two conditions must be met in these determinations. The directors are not allowed to reorient on the surface, and must be either parallel or perpendicular to the bounding surfaces. Since there are three Frank elastic constants, there are three types of magnetic instabilities. These instabilities were observed by Freedericksz in 1927 [16], and are thus called the Freedericksz transitions. They are shown in Figure 1.8.

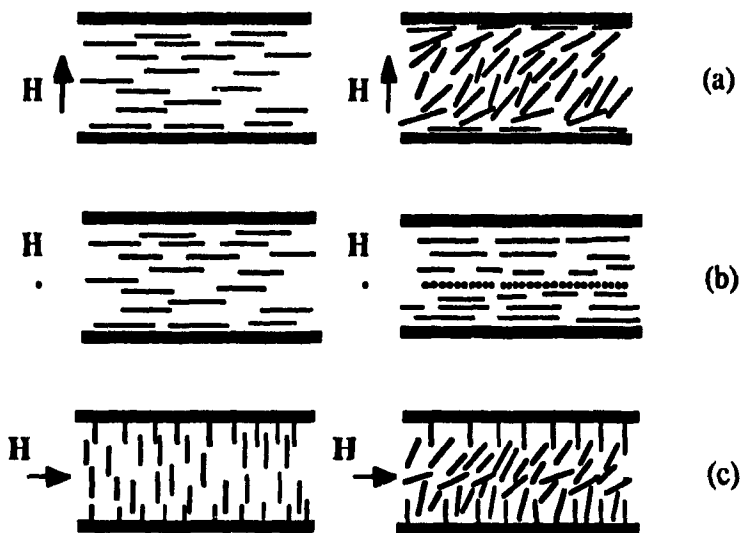


Figure 1.8. The three types of Freedericksz transitions: (a) splay mode, (b) twist mode, and (c) bend mode.  $H$  is the magnetic field.

De Gennes [14] showed by manipulating equation (1.11) that the instabilities only occur if the applied fields exceed their critical values, which are given by

$$H_{c,i} = \frac{\pi}{h} \sqrt{\frac{K_i}{\chi_a}} \quad (1.12)$$

$h$  is the plate spacing, and  $i = 11, 22, 33$  stands for splay, twist and bend, respectively. The elastic constants are then determined by measuring the three critical fields. Equation (1.12) also shows that the critical fields scale with the inverse of the cell thickness, which has already been determined by Freedericksz [16].

### 1.7 Orientational Slip

The term orientational slip denotes that the director may reorient at a bounding surface. If the surface is treated physically (for example, by rubbing in one direction) or chemically (for example, by buffing) then surface director reorientation is not permitted, and this condition is defined as strong director anchoring. However, since a bounding surface is usually untreated, orientational slip is a very important phenomenon in liquid crystal physics. For instance, Figure 1.9 shows typical director relaxation from a simple shear flow-induced orientation for both fixed (or strong) and weak director anchoring at the two bounding surfaces. Figure 1.9a shows that for fixed anchoring, all the bulk directors relax to that of the surface director orientation. On the other hand, Figure 1.9b shows that for weak anchoring, both the bulk and surface directors reorient toward each other during the relaxation and will eventually form a homogeneously oriented phase. Another example is the recent modeling of the periodic twist instability of nematic polymers due to a magnetic field by Rey [17]. He showed that at low magnetic fields, the surfaces have an effect on the amplitudes and time scales of the periodic response. Therefore, it is necessary to include orientational slip to the present theories that describe the dynamical phenomena of nematic polymers. The mathematical formulation for orientation slip consists of both elastic and dissipative interactions, and is presented below.

The static interaction between a nematic polymer and a bounding surface is described macroscopically by a surface free energy. This free energy is composed of both the surface deformation energy and the coupling energy of the director at the surface [18]. The surface deformation energy is due to director gradients at the surface, and is introduced by surface elastic constants. The coupling energy depends on the orientation of the surface director with respect to the easy axis of the surface, which is the preferred surface director orientation. The easy axis depends on the specific interaction between the nematic polymer and bounding surface, and on the surface treatment mentioned above [18]. The coupling energy, introduced into the surface free energy by the anchoring strength  $W$  [14], is a minimum when the director is aligned with the easy axis. When  $W \Rightarrow \infty$ , the director aligns along the easy axis (strong anchoring), and when  $W$  is finite

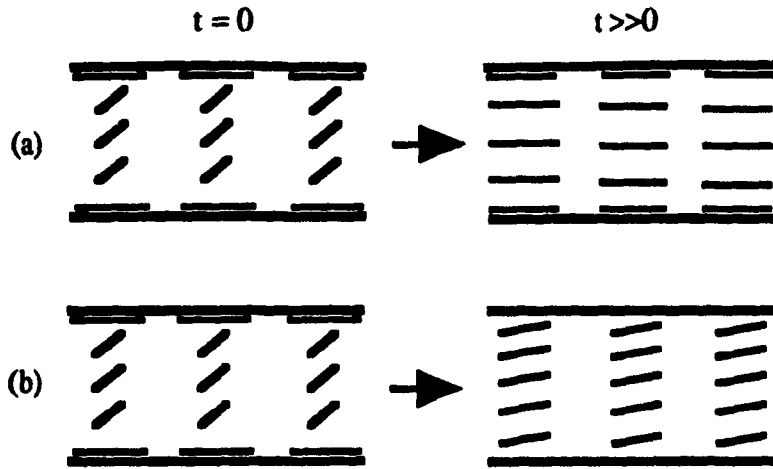


Figure 1.9. Schematic representations of typical director relaxation phenomena for (a) fixed anchoring and (b) weak anchoring of the director at the two bounding surfaces.

the time-dependent surface director orientation is obtained from the balance between surface elastic and viscous torques about an axis normal to the surface. The surface elastic torques are due to bulk director deformations impressed onto the surface, surface director gradients, and deviations of the surface director from the easy axis. Viscous torques are created from the transient director reorientation, and are introduced by surface viscosities.

The Euler-Lagrange equation for surface motion is used to formulate the balance of surface elastic and viscous torques. Assuming no positional slip and planar orientation in a parallel plate geometry, the Euler-Lagrange equation is written as [19]

$$\frac{\partial R^s}{\partial \dot{\phi}} + \Phi_\phi = 0 \quad (1.13)$$

where  $R^s$  is the surface Rayleigh dissipation function,  $\Phi_\phi$  are the elastic forces, and a superposed dot denotes time differentiation.  $\phi$  is the planar orientation angle and the only generalized coordinate. For more complex phenomena, two generalized coordinates are used, such as  $\phi$  and  $\theta$ . Since the frictional force  $\frac{\partial R^s}{\partial \dot{\phi}}$  is a linear function of the velocities

[19],  $R^s$  is given as

$$R^S = \lambda^S \dot{\phi} \cdot \dot{\phi} \quad (1.14)$$

where  $\lambda^S$  is the surface viscosity for the surface director reorientation. There are no known experimentally reported values for  $\lambda^S$ , but it is bounded in the range from zero (free director rotation) to infinity (strong director anchoring).

The elastic forces are acquired from the surface contribution to the variation of the total elastic free energy of the system. This energy is composed of both bulk and surface contributions, but with a couple of justifiable assumptions given below, only the bulk term is needed. Firstly, for entropic reasons, the planar director orientation has been found to be the most likely scenario for a nematic polymer at a bounding surface [20], and this has been substantiated experimentally for poly(1,4-benzamide) (PBA) [21-23], and poly(1,4-phenylene-2,6-benzobis(thiazole)) (PBT) [24]. There are, however, exceptions such as for poly(benzyl-L-glutamate) (PBLG) [25]. Since this analysis is restricted only to planar director orientations contained within untreated isotropic parallel plates, it is assumed that any planar orientation is an easy axis [17,21]; therefore, the coupling energy is a minimum and neglected. Secondly, the surface deformation energy is also neglected since there are no known experimental reports on this energy for nematic polymers [17]. The total free energy is, therefore, given by equations (1.6) and (1.8). The variation of equation (1.8) reads

$$\delta E = \int \left[ \frac{\partial F_d}{\partial \phi} \delta \phi + \frac{\partial F_d}{\partial \nabla \phi} \cdot \delta \nabla \phi \right] dV \quad (1.15)$$

and, after applying the divergence theorem, becomes

$$\delta E = \int \left[ \frac{\partial F_d}{\partial \phi} \delta \phi - \nabla \cdot \frac{\partial F_d}{\partial \nabla \phi} \delta \phi \right] dV + \int \left[ \frac{\partial F_d}{\partial \nabla \phi} \cdot \nu \delta \phi \right] dR \quad (1.16)$$

where  $\nu$  is the outward unit normal vector to the enclosing surface  $R$  of the volume  $V$ . Hence, the elastic forces  $\Phi_\phi$  caused by bulk deformations at the two bounding surfaces are expressed as

$$\Phi_\phi = \frac{\partial F_d}{\partial \nabla \phi} \cdot \nu \quad (1.17)$$

## 1.8 Leslie-Ericksen Continuum Theory

The Leslie-Ericksen (L-E) continuum theory is a viscoelastic nonlinear model that applies to nematic phases with rigid rod-like molecules, assumes the scalar order parameter is a constant, and takes into account backflow effects [26-29]. Backflows are present when the director reorientation produces transient shear flows. This effect is shown schematically in Figure 1.10 for the bend mode of the Fredericksz transition. This theory simplifies to the Frank-Oseen-Zocher continuum theory for the static case. Because flow does not affect  $S$  in low molecular weight nematic phases [30], which are generally composed of rigid molecules, the L-E theory describes very well the dynamics of these phases. Many of its significant predictions have been confirmed by experiments [30,31]. Jenkins [31] gives an extensive summary of confirmations for steady plane and cylindrical Poiseuille and Couette flows. He also shows that the L-E theory describes the onset of the flow instabilities conventional nematic phases have during these two types of flows.

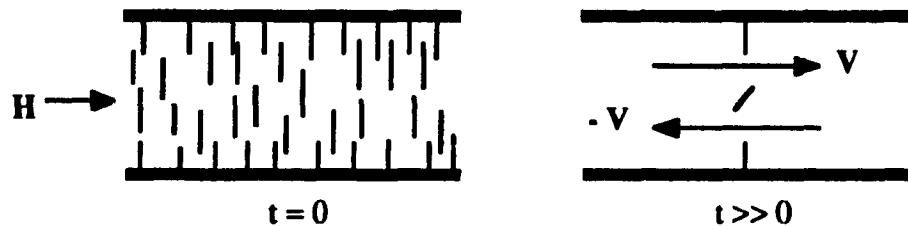


Figure 1.10. Schematic representation of the director reorientation-induced backflows  $V$  in the bend mode geometry of the Fredericksz transition.

Nematic polymers are generally composed of nonrigid molecules and flow affects  $S$  in these materials [30]. Because of this, the extent of the L-E theory in describing nematic polymers is still not known. Since the dynamical terms in this theory arise from the low deformation rate limit of Doi's theory for LCP's [32], it should describe well creeping flows of nematic polymers; however, this does not seem to be true [30]. Nevertheless, it has been used successfully by Rey [17] to describe the planar periodic twist magnetic instability of nematic polymers observed and characterized experimentally by Fincher [21]. Therefore, the L-E continuum theory is presented below, as outlined by

de Gennes [14], with the aim that it will be used to describe the macroscopic relaxation phenomena of nematic polymers after cessation of simple shear flow.

In Cartesian tensorial notation for an incompressible fluid, the linear momentum balance equation is

$$\rho \dot{\mathbf{V}} = \mathbf{F} + \nabla \cdot \boldsymbol{\tau} \quad (1.18)$$

where  $\rho$  is the density,  $\mathbf{V}$  is the velocity, and  $\mathbf{F}$  is the external body force per unit volume. The superposed dot now denotes the material time derivative. The constitutive equation for the stress tensor  $\boldsymbol{\tau}$  is given as

$$\boldsymbol{\tau} = -p\boldsymbol{\delta} - \frac{\partial F_d}{\partial \nabla \mathbf{n}} \cdot (\nabla \mathbf{n})^T + \alpha_1(\mathbf{nn}:\mathbf{A})\mathbf{nn} + \alpha_2\mathbf{nN} + \alpha_3\mathbf{Nn} + \alpha_4\mathbf{A} + \alpha_5\mathbf{nn} \cdot \mathbf{A} + \alpha_6\mathbf{A} \cdot \mathbf{nn} \quad (1.19)$$

where the kinematic quantities are defined as follow:

$$\mathbf{A} = \frac{1}{2}[(\nabla \mathbf{V})^T + \nabla \mathbf{V}] \quad (1.20a)$$

$$\mathbf{N} = \dot{\mathbf{n}} - \boldsymbol{\Omega} \cdot \mathbf{n} \quad (1.20b)$$

$$\boldsymbol{\Omega} = \frac{1}{2}[(\nabla \mathbf{V})^T - \nabla \mathbf{V}] \quad (1.20c)$$

The  $\{\alpha_i\}$ ,  $i = 1, \dots, 6$  are known as the Leslie viscosities,  $p$  is the pressure and  $\boldsymbol{\delta}$  is the unit tensor.  $\mathbf{A}$  is the rate of deformation tensor,  $\mathbf{N}$  is the angular velocity of the director relative to that of the fluid, and  $\boldsymbol{\Omega}$  is the vorticity tensor. The  $ij$  th Cartesian component of  $\nabla \mathbf{n}$  and  $\nabla \mathbf{V}$  are  $\frac{\partial n_j}{\partial x_i}$  and  $\frac{\partial V_j}{\partial x_i}$ , respectively.

The internal angular momentum balance equation in Cartesian tensorial form that governs the director is

$$\boldsymbol{\Gamma}_e + \boldsymbol{\Gamma}_v = \mathbf{0} \quad (1.21)$$

The director inertia is neglected here.  $\boldsymbol{\Gamma}_e$  and  $\boldsymbol{\Gamma}_v$  are the elastic and viscous torques on the director per unit volume, respectively, and their constitutive equations are as follow:

$$\boldsymbol{\Gamma}_e = \mathbf{n} \times \mathbf{h} \quad (1.22a)$$

$$\Gamma_V = -\mathbf{n} \times (\gamma_1 \mathbf{N} + \gamma_2 \mathbf{A} \cdot \mathbf{n}) \quad (1.22b)$$

where

$$\gamma_1 = \alpha_3 - \alpha_2 \quad (1.23a)$$

$$\gamma_2 = \alpha_6 - \alpha_5 = \alpha_2 + \alpha_3 \quad (1.23b)$$

$\gamma_1$  is the rotational viscosity and  $\gamma_2$  is the irrotational viscosity. The equality in equation (1.23b) is due to Parodi [33]; hence, there are only five independent Leslie viscosities. The molecular field  $\mathbf{h}$  arising from the elasticity of the material is defined as follows:

$$\mathbf{h} = \mathbf{h}_S + \mathbf{h}_T + \mathbf{h}_B \quad (1.24a)$$

$$\mathbf{h}_S = K_{11} \nabla(\nabla \cdot \mathbf{n}) \quad (1.24b)$$

$$\mathbf{h}_T = -K_{22} [a \nabla \times \mathbf{n} + \nabla \times (a \mathbf{n})] \quad (1.24c)$$

$$\mathbf{h}_B = K_{33} [b \times \nabla \times \mathbf{n} + \nabla \times (\mathbf{n} \times b)] \quad (1.24d)$$

$$a = \mathbf{n} \cdot \nabla \times \mathbf{n} \quad (1.24e)$$

$$b = \mathbf{n} \times \nabla \times \mathbf{n} \quad (1.24f)$$

## 1.9 Landau-de Gennes Nematic Continuum Theory

In 1937, Landau [7] speculated that near a second-order phase transition point, the free energy density can be expanded as a power series in terms of one or more long range order parameters and their spatial derivatives. Since only the leading terms are important near the transition point, the resulting expansion is a low-order polynomial with temperature-dependent coefficients. De Gennes [7,34] later applied successfully Landau's theory to the first-order phase transition of nematic phases. For a nematic phase, the order parameter is the scalar order parameter defined by equation (1.3), and the free energy density  $F_L$  is expressed as

$$\begin{aligned}
F_L = & f_0(T) + \frac{3}{4}A(T - T_c^*)S^2 + \frac{1}{4}BS^3 + \frac{9}{16}CS^4 + \frac{3}{4}(L_1 + \frac{1}{6}L_2)(\nabla S)^2 + \frac{3}{8}L_2(\mathbf{n} \cdot \nabla S)^2 + \\
& \frac{9}{4}S^2[(L_1 + \frac{1}{2}L_2)(\nabla \cdot \mathbf{n})^2 + L_1(\mathbf{n} \cdot \nabla \times \mathbf{n})^2 + (L_1 + \frac{1}{2}L_2)(\mathbf{n} \times \nabla \times \mathbf{n})^2] + \\
& \frac{3}{7}L_2S(\nabla \cdot \mathbf{n}) \times (\mathbf{n} \cdot \nabla S) + \frac{3}{4}L_2S(\mathbf{n} \times \nabla \times \mathbf{n}) \cdot \nabla S
\end{aligned} \tag{1.25}$$

$f_0(T)$  is the isotropic free energy density at temperature  $T$ , and  $A$ ,  $B$ ,  $C$ ,  $L_1$  and  $L_2$  are constants.  $T_c^*$  is a temperature slightly below the clearing temperature  $T_c$  where the first-order transition occurs.

Equation (1.25) contains four types of terms. The first four terms contain only the scalar order parameter, while the next two contain spatial variations of this parameter. The following term accounts for director spatial variations, and is expressed as such to resemble the Frank-Oseen-Zocher free energy density (equation (1.6)). It should be remarked that, to second-order in the Landau-de Gennes theory, there are only two independent elastic constants ( $L_1$  and  $L_2$ ); however, there are three for nematic phases ( $K_{11}$ ,  $K_{22}$  and  $K_{33}$ ; i.e., the Frank elastic constants) [10]. The last two terms account for the couplings in the variations of  $S$  and  $\mathbf{n}$ .

Notice that  $F_L$  simplifies to  $F_d$  when  $S$  is a constant. Therefore,  $F_L$  can be used generally for any nematic phase, but  $F_d$  applies only to special cases; this is shown schematically in Figure 1.11. Also,  $F_L$  assumes that the splay and bend elastic constants are equal. For most nematics, this is a good approximation.

As mentioned in Section 1.8, shear flow affects the scalar order parameter in nematic polymers [30], which can result in spatial variations in  $S$ . This idea of spatially nonhomogeneous  $S$  is supported by the predicted temporal oscillations of  $S$  in monodomain and spatially invariant nematic polymer systems during shear flow [30,35,36]. Nematic polymers also contain high concentrations of defects, which are points and lines (or disclinations) where the director field changes discontinuously [14], and this also contributes to spatial variations in  $S$ . Since the goal of this thesis is to study the relaxation phenomena of nematic polymers after cessation of shear flow, it is desired to use a free energy density that includes spatial variations in  $S$ , such as  $F_L$ . This does not mean, however, that  $F_d$  is no longer useful. Its simpler form is easier to handle, and will be used initially, as explained below in Section 1.13, in the hope of understanding the macroscopic behavior of nematic polymers after cessation of simple shear flow.

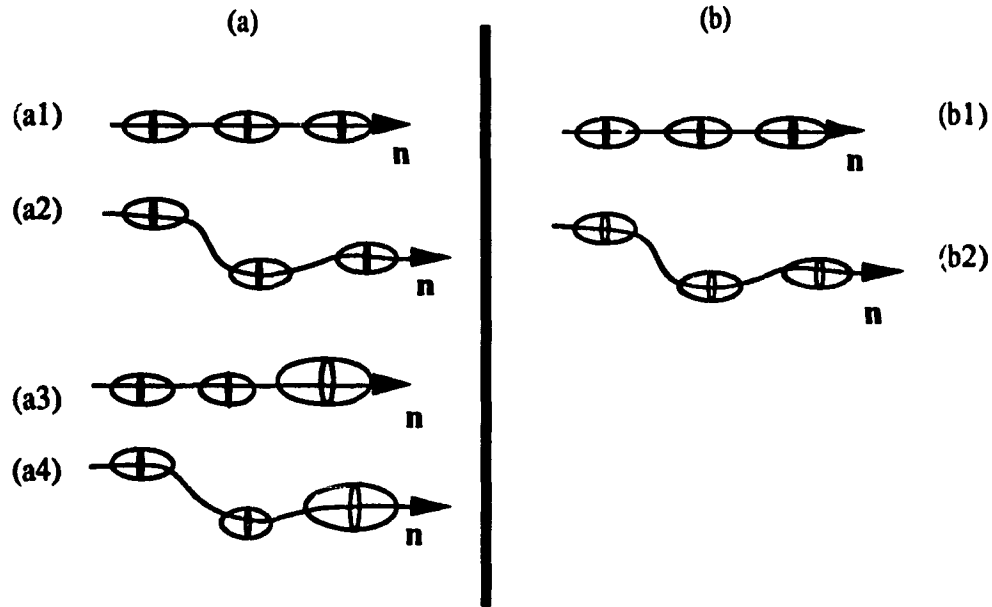


Figure 1.11. Typical nematic structures in which (a)  $F_L$  and (b)  $F_d$  can be used. In (a1) and (b1)  $S \neq S(x,t)$  and  $n \neq n(x,t)$ ; (a2) and (b2)  $S \neq S(x,t)$  and  $n = n(x,t)$ ; (a3)  $S = S(x,t)$  and  $n \neq n(x,t)$ ; and (a4)  $S = S(x,t)$  and  $n = n(x,t)$ .

### 1.10 Ericksen Continuum Theory for Nonhomogeneously Ordered Nematic Phases

Recently, Ericksen [37] proposed a modified version of the Leslie-Ericksen continuum theory to accommodate static and moving defects and to model the more complex behavior of nematic polymers [15,30,37], which include: (1) the formation of periodic textures during shear flow, (2) the formation of periodic textures after cessation of shear flow, (3) the first normal stress difference changes sign from positive to negative and back to positive as the shear rate increases, (4) the viscosity increases with temperature, (5) shear thickening, and (6) the Cox-Merz rule is not obeyed. The most significant change is the addition of the scalar order parameter  $S$ , which is another internal structural parameter. Since one of the goals of this thesis is to explain the formation of the periodic textures formed after cessation of shear flow in nematic polymers, the Ericksen theory is presented below as outlined by Edwards *et al.* [38].

The balance equations for  $S$  and  $n$  are defined as follow:

$$\dot{S} = - \frac{1}{\beta_2^S(S)} \frac{\delta F_L}{\delta S} - \frac{\beta_1^S(S)}{\beta_2^S(S)} n^T \cdot A \cdot n \quad (1.26)$$

$$\dot{\mathbf{n}} = \boldsymbol{\Omega} \cdot \mathbf{n} + \frac{\dot{\gamma}_2^S(S)}{\gamma_1^S(S)} [\mathbf{n}(\mathbf{n}^T \cdot \mathbf{A} \cdot \mathbf{n}) - \mathbf{A} \cdot \mathbf{n}] - \frac{1}{\gamma_1^S(S)} \frac{\delta F_L}{\delta \mathbf{n}} \quad (1.27)$$

The superposed dot denotes the material time derivative, and  $\frac{\delta}{\delta(*)}$  denotes the functional derivative with respect to (\*). The superscript S denotes that the material property varies with S; therefore, the rotational and irrotational viscosities given in Section 1.8 as  $\gamma_1$  and  $\gamma_2$  becomes  $\gamma_1^S$  and  $\gamma_2^S$ , respectively, and are now functions of S. The two new viscosities introduced by the balance equation for S,  $\beta_1^S$  and  $\beta_2^S$ , are also dependent on S. Other terms are already defined in Section 1.8. The constitutive equation for the stress tensor is defined as

$$\begin{aligned} \boldsymbol{\tau} = & -p\delta - \rho\delta \frac{\partial F_L}{\partial \nabla \mathbf{n}} \cdot (\nabla \mathbf{n})^T - \frac{\partial F_L}{\partial \nabla S} \nabla S + \beta_1^S(S) \dot{S} \mathbf{nn} + \alpha_1^S(S) (\mathbf{nn} : \mathbf{A}) \mathbf{nn} + \\ & \alpha_2^S(S) \mathbf{nN} + \alpha_3^S(S) \mathbf{Nn} + \alpha_4^S(S) \mathbf{A} + \alpha_5^S(S) \mathbf{nn} \cdot \mathbf{A} + \alpha_6^S(S) \mathbf{A} \cdot \mathbf{nn} \end{aligned} \quad (1.28)$$

where now the Leslie viscosities ( $\{\alpha_i\}$ ,  $i = 1, \dots, 6$ ) become ( $\{\alpha_i^S\}$ ,  $i = 1, \dots, 6$ ), and are also dependent on S. Ericksen [37] derived expressions in terms of S for these viscosities, but they all contain undermined coefficients. Edwards *et al.* [38] obtained complicated expressions for these viscosities through simplifications of their formulation, which describes the dynamical behavior of liquid crystals through generalized brackets, to obtain the Ericksen theory.

## 1.11 Liquid Crystal Optics

### 1.11.1 Birefringence

Since a nematic phase has cylindrical symmetry, it is uniaxially birefringent in its natural equilibrium state; i.e., it has two refractive indices. As a result of this, a ray of light incident on the phase will be divided into two rays which vibrate orthogonally to each other and to the direction of propagation of the incident beam. They are the ordinary ray (or O-ray) propagating with velocity  $v_o$ , and the extraordinary ray (or E-ray) with velocity  $v_e$ . The refractive indices are

$$n_o = \frac{c_L}{|v_o|} \quad (1.29a)$$

$$n_e = \frac{c_L}{|v_e|} \quad (1.29b)$$

where  $c_L$  is the speed of light in vacuum. The measure for birefringence is

$$\Delta n = n_e - n_o \quad (1.30)$$

Nematic phases of rod-like molecules are uniaxially positive; i.e.,  $n_e$  is greater than  $n_o$ . Since the two velocities are different, a phase lag  $\delta_L$  between the two waves is introduced as they propagate through the medium.

The refractive index ellipsoid shown in Figure 1.12 is used to show how the relative magnitudes of the refractive indices vary with direction of incident light for a uniaxial crystal. The optic axis is an axis of symmetry, and runs along the longest semi-axis of the ellipsoid. For a nematic phase of rod-like molecules, the optic axis coincides with the director. If a light beam is propagated along OH, then the relative magnitudes of  $n_o$  and  $n_e$  are OW and OV, respectively. If the beam is propagated along OV, then both  $n_o$  and  $n_e$  are the radius of the equatorial circle such as OW, and there is no birefringence. As a nonextreme case,  $n_o$  and  $n_e$  are OW and OD, respectively, if light is propagated along ON. Therefore, maximum birefringence occurs when the light is incident normally to the optic axis, and minimum (i.e., no birefringence) if it is parallel to the optic axis. Furthermore, the value for  $n_o$  does not depend on the light ray propagation direction.

Figure 1.12 does not give the actual vibration directions of the O- and E-rays relative to the incident beam. These directions are found, again, with the aid of an ellipsoid. Figure 1.13 shows an example when the incident light wave normal  $\mathbf{P}$  is near the optic axis. The hatched region represents the principal plane, which contains  $\mathbf{P}$  and the optic axis. The elliptical section through O made by the plane perpendicular to  $\mathbf{P}$  is symmetrical about the principal plane; therefore, the principal axes of the ellipse are perpendicular and parallel to the principal plane [39]. These axes are represented by the two vectors  $\mathbf{D}'$  and  $\mathbf{D}''$ , and are the vibration directions of the ordinary and extraordinary waves, respectively.

### 1.11.2 Polarized Light Microscopy of Nematic Phases

Light which vibrates in only one direction is called plane or linearly polarized light. As described above, a ray of light entering a nematic phase is divided into two

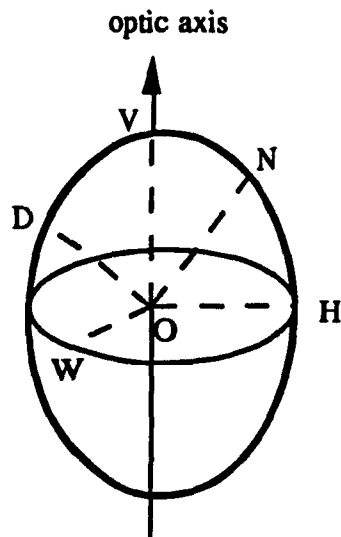


Figure 1.12. Refractive index ellipsoid for a uniaxial crystal.

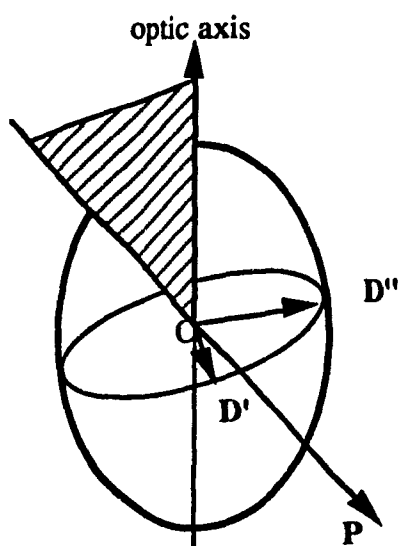


Figure 1.13. The directions of vibration for a uniaxial crystal.

rays, which travel at different velocities and vibrate at orthogonal directions. This description also applies to linearly polarized light.

A polarizing microscope is often used to study the textures of a nematic phase. When the sample is placed between the polars, an interference pattern is obtained above the analyzer. The analyzer allows only the vibration components of the O- and E-rays parallel to it to be transmitted for interference. This means that extinction (or no light transmission) only occurs when the vibration and transmission directions are orthogonal. The intensity of the interference I is [39]

$$I = A_L^2 \left\{ \cos^2 \chi - \sin(2\zeta) \sin 2(\zeta - \chi) \sin^2 \left( \frac{1}{2} \delta_L \right) \right\} \quad (1.31)$$

where  $A_L$  is the amplitude of the linearly polarized light,  $\chi$  is the angle between the polarizer and the analyzer, and  $\zeta$  is the angle between the polarizer and the O-ray vibration direction. The phase lag is

$$\delta_L = \frac{2\pi h_L (n_e - n_o) \sin^2 \Psi}{\lambda_L \cos \bar{n}} \quad (1.32)$$

where  $h_L$  is the distance the light ray travels in the medium,  $\lambda_L$  is the incident light wavelength,  $\Psi$  is the angle between the incident light and the optic axis, and  $\bar{n}$  is the mean value of the two indices of refraction. Polarizing microscopes with  $\chi = 90^\circ$  are called crossed polars, and are used frequently to study nematic phases. The intensity then simplifies to

$$I = A_L^2 \sin^2(2\zeta) \sin^2 \left( \frac{1}{2} \delta_L \right) \quad (1.33)$$

An application of crossed polars is to classify liquid crystalline phases at rest. For instance, a nematic phase exhibits *structures à noyaux* (or Schlieren texture) shown in Figure 1.14. As mentioned in Section 1.9, nematic polymers contain high concentrations of defects. Figure 1.14 shows these defects as disclinations. The light extinction regions originate and terminate at disclinations directed into the page, and are known as brushes. Some possible director field patterns around these disclinations [4] are depicted in Figure 1.15.

The above equations and the next section on the banded textures seen after cessation of shear flow show that clear insights on the nematic phase microstructure (i.e., the director spatial distribution) are obtained by polarized light microscopy. In this thesis,

these calculations are performed on the predicted transient director fields to obtain optical textures so that comparisons can be made with experimentally observed results acquired using crossed polars.



Figure 1.14. The Schlieren texture seen using a polarizing microscope.  
(Reprinted from Chandrasekhar and Ranganath [4].)

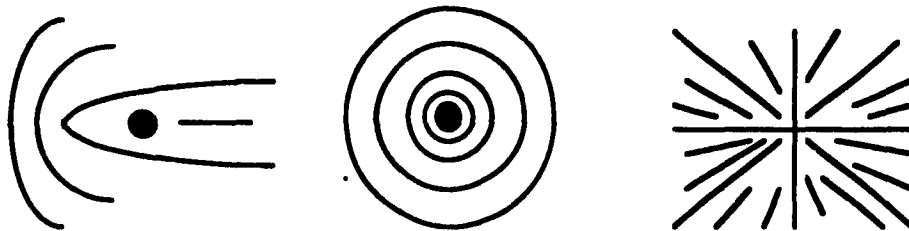


Figure 1.15. Some possible director field patterns around the disclination in the Schlieren texture.

## 1.12 Banded Texture Formed after Cessation of Shear Flow

### 1.12.1 Characteristics of the Banded Texture Formed after Cessation of Shear Flow

When a sheared sample of a LCP is placed between crossed polars with one of the

polars parallel to the prior shearing direction, a banded texture, subjected to the two conditions given below, appears perpendicular to the prior shearing direction [40-62]. Figure 1.16 shows a typical banded texture formed some time after cessation of shear flow [51]. This texture consists of fine, long, parallel and equidistant black lines [53]. All nematic and cholesteric LCP's have this characteristic property [58]. This phenomenon could then serve as a means to characterize polymers as either being liquid crystalline or isotropic depending on whether they do or do not, respectively, form the banded texture after cessation of shear flow. Many experimental results in the literature are for cholesteric LCP's. Navard and Zachariades [51] stated, however, that upon shear, a cholesteric-to-nematic transition occurs, which has a relaxation time after cessation of shear flow much longer than that of the banded texture.

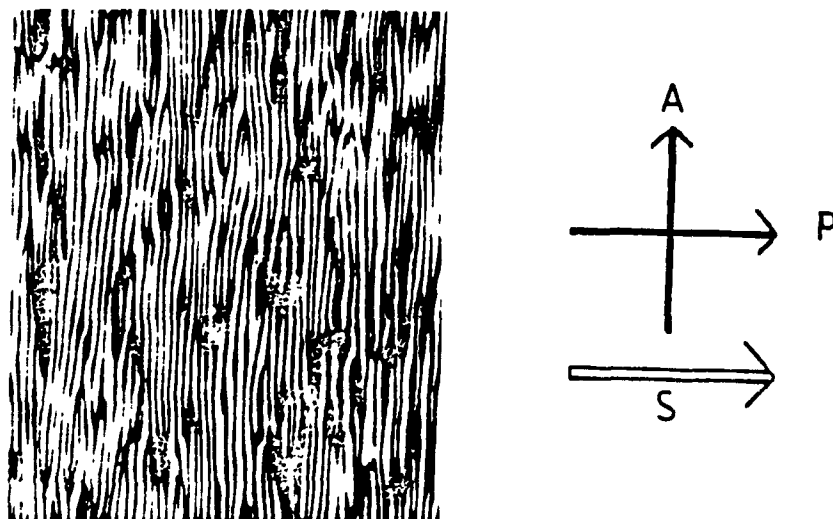


Figure 1.16. Banded texture seen between crossed polars after cessation of shear flow. A and P are the analyzer and polarizer, respectively, and S is the prior shearing direction. (Reprinted from Navard and Zachariades [51].)

There is a critical shear rate  $\dot{\gamma}_c$ , which is a property of the material being sheared, below which no bands appear after cessation of shear flow [53,54,56-60]. Furthermore, even when the applied shear rate  $\dot{\gamma}$  is greater than  $\dot{\gamma}_c$ , there is also a critical shearing time  $t_{sc}$ , which depends on  $\dot{\gamma}$  [53,54,56-60]. Figure 1.17 shows typical representations of experimental curves for these two conditions. At  $\dot{\gamma}_c$  and  $t_{sc}$ , the time for band formation

$t_b$  is infinite; therefore, the banded texture does not form below these critical values. Both these values are dependent on the molecular weight of the sample [53,56], but not on the concentration if it is a lyotropic LCP [56]. The applied shear rate, provided that the experimental conditions meet the critical values, also affects the width of the bright bands formed. With increasing rate of prior shear, the banded texture formed have better definitions and thinner bright bands [44]. For instance, Kiss and Porter [44] reported that for a 15 wt % poly- $\gamma$ -benzyl-L-glutamate (with molecular weight of 350 000)-dioxane solution, the bright bands are approximately  $3 \times 10^{-5}$  m wide for a low  $\dot{\gamma}$  but only  $1 \times 10^{-5}$  m for a high  $\dot{\gamma}$ ; no values were specified for these two shear rates. Navard and Zachariades [51] reported the same qualitative results for the thermotropic trifluoroacetoxypropylcellulose (TFAPC). Generally, the bright band width ranges from  $1 \times 10^{-6}$  m to  $3 \times 10^{-5}$  m [42,44,51,53,55-57,61,62] depending on the material and prior shearing conditions.

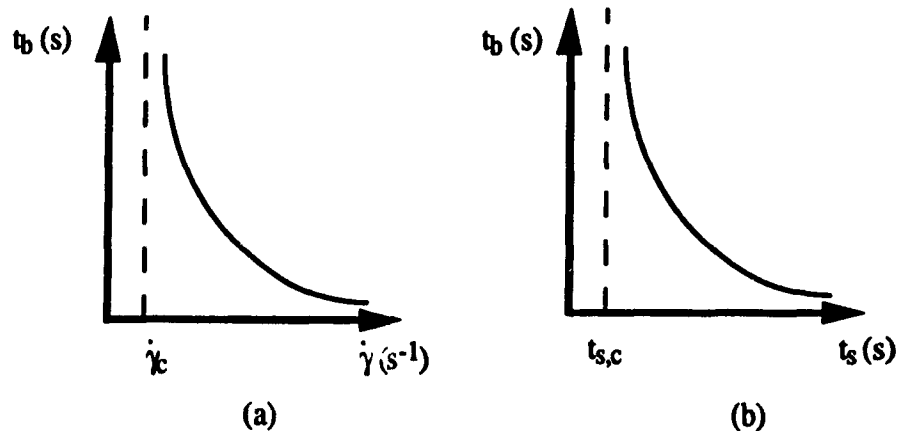


Figure 1.17. Typical representations of experimentally determined relations between the time for band formation  $t_b$  with (a) the applied shear rate  $\dot{\gamma}$  and (b) the shearing time  $t_s$ . The subscript c denotes the critical value.

As noted above, the time after cessation of shear for the banded texture to appear  $t_b$  depends on the prior shear rate. The time of duration of the banded texture  $t_d$  also depends on  $\dot{\gamma}$ . As  $\dot{\gamma}$  increases, both  $t_b$  and  $t_d$  decrease; i.e., with increasing prior shear rate, the banded texture forms more rapidly [44,54,56-60] and relaxes more quickly [44,54].

Navard [53] followed the disappearance of the banded texture for HPC until the sample reached its equilibrium state. Figure 1.18a shows the banded texture he obtained. After some time ( $t_d$ ), the bands begin to lose their parallelism and form a wavy banded structure as shown in Figure 1.18b, and, eventually, domains appear. After several hours, this structure is gradually transformed to an equilibrium globular texture as shown in Figure 1.18c.

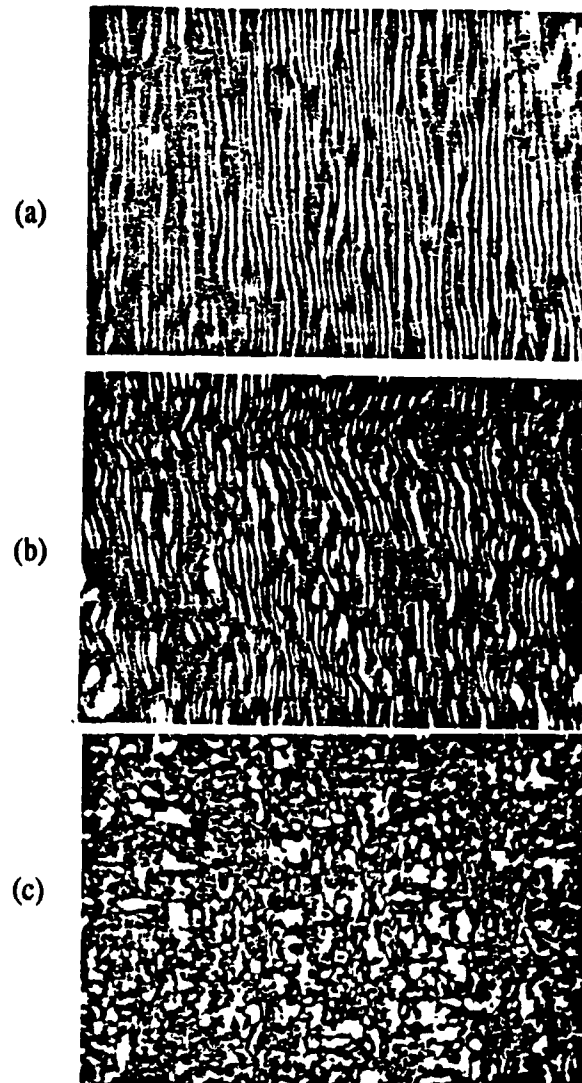


Figure 1.18. Time evolution of the banded texture seen after cessation of shear flow: (a) banded texture growth phase, (b) banded texture relaxation phase, and (c) equilibrium phase. (Reprinted from Navard [53].)

### 1.12.2 Director Structure Exhibiting the Banded Texture after Cessation of Shear Flow

The director structure that exhibits the banded texture when viewed between crossed polars follows a serpentine sinusoidal configuration [41,51]. Furthermore, the structure does not vary through the sample thickness [42,54,56]. The idea that the director is not confined to the sample plane was initially proposed by Viney *et al.* [41] using the results from their Zernicke phase contrast experiments. Furthermore, the use of a first order plate at  $45^\circ$  to the crossed polars shows the bright bands alternate between blue and yellow [41,51,62]. This means that along a bright band, the director is uniformly oriented, and that  $\mathbf{n}$  between two successive bright bands has opposite orientations [41,62,63]. Generally, the planar angle that extends from the prior shearing direction to the director ranges from  $8^\circ$  to  $45^\circ$  [41,42,51,53,57,62] depending on the material and prior shearing conditions.

### 1.12.3 Possible Explanations for the Formation of the Banded Texture after Cessation of Shear Flow

Recently, several investigators [54,58,60,61] reported the idea of stored elastic energy as the internal driving force for transient and spatially periodic director reorientation. This increase in elastic energy is due to defects being deformed and squeezed together into regions during shear flow [54,58,60]. Fincher [61], however, attributed this increase in elastic energy to simply a uniform distortion of the director out of the plane of shear during shear flow. Earlier attempted explanations centered on the idea that LCP's contract [50] or recoil [62] after cessation of shear flow. Despite being well characterized, however, no definite explanation has yet been reported on the mechanism of the transient banded texture formation after cessation of shear flow [56,60,61].

### 1.12.4 Importance of the Banded Texture Formed after Cessation of Shear Flow in Materials Processing

The primary reason that nematic polymers are gaining wide usage in a variety of applications, such as in the examples given in Section 1.1, is that they can have excellent mechanical properties if processed correctly. Shear flow is very common in the processing of nematic polymers into three-dimensional objects such as in injection molding, and because of this the molecules become highly oriented in the shearing

direction [64]. It is this shear flow-induced molecular orientation that gives these materials their excellent mechanical properties. Once the flow is stopped, the fabricated parts are being solidified, but the shear flow-induced molecular orientation is also decaying slowly [64]. During this relaxation, the banded texture described above may appear after some time ( $t_b$ ); therefore, the shear flow-induced molecular orientation is no longer present and the products will not have their excellent mechanical properties once solidification is over. Hence, it is of utmost importance to understand the cause and kinetics of the banded texture formed after cessation of shear flow in order to manufacture products from nematic polymers with excellent mechanical properties.

### **1.13 Thesis Outline and Objectives**

The understanding of the relaxation of nematic polymers after cessation of shear flow, as shown above, is of fundamental importance in the processing of these materials into manufactured products with excellent mechanical properties. The Leslie-Ericksen continuum theory describes very well the dynamics of conventional nematic phases, but the extent that this theory can be used for nematic polymers is still not known. Nevertheless, it has been used successfully to describe some phenomena of nematic polymers. Therefore, this theory is used in Chapter 2 to understand the macroscopic relaxation phenomena of nematic polymers after cessation of simple shear flow. This will cover objectives #1 and 2 of this thesis.

The recent theory of Ericksen is a more appropriate model to describe the complex behavior of nematic polymers, because it also takes into account spatial variations of the scalar order parameter which nematic polymers have during shear flow. Hence, it is intended to use this theory in Chapter 3 to describe the mechanism of the transient periodic (i.e., banded) texture formation after cessation of shear flow. This will cover objectives #3, 4 and 5 of this thesis.

The remaining parts of this thesis contain conclusions and recommendations (Chapter 4), and the appendices which contain the equations used in this thesis that are not presented in the chapters.

The objectives of this thesis are as follow:

- (1) To study the effects of backflows and defects on nematic polymer orientation after cessation of simple shear flow using the Leslie-Ericksen continuum theory.

- (2) To develop, implement and solve a macroscopic wall slip model describing the transient nematic polymer orientation.
- (3) To develop, implement and solve a model that studies the effect of the scalar order parameter on nematic polymer orientation after cessation of shear flow.
- (4) To determine the stability and cause of formation of the banded texture formed after cessation of shear flow.
- (5) To explain experimental observations reported in the literature on the banded texture formed after cessation of shear flow.

## **Chapter 2**

# **Relaxation Phenomena after Cessation of Simple Shear Flow for Perfectly Ordered Nematic Polymers**

### **2.1 Introduction**

Ever since the commercialization of Kevlar by DuPont in the early 1970's, nematic polymers are gaining wide usage in a variety of applications. Their popularity over that of conventional polymers is due to the fact that they can have superior mechanical properties if processed correctly. Shear flow deformations are invariably a part of nematic polymer processing, such as in the injection molding of three-dimensional objects. During the deformations, the molecules are oriented along the flow direction; it is this molecular alignment that gives nematic polymers their excellent mechanical properties. However, once the shear flow has stopped and heat treatment (i.e., solidification) has begun, the shear flow-induced molecular orientation begins to decay after some finite time [64]. The consequence of this is that the manufactured objects will not have the desired mechanical properties. Therefore, it is important to understand the relaxation phenomena of nematic polymers after cessation of shear flow.

This chapter studies the relaxation phenomena after cessation of simple shear flow for the typical nematic polymer PBG using the Leslie-Ericksen continuum theory and the Euler-Lagrange equation for surface motion. The simple shear flow configuration is

chosen because it is used quite often experimentally on LCP's [51,53,59-62], provides a shear flow deformation [65], and has practical utility in developing an understanding of the processing of nematic polymers. Although the extent in which the L-E continuum theory applies to nematic polymers is still not known yet, it has been used successfully to describe the magnetic reorientation of these materials [17]. The rest of this chapter consists of the development of the partial differential equations that describe the relaxation phenomena of nematic polymers after cessation of simple shear flow. It also contains results and discussion on the solutions of these equations under various conditions, and a section containing a summary and concluding remarks. This chapter studies specifically the effects that the surface conditions, defects and backflow, which are all present following shear flow, have on the equilibrium director orientation and the director orientational relaxation time. These two quantities are important, because, in the absence of any heat treatment, they define the state where the director inevitably relaxes to and a measure of how long it takes. This information is then helpful, as a first approximation since no heat treatment is considered, to those who want to manufacture objects with excellent mechanical properties from nematic polymers.

## 2.2 Balance Equations

The simple shear flow configuration is shown schematically in Figure 2.1. The phenomena are best described in Cartesian coordinates; therefore, the director field is defined as

$$\mathbf{n} = (\sin \theta \cos \phi, \sin \theta \sin \phi, \cos \theta) \quad (2.1)$$

where the unit length constraint,  $\mathbf{n} \cdot \mathbf{n} = 1$ , is automatically satisfied.

The following assumptions are used in this study:

- (1) The nematic polymer phase is perfectly ordered, and composed of rigid rod-like molecules; hence, the Leslie-Ericksen continuum theory can be used.
- (2) The relaxation phenomena are isothermal. This assumption is invariably made in modeling flows of nematic phases [31]. Consequently, the material physical constants, such as the Frank elastic constants and Leslie viscosities, are now constants.

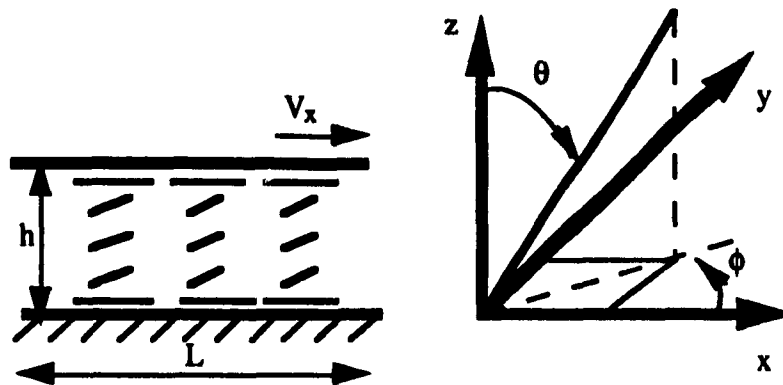


Figure 2.1. Schematic representation of the simple shear flow configuration, and definition of the Cartesian coordinate system. The plates are at  $z = 0$  and  $z = h$ .

- (3) The plates are infinitely wide; hence,  $\frac{\partial(*)}{\partial y} = 0$ , where  $(*)$  denotes a dependent variable.
- (4) There are no external body forces, such as the gravitational field. Hence,  $\mathbf{F} = 0$ .
- (5) The nematic polymer phase is incompressible [31]; i.e.  $\rho$  is a constant.
- (6) The director reorientation-induced backflow is a creeping flow; i.e., the viscous forces predominate over inertial forces. Therefore,  $\rho \dot{\mathbf{V}} = 0$ .
- (7) There are no flows along the  $x$ - and  $z$ -axes; i.e.,  $V_x = 0$  and  $V_z = 0$ . Since the backflow is director reorientation-induced, pressure does not affect the linear momentum balance.
- (8) There is no positional slip on the surfaces; this assumption holds well for viscous liquids and polymer melts [65].
- (9) The inertia of the director is small [66] and neglected.

The velocity field during the relaxation process then simplifies to

$$\mathbf{V} = (0, V_y, 0) \quad (2.2)$$

and the three dependent variables are as follow:

$$\theta = \theta (x, z, t) \quad (2.3a)$$

$$\phi = \phi (x, z, t) \quad (2.3b)$$

$$V_y = V_y (x, z, t) \quad (2.3c)$$

Since there are three unknowns, three equations are needed. They are the y-component of the linear momentum balance equation, and the y- and z-components of the internal angular momentum balance equation. The symbolic algebra program Theorist [67] is used to help derive these equations. To derive the y-component of the linear momentum balance equation, assumptions #1 to 7 given above, equations (1.6), (1.18) to (1.20), (1.23), and (2.1) to (2.3) are used. The final result of this derivation is

$$\begin{aligned} 0 = & \eta_1 \frac{\partial}{\partial x} \frac{\partial \phi}{\partial t} + \eta_2 \frac{\partial}{\partial x} \frac{\partial \theta}{\partial t} + \eta_3 \frac{\partial \phi}{\partial x} \frac{\partial \phi}{\partial t} + \eta_4 \frac{\partial \phi}{\partial x} \frac{\partial \theta}{\partial t} + \eta_5 \frac{\partial \theta}{\partial x} \frac{\partial \phi}{\partial t} + \\ & \eta_6 \frac{\partial \theta}{\partial x} \frac{\partial \theta}{\partial t} + \eta_7 \frac{\partial}{\partial z} \frac{\partial \phi}{\partial t} + \eta_8 \frac{\partial}{\partial z} \frac{\partial \theta}{\partial t} + \eta_9 \frac{\partial \phi}{\partial z} \frac{\partial \phi}{\partial t} + \eta_{10} \frac{\partial \phi}{\partial z} \frac{\partial \theta}{\partial t} + \\ & \eta_{11} \frac{\partial \theta}{\partial z} \frac{\partial \phi}{\partial t} + \eta_{12} \frac{\partial \theta}{\partial t} \frac{\partial \theta}{\partial z} + \eta_{13} \frac{\partial}{\partial x} \frac{\partial V_y}{\partial x} + \eta_{14} \frac{\partial}{\partial x} \frac{\partial V_y}{\partial z} + \eta_{15} \frac{\partial V_y}{\partial x} \frac{\partial \phi}{\partial x} + \\ & \eta_{16} \frac{\partial V_y}{\partial z} \frac{\partial \phi}{\partial x} + \eta_{17} \frac{\partial V_y}{\partial x} \frac{\partial \theta}{\partial x} + \eta_{18} \frac{\partial V_y}{\partial z} \frac{\partial \theta}{\partial x} + \eta_{19} \frac{\partial}{\partial z} \frac{\partial V_y}{\partial z} + \eta_{20} \frac{\partial V_y}{\partial x} \frac{\partial \phi}{\partial z} + \\ & \eta_{21} \frac{\partial V_y}{\partial z} \frac{\partial \phi}{\partial z} + \eta_{22} \frac{\partial V_y}{\partial x} \frac{\partial \theta}{\partial z} + \eta_{23} \frac{\partial V_y}{\partial z} \frac{\partial \theta}{\partial z} \end{aligned} \quad (2.4)$$

where the angle-dependent viscosity functions  $\{ \eta_i \}$ ,  $i = 1, \dots, 23$ , are given in Appendix A. Assumptions #1 to 3, 7 and 9, equations (1.20) to (1.24), and (2.1) to (2.3) are used to obtain the y- and z-components of the internal angular momentum balance equation. They are, respectively, expressed as follow:

$$\begin{aligned} \eta_{24} \frac{\partial \theta}{\partial t} = & \kappa_1 \left( \frac{\partial \phi}{\partial x} \right)^2 + \kappa_2 \frac{\partial}{\partial x} \frac{\partial \phi}{\partial x} + \kappa_3 \frac{\partial}{\partial x} \frac{\partial \phi}{\partial z} + \kappa_4 \left( \frac{\partial \phi}{\partial z} \right)^2 + \kappa_5 \frac{\partial}{\partial z} \frac{\partial \phi}{\partial z} + \\ & \kappa_6 \left( \frac{\partial \theta}{\partial x} \right)^2 + \kappa_7 \frac{\partial}{\partial x} \frac{\partial \theta}{\partial x} + \kappa_8 \frac{\partial}{\partial x} \frac{\partial \theta}{\partial z} + \kappa_9 \left( \frac{\partial \theta}{\partial z} \right)^2 + \kappa_{10} \frac{\partial}{\partial z} \frac{\partial \theta}{\partial z} + \end{aligned} \quad (2.5)$$

$$\begin{aligned}
& \kappa_{11} \frac{\partial \phi}{\partial x} \frac{\partial \phi}{\partial z} + \kappa_{12} \frac{\partial \phi}{\partial x} \frac{\partial \theta}{\partial x} + \kappa_{13} \frac{\partial \phi}{\partial z} \frac{\partial \theta}{\partial x} + \kappa_{14} \frac{\partial \phi}{\partial x} \frac{\partial \theta}{\partial z} + \kappa_{15} \frac{\partial \phi}{\partial z} \frac{\partial \theta}{\partial z} + \\
& \eta_{28} \frac{\partial \theta}{\partial x} \frac{\partial \theta}{\partial z} + \eta_{25} \frac{\partial \phi}{\partial t} + \eta_{26} \frac{\partial V_y}{\partial x} + \eta_{27} \frac{\partial V_y}{\partial z} \\
\eta_{28} \frac{\partial \phi}{\partial t} = & \kappa_{17} \left( \frac{\partial \phi}{\partial x} \right)^2 + \kappa_{18} \frac{\partial \phi}{\partial x} \frac{\partial \phi}{\partial x} + \kappa_{19} \frac{\partial \phi}{\partial x} \frac{\partial \phi}{\partial z} + \kappa_{20} \frac{\partial \phi}{\partial z} \frac{\partial \phi}{\partial z} + \kappa_{21} \left( \frac{\partial \theta}{\partial x} \right)^2 + \\
& \kappa_{22} \frac{\partial \theta}{\partial x} \frac{\partial \theta}{\partial x} + \kappa_{23} \frac{\partial \theta}{\partial x} \frac{\partial \theta}{\partial z} + \kappa_{24} \frac{\partial \phi}{\partial x} \frac{\partial \phi}{\partial z} + \kappa_{25} \frac{\partial \phi}{\partial x} \frac{\partial \theta}{\partial x} + \kappa_{26} \frac{\partial \phi}{\partial z} \frac{\partial \theta}{\partial x} + \\
& \kappa_{27} \frac{\partial \phi}{\partial x} \frac{\partial \theta}{\partial z} + \kappa_{28} \frac{\partial \theta}{\partial z} \frac{\partial \theta}{\partial z} + \kappa_{29} \frac{\partial \theta}{\partial x} \frac{\partial \theta}{\partial z} + \eta_{29} \frac{\partial V_y}{\partial x} + \eta_{30} \frac{\partial V_y}{\partial z}
\end{aligned} \tag{2.6}$$

where the angle-dependent elastic functions  $\{ \kappa_i \}$ ,  $i = 1, \dots, 29$ , and viscosity functions  $\{ \eta_i \}$ ,  $i = 24, \dots, 30$ , are also given in Appendix A. The material physical constants used in this study are for the polymer PBG [13], and are tabulated in Table 2.1.

Since there are two generalized coordinates here ( $\theta$  and  $\phi$ ), two Euler-Lagrange

Table 2.1  
Physical Constants for PBG [13]

Viscosities, N s m <sup>-2</sup>	
$\alpha_1$	- 3.66
$\alpha_2$	- 6.92
$\alpha_3$	$1.85 \times 10^{-2}$
$\alpha_4$	$3.48 \times 10^{-1}$
$\alpha_5$	6.61
$\alpha_6$	$-2.93 \times 10^{-1}$
$\gamma_1 = \alpha_3 - \alpha_2$	6.94
$\gamma_2 = \alpha_6 - \alpha_5$	- 6.90
Frank Elastic Constants, $\times 10^{-12}$ N	
$K_{11}$	12.1
$K_{22}$	0.78
$K_{33}$	7.63

equations governing surface motion are needed. Section 1.7 derives the Euler-Lagrange equation for the planar component of surface motion only; i.e., for  $\phi$ . To obtain the governing equation for the nonplanar component,  $\phi$  is replaced by  $\theta$  in the derivation of Section 1.7. Furthermore, in Section 1.7, it is assumed that any planar orientation is an easy axis so that the coupling energy is a minimum and can be neglected. Since the surface director need not be planar [25] and nonplanar easy axes also exist [14], it can be assumed that any surface orientation is an easy axis and, therefore, the coupling energy is a minimum which can be neglected. Hence, the results of the derivation using equations (1.6), (1.13), (1.14), (1.17) and (2.1) are as follow:

$$2 v_z \lambda^s \dot{\theta} = \kappa_{30} \frac{\partial \theta}{\partial z} + \kappa_{31} \frac{\partial \phi}{\partial x} + \kappa_{32} \frac{\partial \theta}{\partial x} \quad (2.7a)$$

$$2 v_z \lambda^s \dot{\phi} \sin^2 \theta = \kappa_{33} \frac{\partial \phi}{\partial z} + \kappa_{34} \frac{\partial \phi}{\partial x} + \kappa_{35} \frac{\partial \theta}{\partial x} \quad (2.7b)$$

where the angle-dependent elastic functions  $\{ \kappa_i \}$ ,  $i = 30, \dots, 35$ , are given in Appendix A. A superposed dot denotes time differentiation.  $v_z$  is the z-component of the outward unit normal vector to the plates; therefore,  $v_z = 1$  at  $z = h$  (top plate) and  $v_z = -1$  at  $z = 0$  (bottom plate). Since there are no known experimental values in the literature on the surface viscosities of nematic polymers,  $\lambda^s$  is allowed to sample the range from zero to infinity.  $\lambda^s = 0$  corresponds to an orientational free surface, and  $\lambda^s \Rightarrow \infty$  corresponds to fixed surface director orientation because, in this case,  $\frac{\partial \theta}{\partial t} = \frac{\partial \phi}{\partial t} = 0$ .

The initial and periodic boundary conditions are as follow:

$$\theta = \theta_1(x, z) \text{ at } t = 0, 0 \leq x \leq L, 0 \leq z \leq h \quad (2.8a)$$

$$\phi = \phi_1(x, z) \text{ at } t = 0, 0 \leq x \leq L, 0 \leq z \leq h \quad (2.8b)$$

$$V_y = 0 \text{ at } t = 0, 0 \leq x \leq L, 0 \leq z \leq h \quad (2.8c)$$

$$\frac{\partial \theta}{\partial x} = 0 \text{ at } t > 0, x = 0, 0 \leq z \leq h \quad (2.8d)$$

$$\frac{\partial \theta}{\partial x} = 0 \text{ at } t > 0, x = L, 0 \leq z \leq h \quad (2.8e)$$

$$\frac{\partial \phi}{\partial x} = 0 \text{ at } t > 0, x = 0, 0 \leq z \leq h \quad (2.8f)$$

$$\frac{\partial \phi}{\partial x} = 0 \text{ at } t > 0, x = L, 0 \leq z \leq h \quad (2.8g)$$

$$V_y = 0 \text{ at } t > 0, x = 0, 0 \leq z \leq h \quad (2.8h)$$

$$V_y = 0 \text{ at } t > 0, x = L, 0 \leq z \leq h \quad (2.8i)$$

$$-2 \lambda^s \dot{\theta} = \kappa_{30} \frac{\partial \theta}{\partial z} + \kappa_{31} \frac{\partial \phi}{\partial x} + \kappa_{32} \frac{\partial \theta}{\partial x} \text{ at } t > 0, 0 \leq x \leq L, z = 0 \quad (2.8j)$$

$$2 \lambda^s \dot{\theta} = \kappa_{30} \frac{\partial \theta}{\partial z} + \kappa_{31} \frac{\partial \phi}{\partial x} + \kappa_{32} \frac{\partial \theta}{\partial x} \text{ at } t > 0, 0 \leq x \leq L, z = h \quad (2.8k)$$

$$-2 \lambda^s \dot{\phi} \sin^2 \theta = \kappa_{33} \frac{\partial \phi}{\partial z} + \kappa_{34} \frac{\partial \phi}{\partial x} + \kappa_{35} \frac{\partial \theta}{\partial x} \text{ at } t > 0, 0 \leq x \leq L, z = 0 \quad (2.8l)$$

$$2 \lambda^s \dot{\phi} \sin^2 \theta = \kappa_{33} \frac{\partial \phi}{\partial z} + \kappa_{34} \frac{\partial \phi}{\partial x} + \kappa_{35} \frac{\partial \theta}{\partial x} \text{ at } t > 0, 0 \leq x \leq L, z = h \quad (2.8m)$$

$$V_y = 0 \text{ at } t > 0, 0 \leq x \leq L, z = 0 \quad (2.8n)$$

$$V_y = 0 \text{ at } t > 0, 0 \leq x \leq L, z = h \quad (2.8o)$$

Equations (2.4) to (2.6) and (2.8) are solved numerically in dimensionless form using the material physical constants for PBG. The scaling variables, dimensionless governing equations, and dimensionless initial and periodic boundary conditions are given in Appendix A. The Galerkin finite element method is used with ten linear basis functions over ten elements in each coordinate [68]. The time integrator is the first-order Euler predictor-corrector method [69], and the Newton-Raphson method is used for solving this system of nonlinear partial differential equations. For all calculations, the plate spacing is chosen as  $h = 5 \times 10^{-5}$  m, and the plate length is chosen as  $L = 3 \times h$ . The code is written in FORTRAN, and executed on the IBM 3090 S130 mainframe at McGill University. A copy of the code is available, upon request, from Prof. A. D. Rey.

## 2.3 Results and Discussion

This section presents predictions from the model outlined above. Comparisons between the predictions from this model and experimental observations can not be made because there are no known experimental reports in the literature. The analysis in this section is limited. It contains the essential effects that the surface conditions (surface viscosity), defects (surface irregularities) and backflow have on the equilibrium director orientation ( $\theta_{eq}$  and  $\phi_{eq}$ ) and the director orientational relaxation times ( $\tau_\theta$  and  $\tau_\phi$ ) after cessation of simple shear flow.

### 2.3.1 Effects of Surface Conditions

This section examines the effects that the surface conditions have on  $\theta_{eq}$ ,  $\phi_{eq}$ ,  $\tau_\theta$  and  $\tau_\phi$  during the relaxation stage after cessation of simple shear flow. The initial conditions for the director field are expressed as follow:

$$\theta = \frac{1}{2} \pi \text{ rad at } t = 0, 0 \leq x \leq L, z = 0 \quad (2.9a)$$

$$\theta = \frac{1}{2} \pi \text{ rad at } t = 0, 0 \leq x \leq L, z = h \quad (2.9b)$$

$$\theta = \frac{5}{12} \pi \text{ rad at } t = 0, 0 \leq x \leq L, 0 < z < h \quad (2.9c)$$

$$\phi = 0 \text{ rad at } t = 0, 0 \leq x \leq L, z = 0 \quad (2.9d)$$

$$\phi = 0 \text{ rad at } t = 0, 0 \leq x \leq L, z = h \quad (2.9e)$$

$$\phi = \frac{1}{36} \pi \text{ rad at } t = 0, 0 \leq x \leq L, 0 < z < h \quad (2.9f)$$

These initial conditions specify a typical director configuration that a nematic polymer possesses at sufficiently high shear rates [30,35,36,61], and is shown schematically in Figure 2.2. Since these initial conditions stipulate a uniform director rotation, except at the bounding surfaces where no rotations are initially present, the initial backflow  $V_y$  is zero everywhere. This has already been specified by equation (2.8c). Furthermore, there is no backflow on the surfaces because of the no slip condition.

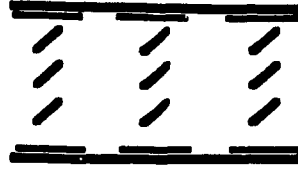


Figure 2.2. Schematic representation of a typical director configuration for a nematic polymer being sheared between parallel plates at high shear rates.

Figure 2.3 shows the time evolution of the tilt angle  $\theta$  (first row), twist angle  $\phi$  (second row) and dimensionless velocity  $V_y^*$  (third row) profiles along the dimensionless length  $x^* = \frac{x}{h}$  after cessation of simple shear flow at a dimensionless height of  $z^* = \frac{z}{h} = 0$  (first column),  $z^* = 0.1$  (second column),  $z^* = 0.3$  (third column) and  $z^* = 0.5$  (fourth column). The parameter is time, and the dimensionless surface viscosity is  $\lambda^{s*} = 1$ . Only the results from the bottom half of the simple shear flow configuration, as shown in Figure 2.1, are given because the results are symmetric about the midplane ( $z^* = 0.5$ ). The initial conditions, given by equation (2.9), specify director gradients near the bounding surfaces (see Figure 2.2), and uniform bulk orientation. These gradients translate into elastic director distortions, which, consequently, raise the elastic free energy of the system as shown at time  $t = 0$  s in Figure 2.4. To lower this stored free energy, the directors on the surface and in the bulk but adjacent to the surface, which is approximated as  $z^* = 0.1$  in this study, reorient toward each other. Since a nematic phase transmits torques [14], the act of director reorientation near the surface diffuses through the sample thickness. Consequently, all the bulk directors reorient. This phenomenon is evident in this model primarily through:

- (1) the  $\kappa_4$ ,  $\kappa_5$ ,  $\kappa_9$ ,  $\kappa_{10}$  and  $\kappa_{15}$  terms in equation (2.5),
- (2) the  $\kappa_{20}$  and  $\kappa_{28}$  terms in equation (2.6), and
- (3) the  $\kappa_{30}$  and  $\kappa_{33}$  terms in equations (2.8j) to (2.8m).

In addition, Figure 2.3 shows that the directors closest to the surface relax first, and the directors in the midplane ( $z^* = 0.5$ ) relax last to equilibrium. This is due to the fact that the driving force for director reorientation, which are the director gradients, is located adjacent to the surface. In addition, it also takes time to transmit the director reorienting torques from the surface into the bulk. The nine  $\kappa$  terms mentioned above, along with the  $\eta_{24}$  term in equation (2.5) and the  $\eta_{28}$  term in equation (2.6), show that these ideas are contained in this model. Figure 2.3 also shows that the directors relax almost uniformly at each  $z^*$  and for each time step. The word *almost* is used to describe the director

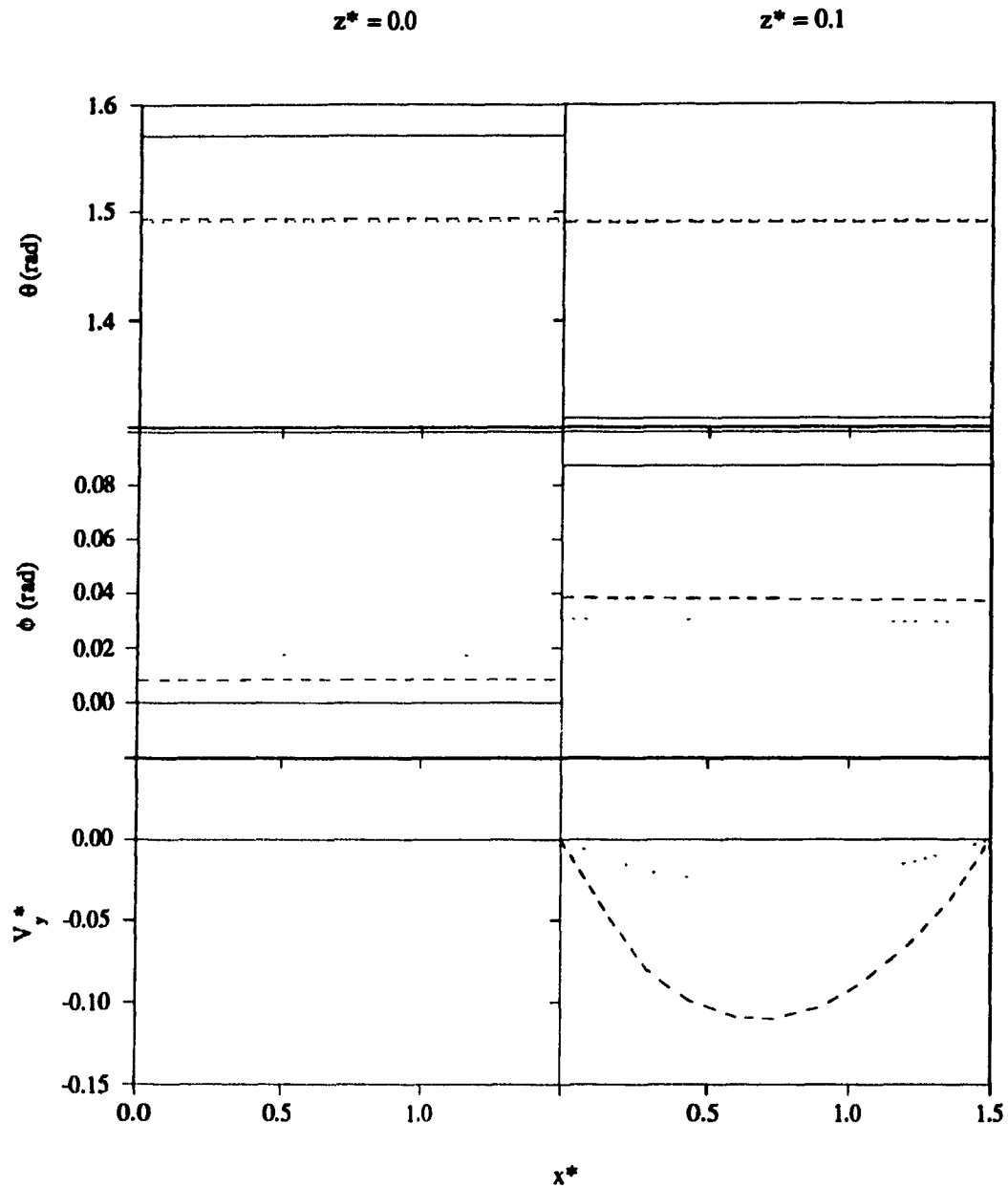


Figure 2.3 (continued on next page). Tilt angle  $\theta$  (first row), twist angle  $\phi$  (second row) and dimensionless velocity  $V_y^*$  (third row) spatial profiles at dimensionless heights of  $z^* = 0.0$  (first column),  $z^* = 0.1$  (second column),  $z^* = 0.3$  (third column) and  $z^* = 0.5$  (fourth column). The times are:  $t = 0$  s (—),  $t = 372$  s (-----), and  $t = 1413$  s (·····).

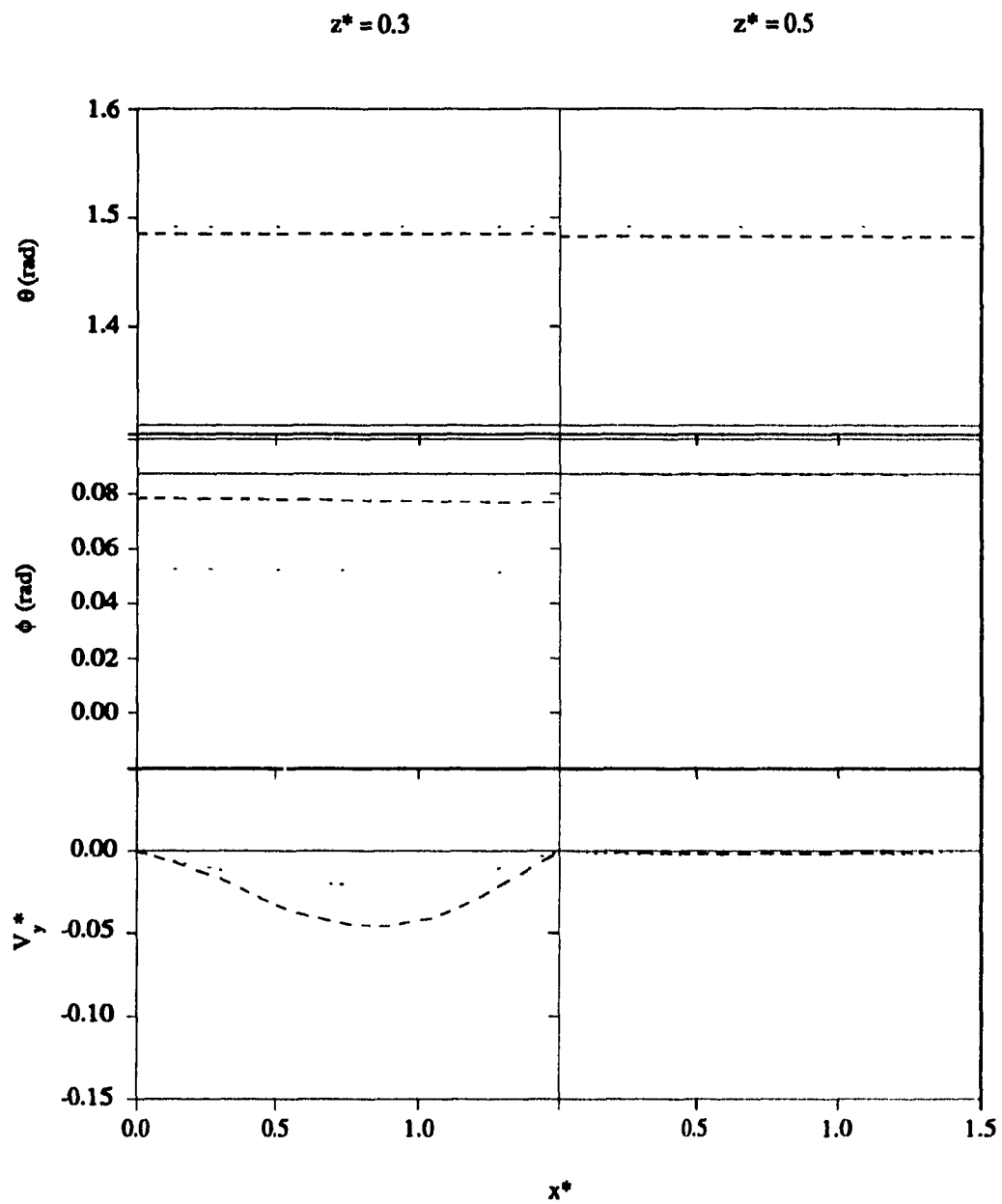


Figure 2.3 (continued).

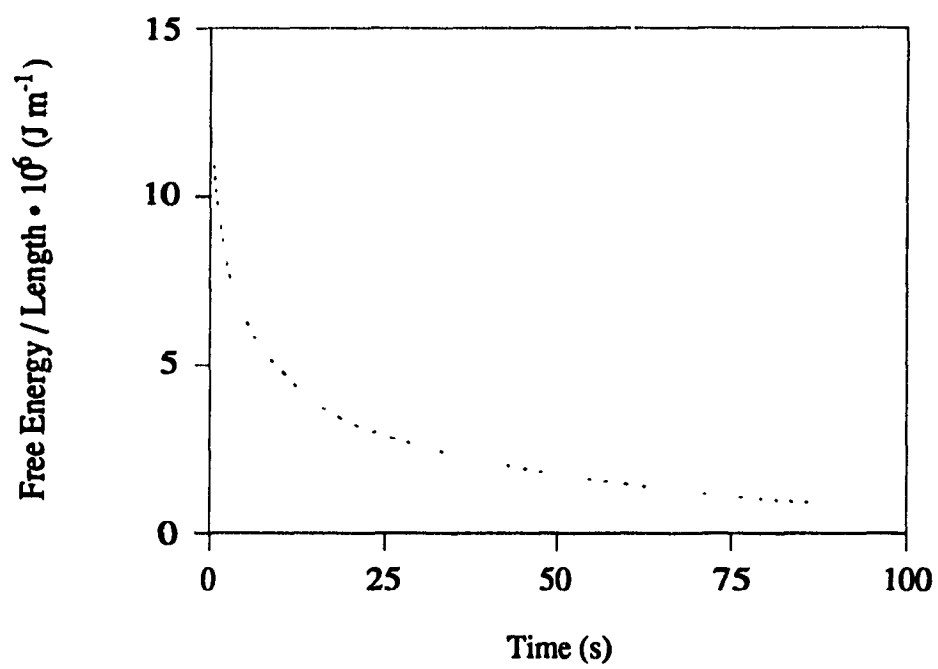


Figure 2.4. Transient relaxation of the stored elastic free energy per unit length.

orientation, because director gradients are needed to create the backflows shown in the bottom row of this figure. Backflow is not created at  $z^* = 0.0$  because of the no slip condition. The nonuniformity in the director field and the shape of the dimensionless velocity profile are attributed primarily to the periodic boundary conditions; i.e., equations (2.8d) to (2.8i). The maximum magnitude of the velocity profile is a measure of the rate of director reorientation; the faster the director rotates, the stronger is the reorientation induced-backflow. Figure 2.3 shows that the directors rotate the fastest at  $z^* = 0.1$ , and the slowest at the midplane where little director reorientation-induced backflow is created; this is consistent with the aforesaid discussion. Lastly, in the order of tens of minutes, the directors reorient to an equilibrium state. In this state, the director orientation is given by  $\theta_{eq} \cong 1.492$  rad and  $\phi_{eq} \cong 0.026$  rad, and has no elastic free energy (Figure 2.4). Therefore, during the relaxation phenomena after cessation of simple shear flow, the directors reorient to minimize the shear flow induced-elastic free energy.

Figure 2.5 shows the dependence of the tilt angle (top graph) and twist angle (bottom graph) relaxation times on the dimensionless surface viscosity. The parameter is the dimensionless height. The relaxation times are defined to be the times for  $\theta$  and  $\phi$  to attain a state of 63.2 % of the difference between their initial and equilibrium values [70]. Once more the phenomenon that directors relax fastest at  $z^* = 0.1$  and slowest at  $z^* = 0.5$  is present, which is characteristic of the given initial conditions, as evident in Figure 2.5. Figure 2.6 shows the dependence of the final orientation,  $\theta_{eq}$  (top graph) and  $\phi_{eq}$  (bottom graph), on  $\lambda^{s^*}$ .

There are three points that are of interest in Figures 2.5 and 2.6. Firstly, at each  $z^*$  and  $\lambda^{s^*}$ ,  $\tau_\phi$  is longer than  $\tau_\theta$ . This is due to the fact that the splay and bend elastic constants are each about ten times greater than the twist elastic constant, and that the initial conditions contain more splay than twist director deformations. Hence, the system tries to relax the splay and bend distortions first since they cost more energetically. The second point to note is the effect of  $\lambda^{s^*}$  on the relaxation times and equilibrium angles. Figure 2.6 shows that the equilibrium angles are closest to the initial bulk angles but furthest away from the initial surface angles when  $\lambda^{s^*} = 0$ . Upon increasing the magnitude of  $\lambda^{s^*}$ , the equilibrium orientation begins moving away from the initial bulk orientation, but approaches the initial surface orientation. At  $\lambda^{s^*} \Rightarrow \infty$ , the equilibrium orientation is parallel to the initial surface director orientation. In short then, the equilibrium director orientation is governed by the surface conditions, which are given in this model by equations (2.8j) to (2.8m). There is maximum director reorientation on the surfaces when  $\lambda^{s^*} = 0$ . Conversely, there is minimum (no) director reorientation on the

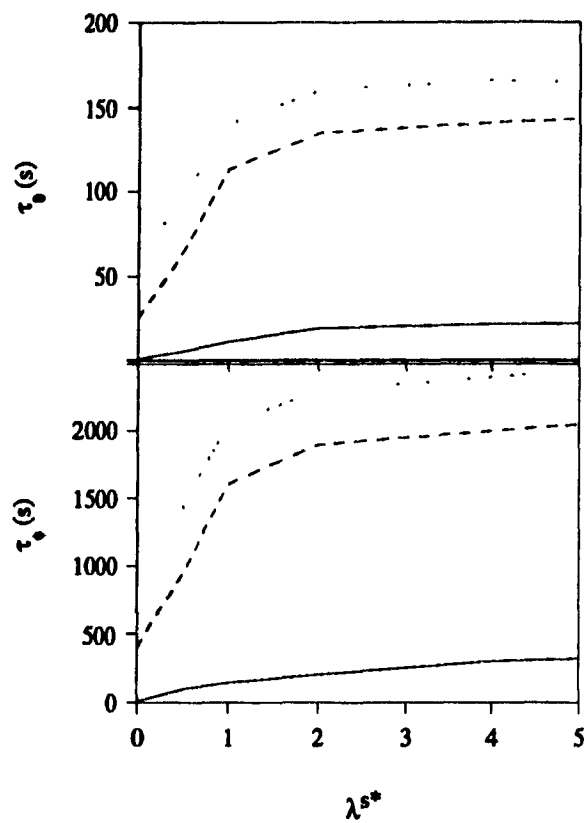


Figure 2.5. The dependence of the tilt angle relaxation time  $\tau_\theta$  (top graph) and twist angle relaxation time  $\tau_\phi$  (bottom graph) on the dimensionless surface viscosity  $\lambda^{S*}$ . The dimensionless heights are:  $z^* = 0.1$  (—),  $z^* = 0.3$  (-----), and  $z^* = 0.5$  (.....).

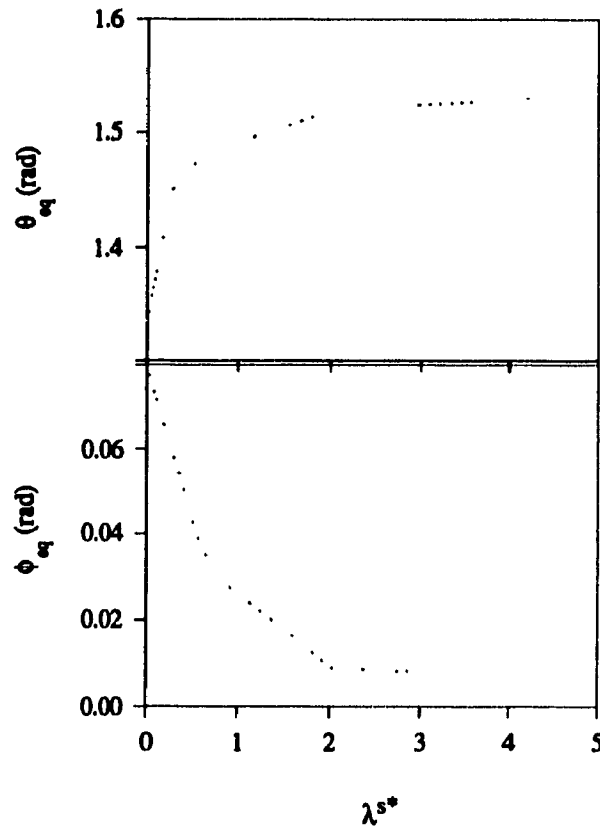


Figure 2.6. The dependence of the equilibrium tilt angle  $\theta_{eq}$  (top graph) and equilibrium twist angle  $\phi_{eq}$  (bottom graph) on the dimensionless surface viscosity  $\lambda^{s*}$ .

surfaces when  $\lambda^{s*} \Rightarrow \infty$ ; i.e.,  $\frac{\partial \theta}{\partial t} = 0$  and  $\frac{\partial \phi}{\partial t} = 0$ . Figure 2.5 shows that upon increasing  $\lambda^{s*}$ ,  $\tau_\theta$  and  $\tau_\phi$  increase. This is consistent with the results given in Figure 2.6. Upon increasing  $\lambda^{s*}$ , surface director reorientation decreases to the point where no reorientation is permitted at  $\lambda^{s*} \Rightarrow \infty$ . The relaxation times are then fastest at  $\lambda^{s*} = 0$  since the surface directors reorient freely towards the bulk directors, which themselves reorient minimally. On the other hand, when  $\lambda^{s*} \Rightarrow \infty$ , all the bulk directors must reorient to the surface director orientation. As discussed above, it takes time to transmit torques over distance from the surface into the bulk; therefore, the relaxation times are longest for fixed anchoring conditions.

The last point of interest is that  $\tau_\theta$ ,  $\tau_\phi$ ,  $\theta_{eq}$  and  $\phi_{eq}$  vary dramatically within the range  $0 \leq \lambda^{s*} \leq 2$ , but then only slowly and slightly for  $\lambda^{s*} > 2$ . This can be explained by comparing the magnitudes of the surface and bulk viscosities. The dimensionless surface viscosity is defined as

$$\lambda^{s*} = 2 \frac{\left(\frac{\lambda^s}{h}\right)}{\gamma_1} \quad (2.10)$$

Notice the units of  $\lambda^s$  is  $N \ s \ m^{-1}$ , and not the usual bulk viscosity units of  $N \ s \ m^{-2}$ . To then compare magnitudes of viscosities, the quotient  $\left(\frac{\lambda^s}{h}\right)$  should be used instead of simply  $\lambda^s$ . If  $\lambda^{s*} < 2$ , then  $\gamma_1 > \left(\frac{\lambda^s}{h}\right)$  and surface director reorientation is easier than bulk director reorientation. Conversely, if  $\lambda^{s*} > 2$ , then  $\left(\frac{\lambda^s}{h}\right) > \gamma_1$  and bulk director reorientation is now easier than surface director reorientation. Hence, the value  $\lambda^{s*} = 2$  can then be thought of as a critical point separating two different types of dependence on  $\lambda^{s*}$  as described above.

### 2.3.2 Effects of Defects

Defects, as already defined in Section 1.9, are points and lines (or disclinations) where the director field changes discontinuously [14]. This section examines the effects that defects have on  $\tau_\phi$  and  $\phi_{eq}$  by using two simple types of irregularities in the surface director configuration. The initial conditions of the director field in these two cases are expressed as follow:

Case 1

$$\theta = \frac{1}{2} \pi \text{ rad at } t = 0, 0 \leq x \leq L, 0 \leq z \leq h \quad (2.11a)$$

$$\phi = 0 \text{ rad at } t = 0, 0 \leq x \leq L, 0 < z < h \quad (2.11b)$$

$$\phi = 0 \text{ rad at } t = 0, 0 \leq x < \frac{1}{2}L \cup \frac{1}{2}L < x \leq L, z = 0 \quad (2.11c)$$

$$\phi = 0 \text{ rad at } t = 0, 0 \leq x < \frac{1}{2}L \cup \frac{1}{2}L < x \leq L, z = h \quad (2.11d)$$

$$\phi = \frac{1}{2} \pi \text{ rad at } t = 0, x = \frac{1}{2}L, z = 0 \quad (2.11e)$$

$$\phi = \frac{1}{2} \pi \text{ rad at } t = 0, x = \frac{1}{2}L, z = h \quad (2.11f)$$

Case 2

$$\theta = \frac{1}{2} \pi \text{ rad at } t = 0, 0 \leq x \leq L, 0 \leq z \leq h \quad (2.12a)$$

$$\phi = 0 \text{ rad at } t = 0, 0 \leq x \leq L, 0 < z < h \quad (2.12b)$$

$$\phi = 0 \text{ rad at } t = 0, 0 \leq x < 0.3125L \cup 0.3125L < x < 0.6875L \cup \\ 0.6875L < x \leq L, z = 0 \quad (2.12c)$$

$$\phi = 0 \text{ rad at } t = 0, 0 \leq x < 0.3125L \cup 0.3125L < x < 0.6875L \cup \\ 0.6875L < x \leq L, z = h \quad (2.12d)$$

$$\phi = \frac{1}{2} \pi \text{ rad at } t = 0, x = 0.3125L \text{ and } 0.6875L, z = 0 \quad (2.12e)$$

$$\phi = \frac{1}{2} \pi \text{ rad at } t = 0, x = 0.3125L \text{ and } 0.6875L, z = h \quad (2.12f)$$

The director configurations for these two cases are depicted schematically in Figure 2.7. Since there are no director rotations initially, except at the bounding surfaces, the initial backflow  $V_y$  is everywhere zero. This is specified by equation (2.8c); there is no

backflow on the surfaces because of the no slip condition. These two types of surface irregularities are motivated by the work of Currie and Leslie [71]. They predicted evenly spaced disclinations running along the width of the plates.

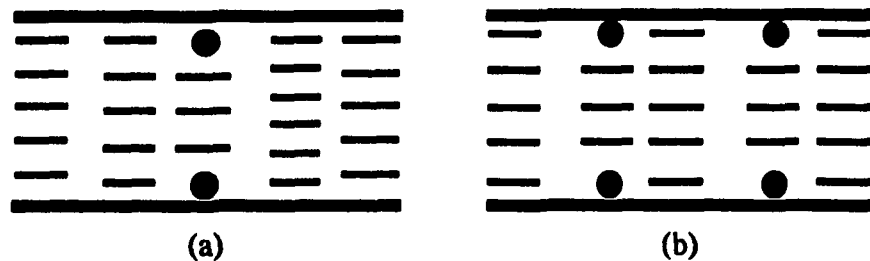


Figure 2.7. Schematic representations of the director configurations containing surface disclinations for (a) Case 1, and (b) Case 2.

Figure 2.8 shows the time evolution of the tilt angle  $\theta$  (first row), twist angle  $\phi$  (second row) and dimensionless velocity  $V_y^*$  (third row) spatial profiles for Case 2 at a dimensionless height of  $z^* = 0.0$  (first column),  $z^* = 0.1$  (second column),  $z^* = 0.3$  (third column) and  $z^* = 0.5$  (fourth column). The parameter is time, and the dimensionless surface viscosity is  $\lambda^{S^*} = 1$ . Once again, only the results from the bottom half of the simple shear flow configuration are given because the results are symmetric about the midplane ( $z^* = 0.5$ ). There are two intriguing points to note from the results contained in this figure. The directors are not tilted in the stressed state ( $t = 0$ ), but are tilted during the relaxation phase ( $t > 0$ ). The exception to this is at the midplane, where no noticeable tilt is observed. The director field reorients in this manner so as to release the stored elastic free energy as fast as possible (Figure 2.9). This phenomenon is contained primarily in this model by:

- (1) the  $\kappa_1, \kappa_2, \kappa_3, \kappa_4, \kappa_5$  and  $\kappa_{11}$  terms in equation (2.5), and
- (2) the  $\kappa_{31}$  term in equation (2.8j) and (2.8k).

Thus, any spatial gradients in the twist angle  $\phi$  causes the directors to tilt. This then explains why no noticeable tilt is observed at  $z^* = 0.5$ ; there is no significant twist angle gradient here. This leads to the next point.

Secondly, it is noted here as well (see Section 2.3.1) that the director reorientation dynamics are very slow at  $z^* = 0.5$ . This is evident by observing principally the dimensionless velocity profile. High rates of director reorientation create strong

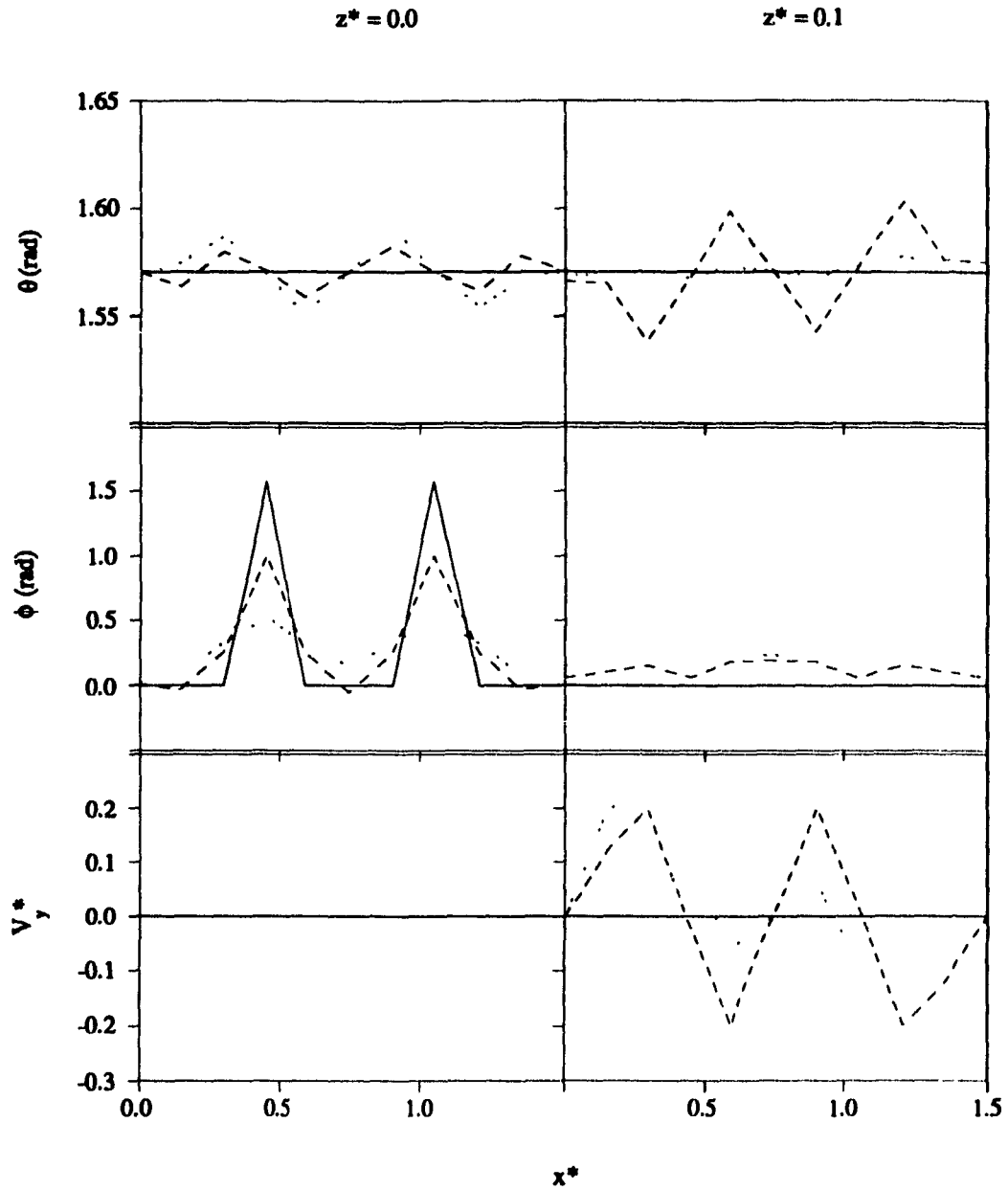


Figure 2.8 (continued on next page). Tilt angle  $\theta$  (first row), twist angle  $\phi$  (second row) and dimensionless velocity  $V_y^*$  (third row) spatial profiles at dimensionless heights of  $z^* = 0.0$  (first column),  $z^* = 0.1$  (second column),  $z^* = 0.3$  (third column) and  $z^* = 0.5$  (fourth column). The times are:  $t = 0$  s (—),  $t = 158$  s (---), and  $t = 623$  s (-·-·-).

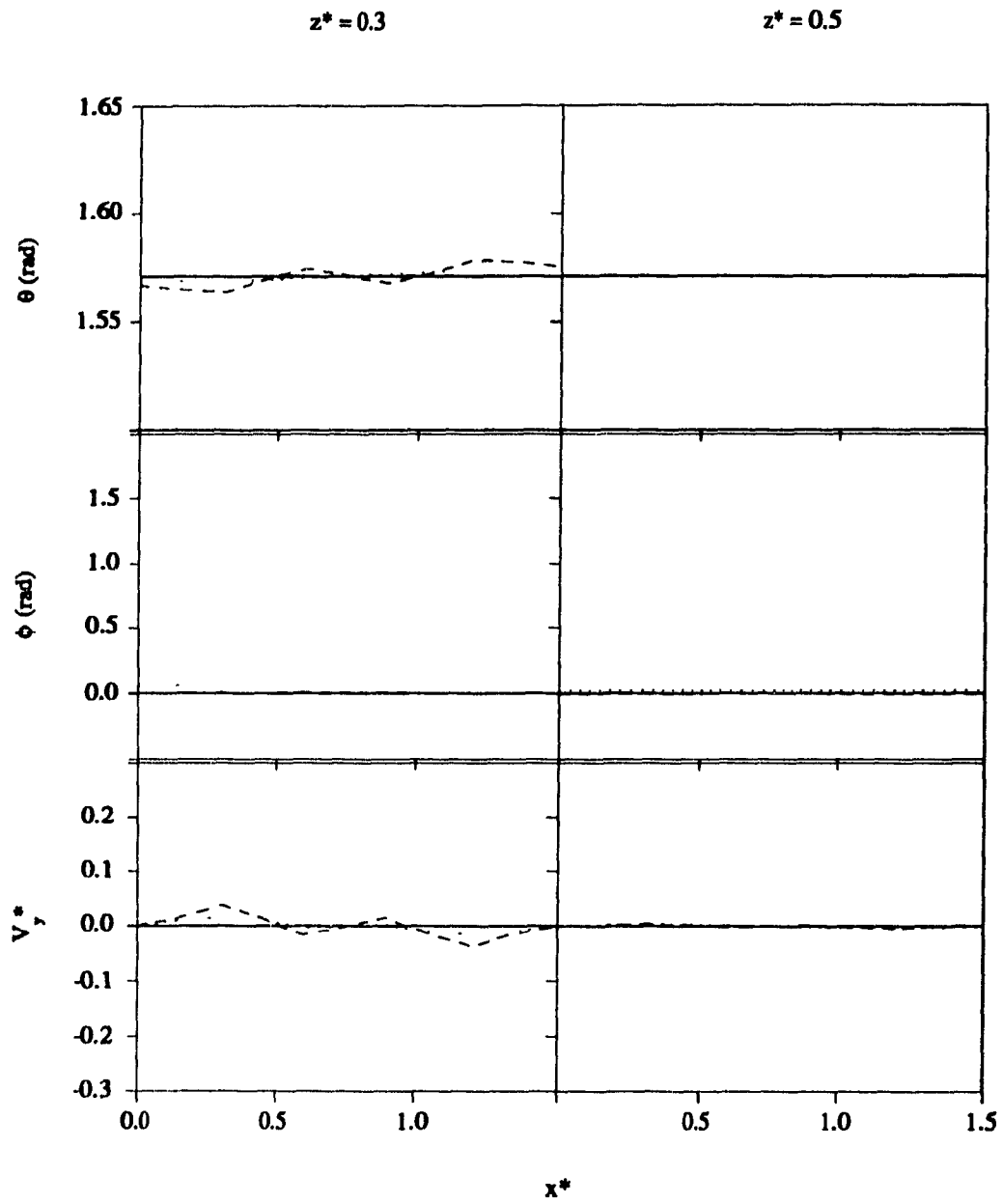


Figure 2.8 continued.

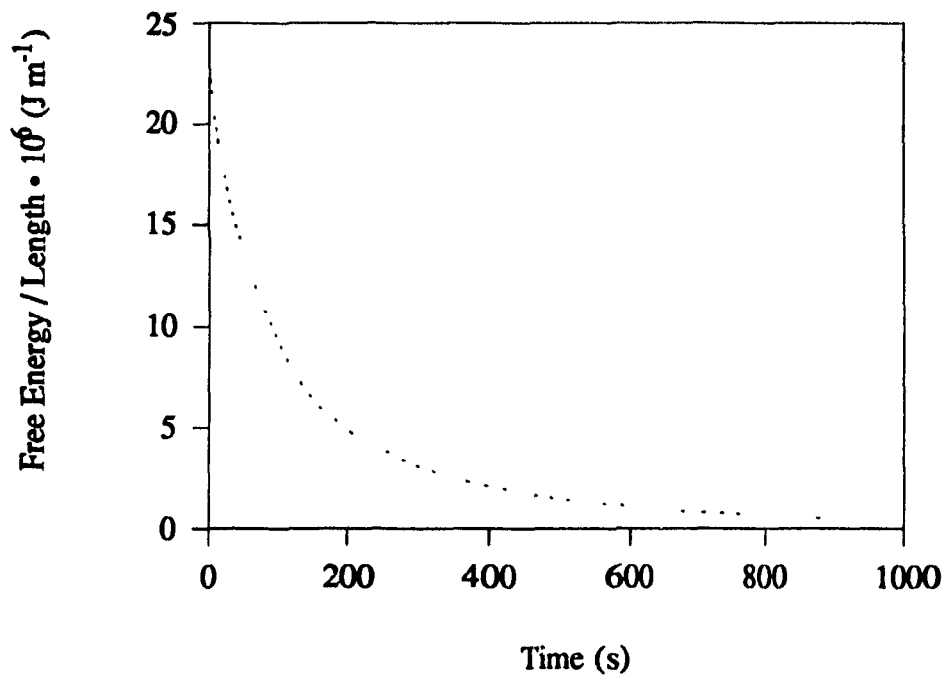


Figure 2.9. Transient relaxation of the stored elastic free energy per unit length.

backflow (see  $z^* = 0.1$ ); however, the backflow at  $z^* = 0.5$  is insignificant. This is due to the fact that the driving force for director reorientation (director gradients) is located near the surfaces, and that it takes time to transmit these reorienting torques over distance from the surfaces into the bulk.

The relaxation time and equilibrium value for  $\phi$  are given in Table 2.2. Values of  $\tau_\phi$  for other thickness levels are not reported. This is due to the difficulties encountered in trying to find these values embedded in the complex reorientation dynamics of these two systems (see Figure 2.8). The presence of disclinations during simple shear flow then prevents the equilibrium director field after cessation of flow to lie within the prior shear plane; i.e., the  $x,z$ -plane. In addition, this phenomenon is not affected by the surface conditions ( $\lambda^{s^*}$ ). Even for fixed anchoring at the surfaces ( $\lambda^{s^*} \Rightarrow \infty$ ), there will still be out of shear plane components; however, due to the nonuniformity of the initial conditions of the surface directors, the resulting equilibrium configuration is not uniform.

Table 2.2  
Relaxation Time ( $\tau_\phi$ ) and Equilibrium Value ( $\phi_{eq}$ ) for  
the Twist Angle ( $\phi$ ) at the Midplane ( $z^* = 0.5$ )

Case	$\tau_\phi$ (s)		$\phi_{eq}$ (rad)	
	(with backflow)	(without backflow)	(with backflow)	(without backflow)
1	2220	2440	0.0686	0.0686
2	2000	2270	0.1377	0.1377

Table 2.2 also shows that  $\tau_\phi$  for Case 2 is faster than that for Case 1 despite containing more defects and a larger equilibrium twist angle (see Section 2.3.1). The underlying reason for this is that the reorientation induced-backflow is stronger in Case 2, because of the presence of more defects in this case. As the director field around the disclination relaxes to equilibrium, backflow is created. When the surface disclinations

move closer to each other, as in going from Case 1 to Case 2, the resulting backflow then becomes stronger. Since backflow and director reorientation are coupled, the rate that the director relaxes to equilibrium is increased with increasing backflow strength. This effect of backflow is further considered in the next section.

### 2.3.3 Effects of Backflow

This section investigates the effects that the presence of the director reorientation-induced backflow have on  $\tau_\phi$  and  $\phi_{eq}$ . Figure 2.10 shows results for  $\tau_\phi$  using the initial conditions from Section 2.3.1 and  $\lambda^{S*} = 1$ . Furthermore, Table 2.2 gives  $\tau_\phi$  for the initial director fields and conditions used in Section 2.3.2. It is noticed rather quickly that the presence of backflow does have an impact on the dynamics of the director reorientation process. Backflow increases the rate of reorientation, which results in shorter relaxation times. The equilibrium state, however, is not affected if the backflow is not present. The consequence is that it will only take longer to reach the equilibrium orientation. This transient shear flow is a result of the intimate coupling between flow and orientation. In short, backflow relaxes the constraint on director rotation, which is the rotational viscosity  $\gamma_1$  [72]; hence, the rate of director reorientation after cessation of simple shear flow is increased.

## 2.4 Summary and Concluding Remarks

This chapter examined numerically the consequences that the surface conditions ( $\lambda^S$ ), defects (surface irregularities) and backflow ( $V_y$ ) have on the relaxation phenomena ( $\tau_\theta$ ,  $\tau_\phi$ ,  $\theta_{eq}$  and  $\phi_{eq}$ ) after cessation of simple shear flow for the typical nematic polymer PBG. The Leslie-Ericksen continuum theory and the Euler-Lagrange equations for surface motion were derived and used for this purpose.

The conclusions from this chapter are as follow:

- (1) The director relaxation time and equilibrium director orientation vary with the surface viscosity. For the initial conditions used in this study, the variation is strong when  $\gamma_1 > \frac{\lambda^S}{h}$ , but weak when  $\frac{\lambda^S}{h} > \gamma_1$ . In addition, as  $\lambda^S$  increases,  $\tau_\theta$  and  $\tau_\phi$  also increase, and the equilibrium director orientation approaches the initial surface orientation.

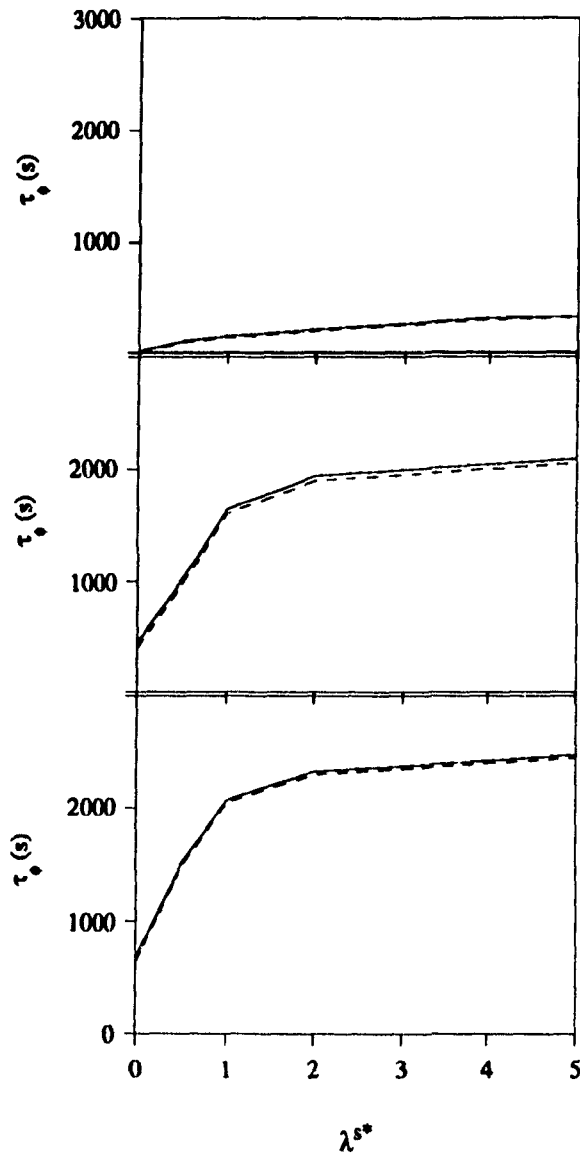


Figure 2.10. The dependence of the twist angle relaxation time  $\tau_\phi$  on the dimensionless surface viscosity  $\lambda^{s*}$  when backflow is present (----) and absent (—). The dimensionless heights are:  $z^* = 0.1$  (top graph),  $z^* = 0.3$  (middle graph), and  $z^* = 0.5$  (bottom graph).

- (2) The presence of surface disclinations, as described in Section 2.3.2, prevents the equilibrium director orientation from lying within the shear plane. At a given  $\lambda^s$ ,  $\tau_\phi$  decreases and  $\phi_{eq}$  increases with increasing number of surface disclinations.
- (3) The director reorientation induced-backflow relaxes the constraint for director rotation; consequently, the rate of director reorientation increases. Backflow, however, does not affect the resulting equilibrium configuration.
- (4) This model does not predict the growth of a serpentine sinusoidal director configuration. Therefore, it can not explain the formation of the banded texture that nematic polymers exhibit when observed between crossed polars after cessation of simple shear flow (see Section 1.12).

## **Chapter 3**

# **Relaxation Phenomena after Cessation of Shear Flow for Partially Ordered Nematic Polymers**

### **3.1 Introduction**

During the past two decades, nematic polymers have been replacing conventional materials in the manufacturing of various products. For instance, to name a few, nematic polymers are used to make bullet proof vests, brake linings, radial tires, tennis rackets and pressure vessels. The wide and popular usage of these novel high performance materials is due to the excellent mechanical properties they can have when processed correctly. Shear flow deformations are invariably a part of nematic polymer processing, such as in the injection molding of three dimensional objects. During these deformations, the molecules are highly oriented along the flow direction; it is this shear flow-induced molecular orientation that gives nematic polymers their excellent mechanical properties. However, once the flow has stopped and heat treatment (i.e., solidification) has begun, the shear flow-induced molecular orientation decays away slowly [64]. During the relaxation period, the directors may reorient into a periodic pattern along the prior shear flow direction after some finite time [53,54,56-60]. This periodic pattern is due to a serpentine sinusoidal director field [41,51], and is known as the banded texture [40-62]. The banded texture is described in Section 1.12. Consequently, the shear flow-induced molecular orientation is no longer present, and the manufactured products will not have

the desired excellent mechanical properties once solidification is over. Therefore, it is of utmost importance to understand the cause and kinetics of the banded texture formed after cessation of shear flow in order to manufacture products from nematic polymers with excellent mechanical properties.

The study in Chapter 2 shows that the Leslie-Ericksen continuum theory can not be used to predict the formation of the banded texture after cessation of shear flow for nematic polymers. This important conclusion, by no means, comes as a total surprise, because the extent to which this theory applies to nematic polymers is still not known yet. The inadequacy of this theory is due to the fact that it does not take into account the scalar order parameter  $S$ . Shear flow affects  $S$  in nematic polymers, which can imply spatial variations of  $S$  [30]. This idea of spatial variations of  $S$  is also supported by the predicted periodic temporal oscillations of  $S$  in monodomain and spatially invariant nematic polymer systems during shear flow [30,35,36]. Consequently, this chapter studies the relaxation phenomena and pattern formation after cessation of shear flow for a typical nematic polymer using the more general Ericksen and Landau-de Gennes nematic continuum theories. Furthermore, this chapter examines specifically the effects that an initial periodic spatial variation of  $S$  (i.e., base value  $S_0$  and amplitude  $A_S$ ) have on the time for pattern formation  $t_p$  and the maximum planar orientation  $\phi_m$  (see Figure 2.1) in the resulting transient periodic director configuration. These two quantities are important because, in the absence of any heat treatment, they give a measure of how long the directors remain oriented in the shear flow direction and how much the directors can rotate away from this direction. This information is then helpful, as a first approximation since no heat treatment and only planar director orientation are considered, to those who want to manufacture objects with excellent mechanical properties from nematic polymers.

The rest of this chapter consists of the development of the partial differential equations that govern the relaxation phenomena of nonhomogeneously ordered nematic polymers after cessation of shear flow. It also contains results, physical and mathematical interpretations of these results, discussions on the solutions of these equations under various conditions, and a section containing a summary and concluding remarks.

### 3.2 Balance Equations

The following assumptions are used in this study:

- (1) The nematic polymer phase is composed of rigid rod-like molecules; hence, the Ericksen continuum theory can be used.

(2) Figure 3.1 shows the dependence of the viscosities  $\{\alpha_i^S\}$ ,  $i = 1, \dots, 6$ , for the nematic polymer poly(4,4'-dioxy-2,2'-dimethyl azoxybenzene dodecanediyl) (DDA9) [73] whose values were used in this study. The complex relations for the dependence of the viscosities on  $S$  are specified by Edwards *et al.* [38], and are given in Appendix B. The values reported by Martins *et al.* [73] are taken to be at  $S = 1$  in Figure 3.1. This figure shows that there is a dependence of the viscosities on  $S$  in the desired working range of  $0.35 \leq S \leq 0.75$ . For simplicity, however, it is assumed that  $\alpha_i^S \neq \alpha_i^S(S)$  in this study. Hence, the viscosities will not be denoted with the superscript  $S$  below.

(3) The relaxation phenomena are isothermal. This assumption is invariably made in modeling flows of nematic phases [31]. Consequently, the material physical constants, such as the elastic constants and viscosities, are constants.

(4) The simple shear flow and cone-and-plate configurations have been the only flow geometries (see Figure 3.2) used to study experimentally the banded texture formed after cessation of shear flow. It is then useful to assume that the plates are infinitely wide; hence,  $\frac{\partial(*)}{\partial y} = \frac{\partial(*)}{\partial x} = 0$ , where  $(*)$  denotes a dependent variable. In addition, since there is no variation of the banded texture in the sample thickness direction [42,54,56], it is assumed that  $\frac{\partial(*)}{\partial z} = 0$ . For simplicity, in the ensuing analyses, the simple shear flow configuration is used.

(5) There are no external body forces, such as the gravitational field. Hence,  $\mathbf{F} = 0$ .

(6) The nematic polymer phase is incompressible [31]; i.e.,  $\rho$  is a constant.

(7) The director remains within the sample  $(x,y)$  plane. This is a good assumption, because it is the planar director orientation that is used to determine the light intensity pattern.

(8) The director reorientation-induced backflow is a creeping flow; i.e., the viscous forces predominate over inertial forces. Therefore,  $\rho \dot{\mathbf{V}} = 0$ .

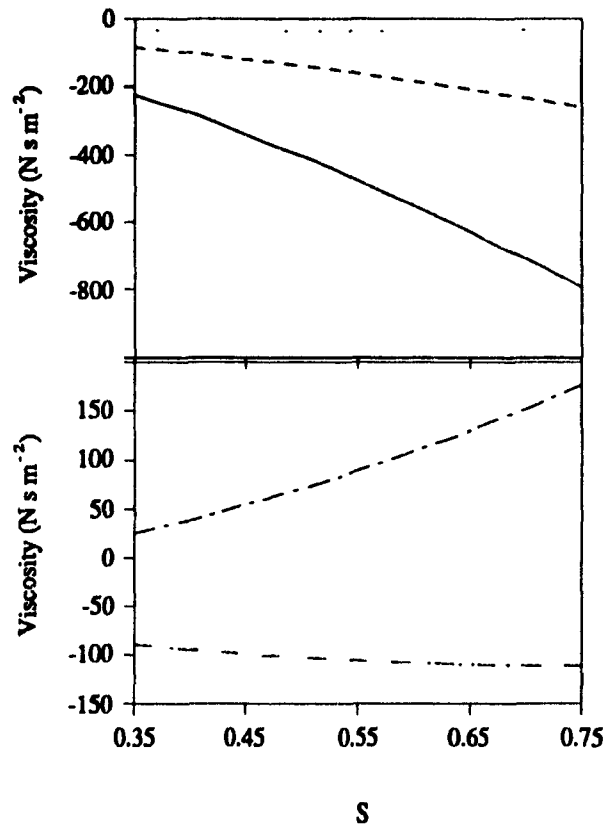


Figure 3.1. The dependence of the viscosities  $\alpha_1^S$  (—),  $\alpha_2^S$  (-----),  $\alpha_3^S$  (.....),  $\alpha_4^S + \alpha_5^S$  (-.-.-.-) and  $\alpha_4^S + \alpha_6^S$  (-...-...-...) on  $S$  for the nematic polymer DDA9.

(9) There are no flows along the  $x$ - and  $z$ -axes, i.e.,  $V_x = 0$  and  $V_z = 0$ . Since the backflow is director reorientation-induced, pressure does not affect the linear momentum balance.

(10) The inertia of the director is small [66] and neglected.

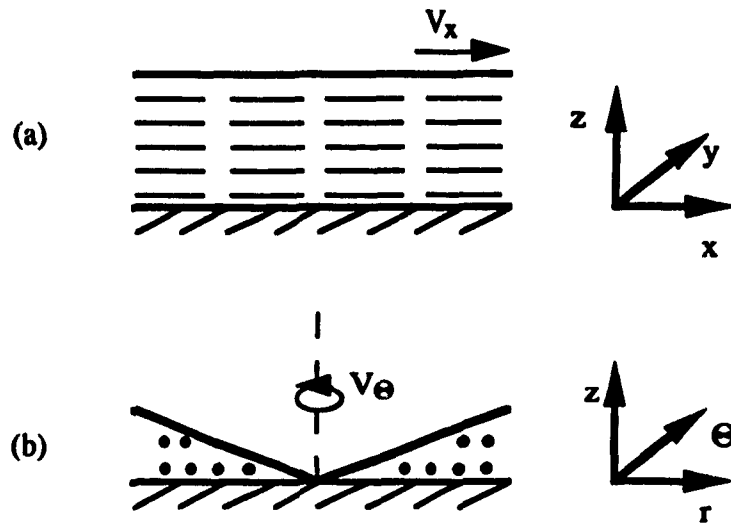


Figure 3.2. Schematic representations of the (a) simple shear flow, and (b) cone-and-plate configurations.

The simple shear flow configuration is shown schematically in Figure 3.3. The phenomena are best described in Cartesian coordinates; therefore the director field is defined as

$$\mathbf{n} = (\cos \phi, \sin \phi, 0) \quad (3.1)$$

where the unit length constraint,  $\mathbf{n} \cdot \mathbf{n} = 1$ , is automatically satisfied. The velocity field during the relaxation process then simplifies to

$$\mathbf{V} = (0, V_y, 0) \quad (3.2)$$

and the three dependent variables are:

$$S = S(x, t) \quad (3.3a)$$

$$\phi = \phi(x, t) \quad (3.3b)$$

$$V_y = V_y(x, t) \quad (3.3c)$$

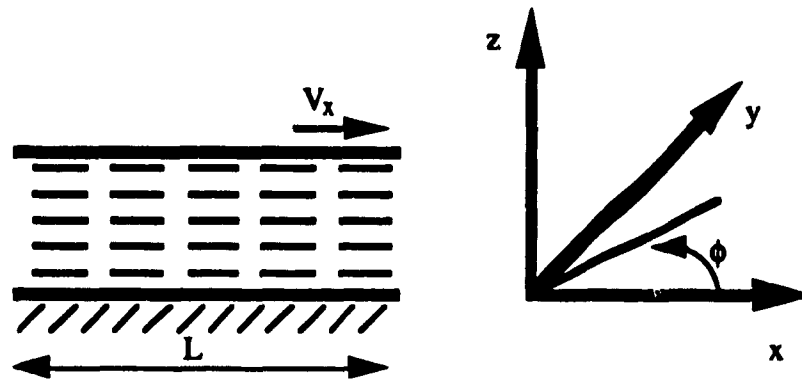


Figure 3.3. Schematic representation of the simple shear flow configuration, and definition of the Cartesian coordinate system.

Since there are three unknowns, three equations are needed. They are the  $y$ -component of the linear momentum balance equation, the  $z$ -component of the internal angular momentum balance equation, and the scalar order parameter balance equation. The symbolic algebra program Theorist [67] is used to help derive these equations. The coefficients  $A$ ,  $B$  and  $C$  in the Landau-de Gennes free energy density (equation (1.25)) are not known for a nematic polymer. It is then convenient to replace the spatially invariant terms in this free energy by an expression given by Doi and Edwards [32], which is as follows:

$$F_S = k_B \vartheta T \left[ \frac{1}{2} \left( 1 - \frac{1}{3} U \right) S^2 - \frac{1}{9} U S^3 + \frac{1}{6} U S^4 \right] \quad (3.4)$$

$k_B$  is the Boltzmann constant,  $\vartheta$  is the rod concentration,  $T$  is the temperature, and  $U$  is the dimensionless nematic potential. The shape of this curve is shown schematically in Figure 3.4 for a typical nematic polymer phase. Now, only  $U$  is unknown, but typical values are known.

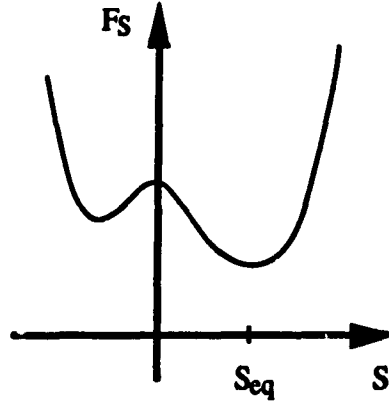


Figure 3.4. Typical dependence of the free energy  $F_S$  on the scalar order parameter  $S$ .  $S_{eq}$  is the equilibrium value of  $S$ .

To derive the  $y$ -component of the linear momentum balance equation, assumptions #1 to 9 given above, equations (1.18), (1.20), (1.23), (1.25), (1.28), and (3.1) to (3.4) are used. The final result of this derivation is

$$0 = \eta_{31} \frac{\partial}{\partial x} \frac{\partial \phi}{\partial t} + \eta_{32} \frac{\partial \phi}{\partial x} \frac{\partial \phi}{\partial t} + \eta_{33} \frac{\partial \phi}{\partial x} \frac{\partial V_y}{\partial x} + \eta_{34} \frac{\partial}{\partial x} \frac{\partial V_y}{\partial x} \quad (3.5)$$

where the angle-dependent viscosity functions  $\{\eta_i\}$ ,  $i = 31, \dots, 34$ , are given in Appendix B. Assumptions #1 to 4, 7, 9 and 10, equations (1.20), (1.23), (1.25) to (1.27) and (3.1) to (3.4) are used to obtain the  $z$ -component of the internal angular momentum balance equation and the scalar order parameter balance equation. They are, respectively, as follow:

$$\eta_{35} \frac{\partial \phi}{\partial t} = \kappa_{36} \frac{\partial S}{\partial x} \frac{\partial \phi}{\partial x} + \kappa_{37} \frac{\partial}{\partial x} \frac{\partial \phi}{\partial x} + \kappa_{38} \frac{\partial}{\partial x} \frac{\partial S}{\partial x} + \eta_{36} \frac{\partial V_y}{\partial x} \quad (3.6)$$

$$\begin{aligned} \eta_{37} \frac{\partial S}{\partial t} = & k_B \theta T \left[ \left(1 - \frac{1}{3} U\right) S - \frac{1}{3} U S^2 + \frac{2}{3} U S^3 \right] + \kappa_{39} \left(\frac{\partial \phi}{\partial x}\right)^2 + \kappa_{40} \frac{\partial}{\partial x} \frac{\partial S}{\partial x} + \\ & \kappa_{41} \frac{\partial \phi}{\partial x} \frac{\partial S}{\partial x} + \kappa_{42} \frac{\partial}{\partial x} \frac{\partial S}{\partial x} + \kappa_{43} \left(\frac{\partial \phi}{\partial x}\right)^2 + \kappa_{44} \frac{\partial}{\partial x} \frac{\partial \phi}{\partial x} + \eta_{38} \frac{\partial V_y}{\partial x} \end{aligned} \quad (3.7)$$

where the angle-dependent elastic functions  $\{\kappa_i\}$ ,  $i = 36, \dots, 44$ , and viscosity functions  $\{\eta_i\}$ ,  $i = 35, \dots, 38$  are also given in Appendix B.

The material physical constants used in this study are for the polymer DDA9 [73], and are tabulated in Table 3.1. The values for  $\beta_1$ ,  $\beta_2$ ,  $K$ ,  $K_5$  and  $K_6$  are assumed, because no experimentally determined values can be found for them. The magnitudes of the three elastic constants are around the estimated value of  $10^{-12}$  N [12]. Furthermore, the three elastic constants fulfill the constitutive hypothesis set up by Maddocks [74]. He studied static disclinations in nematic phases using a much simpler free energy density than the Landau-de Gennes one, and hypothesized the following inequality:

$$K_5 + K_6 > K \quad (3.8)$$

The values for  $\beta_1$  and  $\beta_2$  are chosen as such so the following predicted ratios are satisfied [32,36,38]:

$$\frac{|\beta_1|}{\gamma_1} \approx 10 ; \frac{\beta_2}{\gamma_1} \approx 1 ; \frac{|\beta_1|}{\beta_2} \approx 2 \quad (3.9a,b,c)$$

Table 3.1  
Physical Constants for DDA9 [73]

Viscosities, N s m <sup>-2</sup>	
$\alpha_1$	- 393
$\alpha_2$	- 415
$\alpha_3$	- 4
$\alpha_4 + \alpha_5$	429
$\alpha_4 + \alpha_6$	10
$\beta_1^{\#}$	- $411 \times 10^2$
$\beta_2^{\#}$	$205.5 \times 10^2$
Elastic Constants, $\times 10^{-11}$ N	
$K^{\#} = 9L_1 + \frac{9}{2}L_2$	3.78
$K_5^{\#} = \frac{3}{2}L_1 + \frac{1}{4}L_2$	3.78
$K_6^{\#} = \frac{3}{4}L_2$	37.8

# These values are assumed, since no experimentally determined values are reported.

The initial and periodic boundary conditions are as follow:

$$\phi = A_\phi \sin(k_\phi \pi x + \frac{1}{2} \pi) \text{ at } t = 0, 0 \leq x \leq L \quad (3.10a)$$

$$S = S_0 + A_S \sin(k_S \pi x + \frac{1}{2} \pi) \text{ at } t = 0, 0 \leq x \leq L \quad (3.10b)$$

$$V_y = 0 \text{ at } t = 0, 0 \leq x \leq L \quad (3.10c)$$

$$\frac{\partial \phi}{\partial x} = 0 \text{ at } t > 0, x = 0 \quad (3.10d)$$

$$\frac{\partial \phi}{\partial x} = 0 \text{ at } t > 0, x = L \quad (3.10e)$$

$$\frac{\partial S}{\partial x} = 0 \text{ at } t > 0, x = 0 \quad (3.10f)$$

$$\frac{\partial S}{\partial x} = 0 \text{ at } t > 0, x = L \quad (3.10g)$$

$$V_y = 0 \text{ at } t > 0, x = 0 \quad (3.10h)$$

$$V_y = 0 \text{ at } t > 0, x = L \quad (3.10i)$$

where  $A_\phi$  and  $A_S$  are the wave amplitudes, and  $k_\phi$  and  $k_S$  are the wave length scales.  $S_0$  is the base value for the wave.

Equations (3.5) to (3.7) and (3.10) are solved numerically in dimensionless form using the material physical constants for DDA9. The scaling variables, dimensionless governing equations, and dimensionless initial and periodic boundary conditions are given in Appendix B. The Galerkin finite element method is used with 252 linear elements [68]. The time integrator is the first-order Euler predictor-corrector method [69], and the Newton-Raphson method is used for solving this system of nonlinear partial differential equations. For all calculations, the length  $L$  is chosen as  $157.5 \times 10^{-6}$  m. For a typical nematic polymer,  $U = 5.769$ ; the equilibrium  $S$  value is then  $S_{eq} = 0.8$  [32]. In addition, for a typical nematic polymer, the molecular length is  $1.5 \times 10^{-7}$  m and the molecular diameter is  $1.5 \times 10^{-9}$  m [75,76]. Hence, the concentration, using the relation [32]

$$\vartheta = \frac{4.44}{3} \frac{U}{(\text{molecular length})^2 \times \text{molecular diameter}} \quad (3.11)$$

is  $2.53 \times 10^{23}$  rods  $\text{m}^{-3}$ . At room temperature ( $T = 298$  K), the product  $k_B \vartheta T = 1.04 \times 10^3$  J  $\text{m}^{-3}$ . The code is written in FORTRAN, and executed on the IBM 3090 S130 mainframe at McGill University. A copy of the code is available, upon request, from Prof. A. D. Rey.

### 3.3 Results and Discussion

This section is divided into two parts. The first part presents typical relaxation phenomena and pattern formation after cessation of shear flow. The second part presents the effects of the base value  $S_0$  and amplitude  $A_S$  of the initial  $S$  periodic spatial variation on the relaxation phenomena and pattern formation after cessation of shear flow. As mentioned in Section 3.1, the emphasis in this chapter is on the time for periodic pattern formation ( $t_p$ ) and the maximum planar director orientation ( $\phi_m$ ) of the resulting pattern.

#### 3.3.1 Typical Results on the Relaxation Phenomena and Pattern Formation

The initial condition used in this section is as follows: equation (3.10a) with  $A_\phi = 0.01$  rad and  $k_\phi = \frac{21}{L}$   $\text{m}^{-1}$ , equation (3.10b) with  $S_0 = 0.75$ ,  $A_S = 0.108$  and  $k_S = \frac{126}{L}$   $\text{m}^{-1}$ , and equation (3.10c). The length scale  $k_\phi$  is chosen such that the periodic director field wavelength is  $1.5 \times 10^{-5}$  m. This is a typical wavelength, as measured experimentally, for the director field in the banded texture [42,44,47,51,53,55-57]. Furthermore, it is shown below that this wavelength is the fastest growing one when compared to longer and shorter wavelengths according to the principle that the fastest growing wavelength optimizes the effects due to elasticity and backflow [13,17]. The length scale  $k_S$  is chosen to represent a possible spatial variation in  $S$ . This is certainly not the only possible value; however, there are no known experimentally determined results on the spatial effects that shear flow has on  $S$ . The value  $A_S = 0.108$  is not rather large and unrealistic if one considers the large temporal periodic oscillations of  $S$  in certain shear rate ranges of nematic polymer flows [35,36]. For instance, Larson [35] predicted, for one shearing condition, that this temporal oscillation of  $S$  ranges from  $S = 0.2$  to  $S = 0.8$ . This gives an amplitude of 0.6. Furthermore, the idea that these temporal oscillations indeed represent spatial variations in  $S$  have already been cited by Marrucci [30] and Larson [35].

From the above initial conditions, it is noticed that the shear flow has an aligning effect on the director field; i.e.,  $\phi \equiv 0$  rad for  $0 \leq x \leq L$ . Conversely, the shear flow does not smooth the spatial variations in  $S$ . This is due to the dependency of the viscosity  $\beta_1$  on  $S$  during shear flow (see Figure 3.5). As shown schematically in Figure 3.5, the magnitude of  $\beta_1$  increases with  $S$  [36]. In addition, the scalar order parameter during shear flow  $S_f$  is below the equilibrium value  $S_{eq}$  [35,36]. During shear flow, as stated above, there are  $S$  spatial variations. When  $0 < S < S_f$ , the elastic force driving  $S$  back to equilibrium increases, but the flow force driving  $S$  to lower values decreases. By a balance of net forces, it would then be consistent for  $S$  to return quickly back to equilibrium. However, since the magnitude of  $\beta_1$  has decreased (since  $S$  is lower here), the weaker flow force faces a lower viscosity; this increases the effectiveness of the flow force. The net force could then be zero, and  $S$  remains at this value for a while longer. Similar arguments are made when  $S_f < S < S_{eq}$ .

Figure 3.6 shows typical relaxation phenomena for  $S$  (first row),  $\phi$  (second row) and  $V_y^*$  (third row) along  $x^*$  after cessation of shear flow at  $t = 0.0$  s (first column),  $t = 4.0$  s (second column),  $t = 14.3$  s (third column), and  $t = 31.7$  s (fourth column). The initial state contains minor director gradients, but considerable  $S$  gradients. These gradients raise the elastic free energy of the system as shown at  $t = 0.0$  s in Figure 3.7. Since the shear flow has stopped, the effect of the dependency of  $\beta_1$  on  $S$ , as described above, is no longer present. Consequently, the  $S$  spatial variations relax after cessation of shear flow. This produces spatially periodic torques on the director ( $t = 4.0$  s and  $14.3$  s) to rotate away from the prior flow direction. As shown in Figure 3.7, this is the fastest route for the system to release its stored elastic free energy, even though the director distortions are growing ( $t = 4.0$  s and  $t = 14.3$  s). This is primarily due to the couplings between  $\mathbf{n}$  and  $\nabla S$  introduced by the  $L_2$  (or, equivalently,  $K_6$ ) constant in the Landau-de Gennes free energy expression (equation (1.25)). The dot product  $\mathbf{n} \cdot \nabla S$  goes to zero when  $\mathbf{n}$  and  $\nabla S$  are normal to each other. Since  $\nabla S$  is along the prior flow direction,  $\nabla S \neq 0$  and only planar director orientation is considered, the magnitude of  $\phi$  then grows. As the  $S$  spatial variations continue to decay, so do the driving torques and the director begins to reorient towards its initial state ( $t = 31.7$  s). Figure 3.7 also shows that the periodic director pattern is unstable. At  $t \geq 31.7$  s,  $\nabla S \equiv 0$ ; therefore,  $F_L$  reduces to the spatially invariant terms ( $F_S$ ) and the equivalents of the director splay and bend distortion terms in the Frank-Oseen-Zocher elastic free energy density (equation (1.6)). The present fastest route that minimizes the stored elastic free energy is that where the directors reorient to a uniform orientation. This part of the relaxation phenomenon (i.e., relaxation

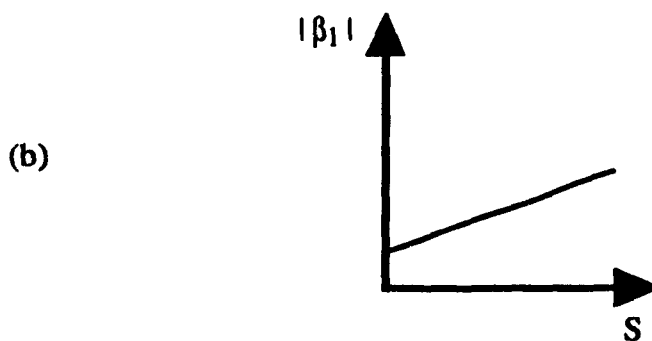
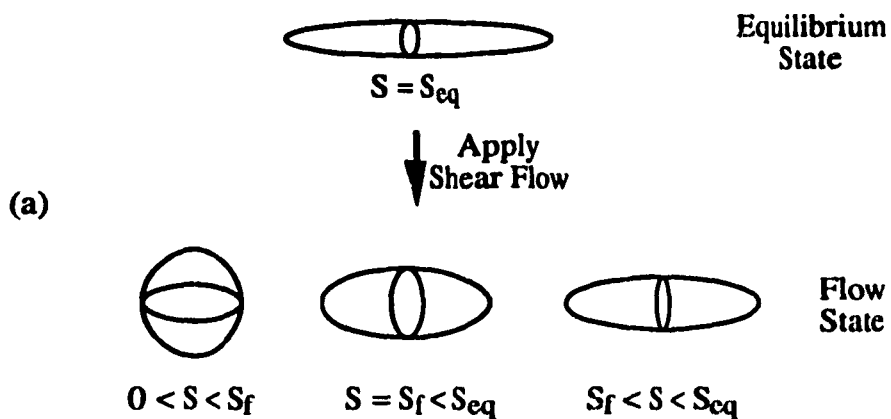


Figure 3.5. Schematic representations of (a) the effect shear flow has on the scalar order parameter  $S$ , and (b) the dependence of the magnitude of the viscosity  $\beta_1$  on  $S$ .  $S_{eq}$  and  $S_f$  are the equilibrium and flow values of  $S$ , respectively.

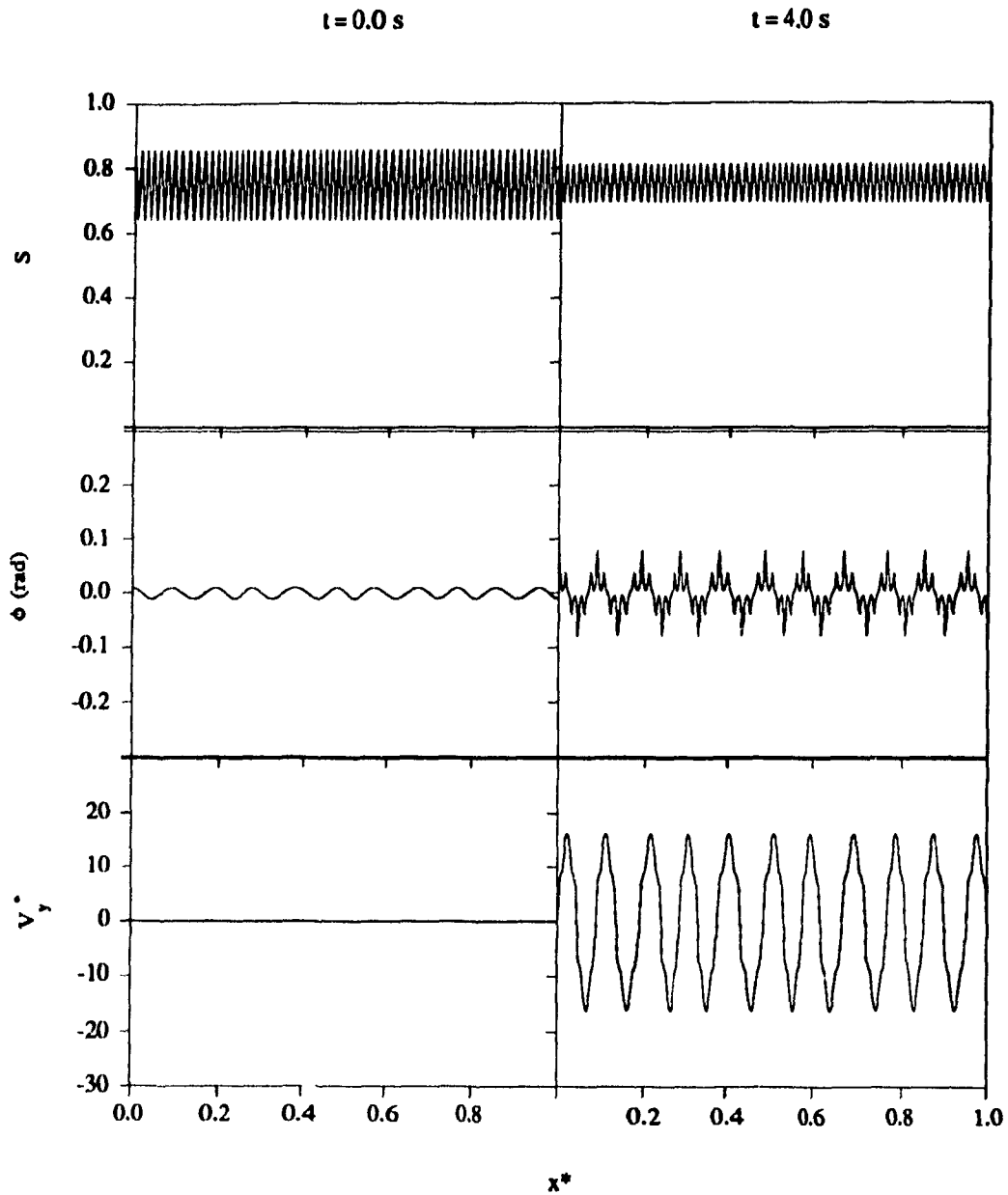


Figure 3.6 (continued on next page). Scalar order parameter  $S$  (first row), planar orientation angle  $\phi$  (second row) and dimensionless velocity  $V_y^*$  (third row) spatial profiles at  $t = 0.0$  s (first column),  $t = 4.0$  s (second column),  $t = 14.3$  s (third column) and  $t = 31.7$  s (fourth column).

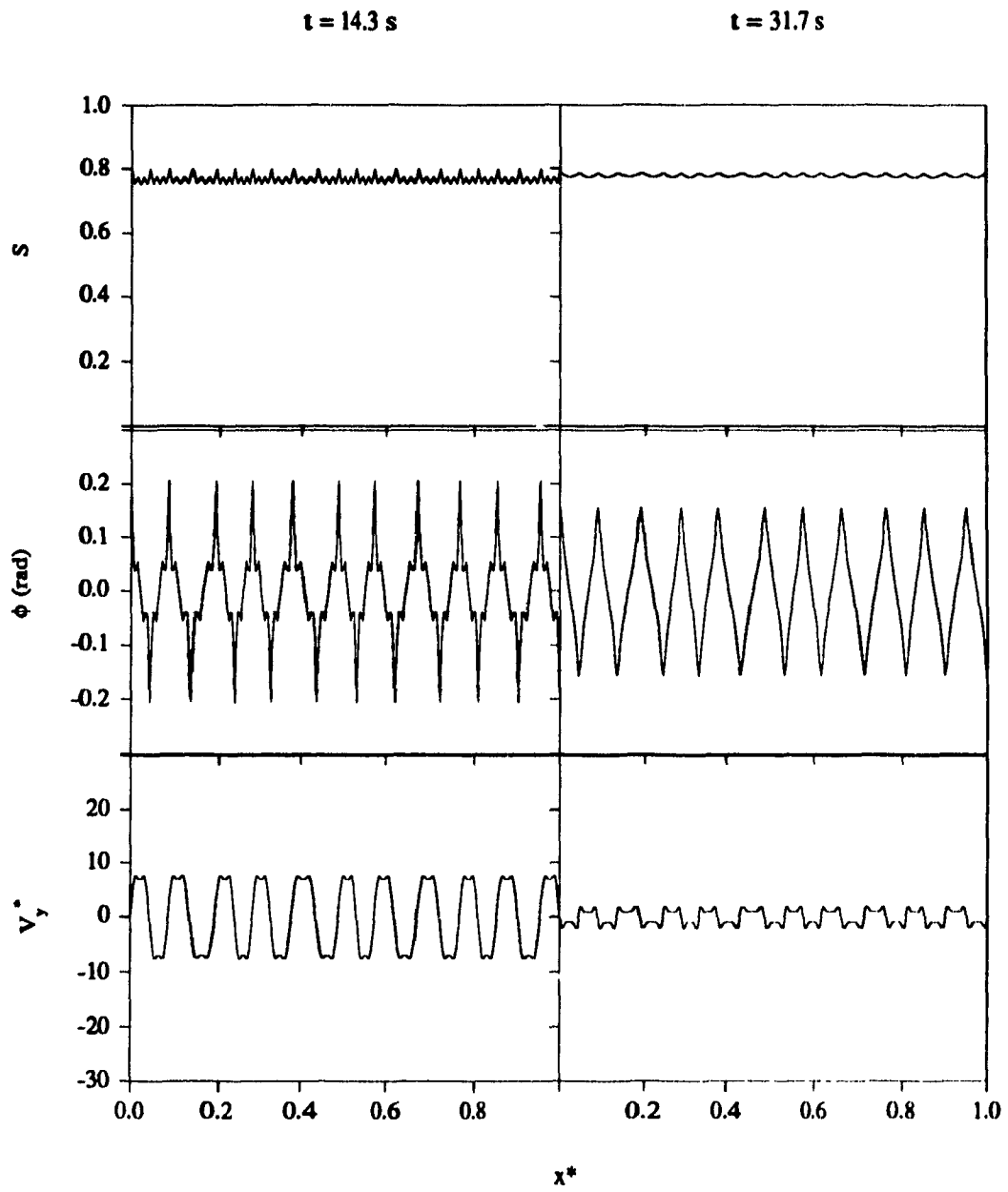


Figure 3.6 (continued).

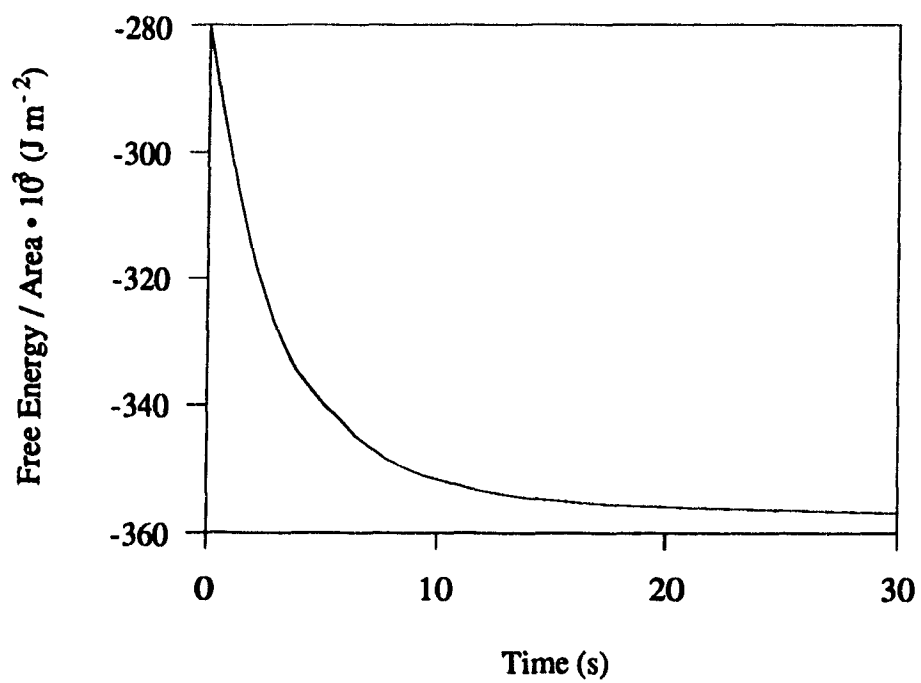


Figure 3.7. Transient relaxation of the stored free energy per unit area.

of director distortions) has already been discussed in Chapter 2, where  $S(x,t) = 1.0$  is assumed.

The response is viscoelastic since periodic director reorientation creates periodic backflows, as shown in the third row of Figure 3.6. This is due to the intimate coupling between flow and orientation [26-29]. The phase difference of  $\frac{1}{2} \pi$  rad between the  $\phi$  and  $V_y^*$  spatial profiles is physically consistent. Maximum director rotation couples with minimum flow, and minimum director rotation couples with maximum flow. This kind of periodic coupling is seen in the magnetic reorientation of nematic polymers [13,17]. Unlike the magnetic reorientation phenomenon, however, the sign ( $\pm$ ) of  $V_y^*$  at  $t = 14.3$  s and any position  $x^*$  switches to the opposite sign at  $t = 31.7$  s; i.e., at any  $x^*$ ,  $V_y^*$  becomes ( $-V_y^*$ ). This is due to the reversal of director rotation; at  $t = 14.3$  s the directors are rotating away from  $x^*$ , but at  $t = 31.7$  s the directors are rotating back to  $x^*$ . The coupling between reorientation and flow is evident in this model through:

- (1) the  $\eta_{31}$ ,  $\eta_{32}$ , and  $\eta_{33}$  terms in equation (3.5), and
- (2) the  $\eta_{36}$  term in equation (3.6).

Equation (1.33) is used to calculate the relative intensity patterns, as seen between crossed polars, for the director fields shown in the second row of Figure 3.6. By assuming a constant phase lag  $\delta_L$  [77] and taking  $\phi$  to be  $\zeta$  [63,78], the relative intensity is

$$I_r = \sin^2(2\phi) \quad (3.12)$$

Figure 3.8 shows the digitized optical light patterns of the corresponding director fields in Figure 3.6. A strong resemblance between the patterns at  $t = 14.3$  and  $31.7$  s and the banded textures shown in Figures 1.16 and 1.18 is noted. At  $t = 0.0$  s, the optical pattern is all black. This implies that the directors, as specified by the initial condition, are highly aligned along the prior shear flow direction [56]. At early times ( $t = 4.0$  s), a banded texture of weak contrast begins to appear. As time progresses ( $t = 14.3$  s), the directors rotate away from the prior flow direction, and the banded texture develops into a well defined periodic pattern with good contrast. It then remains for some time ( $t = 31.7$  s). The development of these optical patterns are consistent with the experimental observations of the development of the banded texture formed after cessation of shear flow made by Kiss and Porter [44] and Marsano *et al.* [56]. This model, with the given physical material constants and initial and boundary conditions, demonstrates that the relaxation of stored elastic energy due to periodic  $S$  spatial variations results in a transient

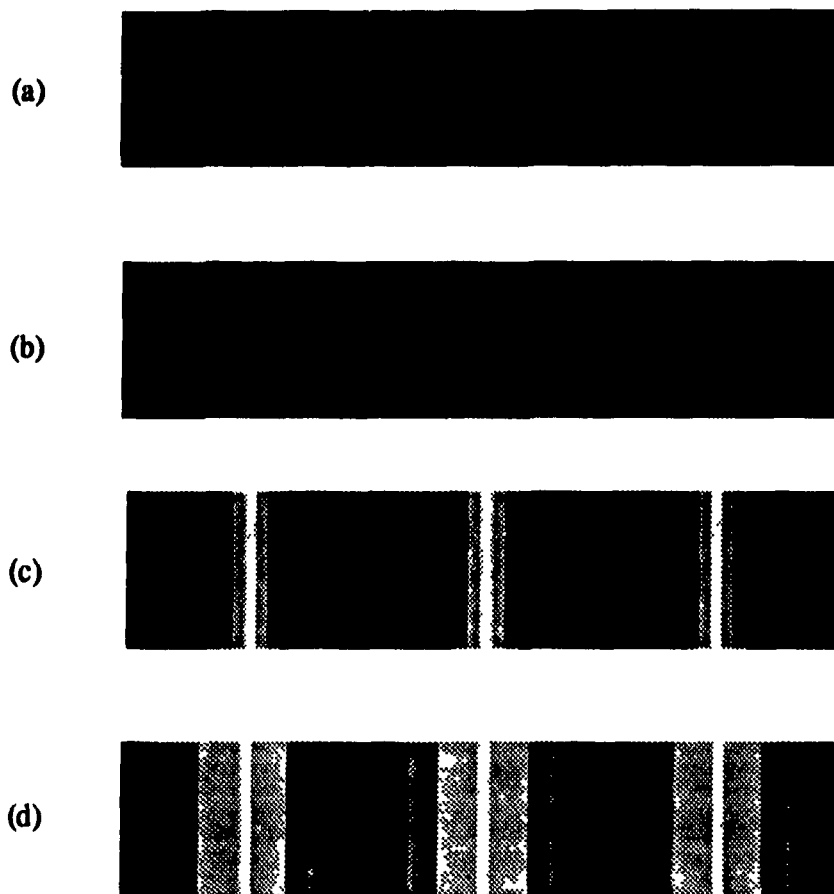


**Figure 3.8.** Time evolution of the digitized optical light patterns representing the patterns seen between crossed polars for the director fields in Figure 3.6. The times are: (a)  $t = 0.0$  s, (b)  $t = 4.0$  s, (c)  $t = 14.3$  s and (d)  $t = 31.7$  s. The relative maximum intensity is white and the relative minimum is black.

periodic distortion of the director field, such that a transient banded texture is seen when the sample is viewed between crossed polars.

In a periodic director reorientation response, backflows are created. As explained in Chapter 2, backflows relax the constraint of director rotation; the rotational viscosity is replaced by a lower effective one. The response speed is now increased; therefore, viscous flow favors short wavelengths. However, short wavelengths contain large director distortions which increase the elastic free energy. The elastic forces then tend to favor long wavelengths. Hence, the macroscopically observable wavelength optimizes the effects due to the viscous and elastic forces [13,17], and is the fastest growing one [79]. Since the initial condition for the director field contains a slight periodic modulation, it is necessary to use this optimization theory to show that the wavelength used in the above calculations was not arbitrarily chosen but, rather, is the fastest growing one when compared to shorter and longer wavelengths.

Figure 3.9 shows  $\phi_m$  (first row),  $V_{y,m}^*$  (second row) and the free energy per unit area (third row) as a function of time at the early (first column) and later (second column) stages of the banded texture formation. The parameter is the director field wavelength  $\lambda_b$ . From the first row, it is noticed that the banded texture with  $\lambda_b = 1.5 \times 10^{-5}$  m is the fastest growing one when compared to a longer and shorter one. Consequently, it is the macroscopically observable one [79]. There is a cross over of the  $\phi_m$  curves for  $\lambda_b = 1.5 \times 10^{-5}$  m and  $\lambda_b = 6.3 \times 10^{-5}$  m at  $t \cong 50$  s. Since there are less elastic distortions in the latter wavelength than in the former, it will take longer for  $\phi_m$  in the longer wavelength to relax to equilibrium. The free energy (third row) decays similarly for the three  $\lambda_b$ 's. This is attributed to the fact that the spatially invariant terms (equation (3.4)) in the free energy are much greater than the other terms, and that  $S_0$  relaxes to equilibrium independently of the other variables.

Thus far, many similarities between the developments of a transient banded texture after cessation of shear flow and that due to a magnetic field [13,17,79] have been cited. There are, however, differences. In the magnetic field case, the initial optimal wavelength corresponds to the fastest growth rate of  $V_{y,m}^*$  [13,17]. Conversely, this is not true for the optimal wavelength in this study (Figure 3.9, second row). This difference can be accounted for by examining the director fields formed during the relaxation phenomena. Figure 3.10 shows the relaxation phenomena of  $\phi$  along  $x^*$  after cessation of shear flow for  $\lambda_b = 5.0 \times 10^{-6}$  m (first row),  $\lambda_b = 1.5 \times 10^{-5}$  m (second row) and  $\lambda_b = 6.3 \times 10^{-5}$  m (third row) at  $t = 0.0$  s (first column) and  $t = 14.3$  s (second column). Although the initial periodic modulations (first column) for the three  $\lambda_b$ 's are quite similar, the resulting director fields at  $t = 14.3$  s are not. In addition, the director

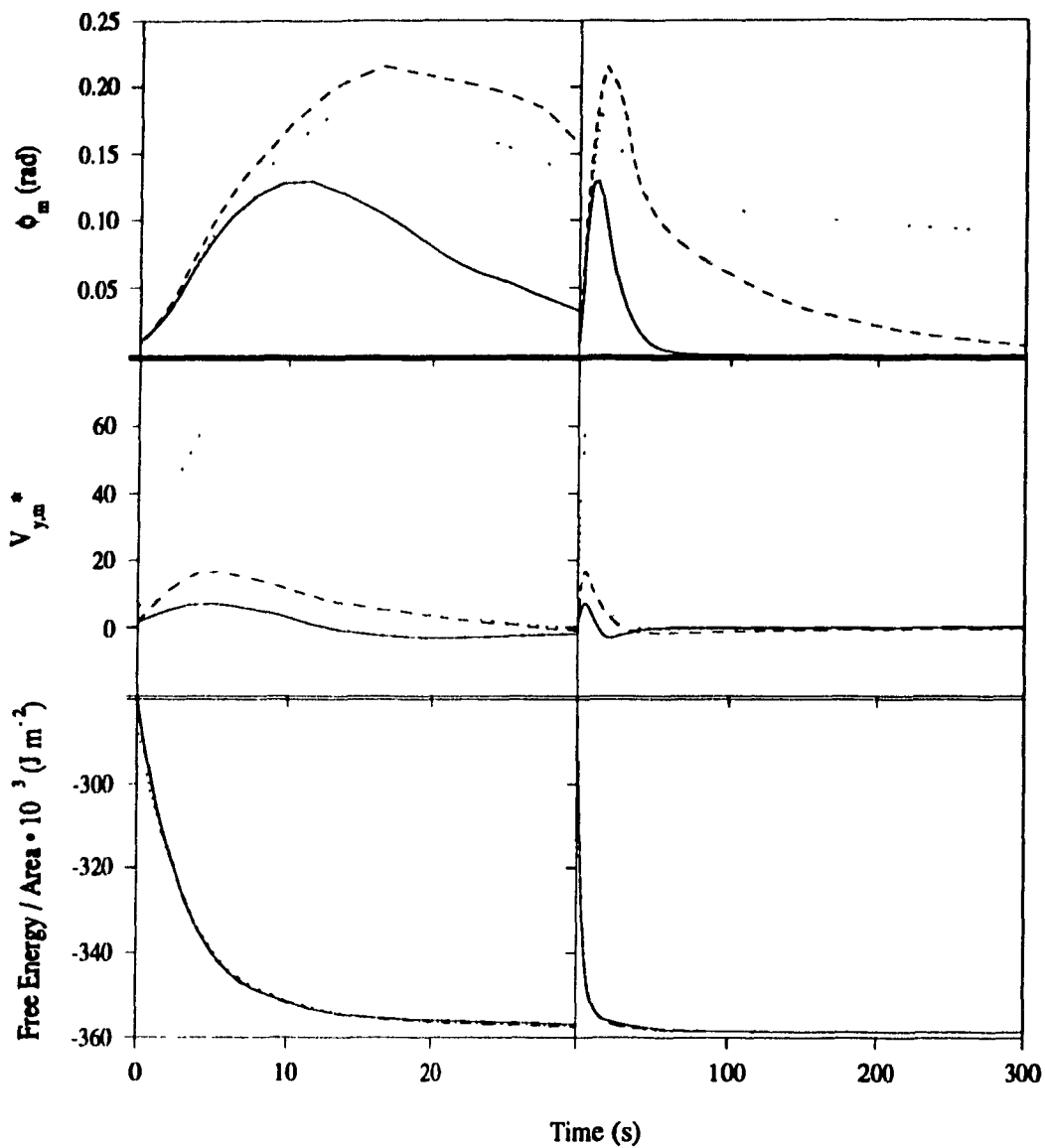


Figure 3.9. Maximum planar orientation angle  $\phi_m$  (first row), maximum dimensionless velocity  $V_{y,m}^*$  (second row) and free energy per unit area as a function of time at early (first column) and later (second column) times. The periodic director field wavelengths are:  $\lambda_b = 5.0 \times 10^{-6}$  m (—),  $\lambda_b = 1.5 \times 10^{-5}$  m (-----) and  $\lambda_b = 6.3 \times 10^{-5}$  m (·····).

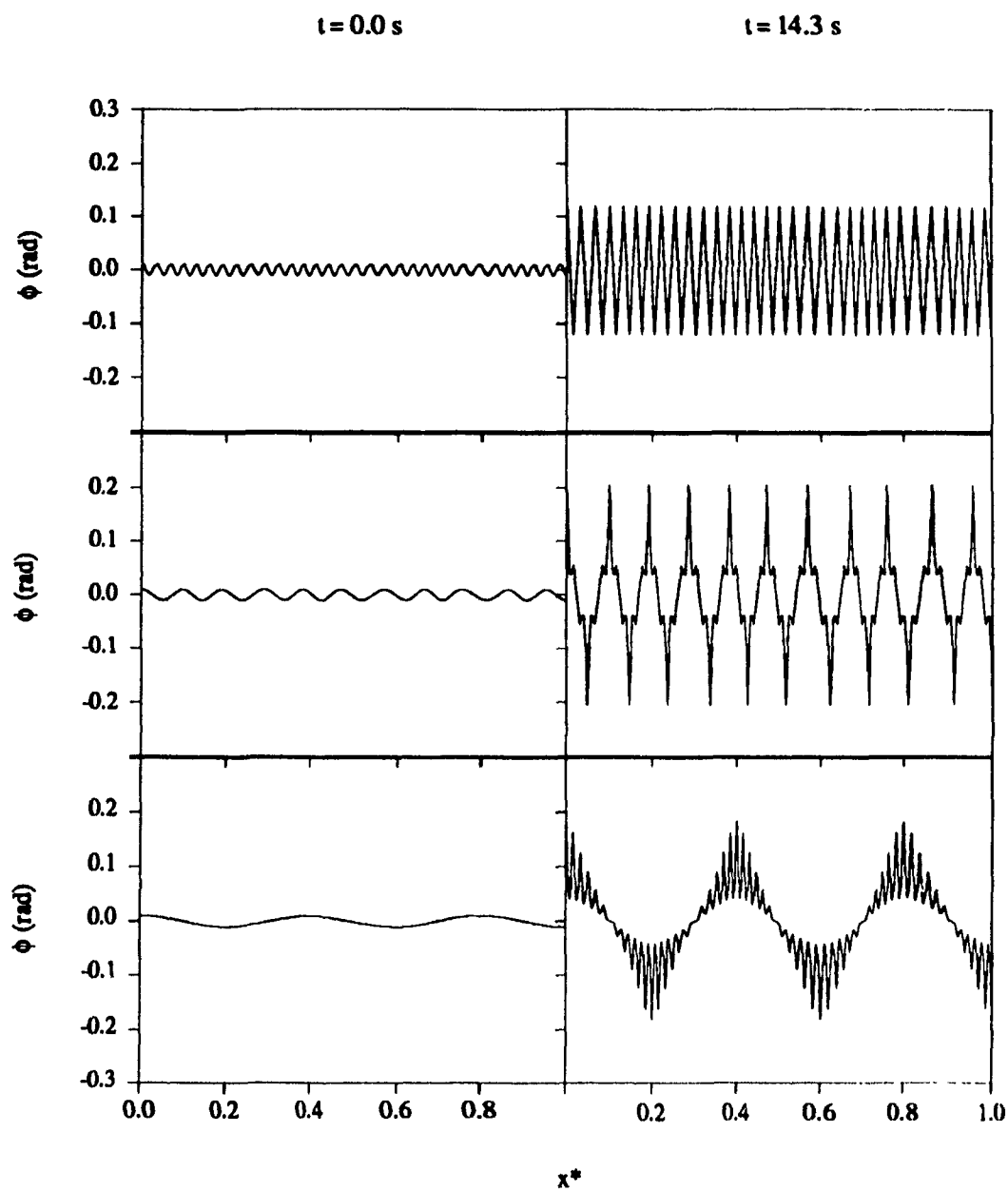


Figure 3.10. Spatial planar orientation angle  $\phi$  profiles at  $t = 0.0 \text{ s}$  (first column) and  $t = 14.3 \text{ s}$  (second column). The periodic director field wavelengths are:  $\lambda_b = 5.0 \times 10^{-6} \text{ m}$  (first row),  $\lambda_b = 1.5 \times 10^{-5} \text{ m}$  (second row) and  $\lambda_b = 6.3 \times 10^{-5} \text{ m}$  (third row).

fields at  $t = 14.3$  s do not resemble the smooth sinusoidal director fields predicted for the magnetic reorientation phenomenon [13,17]. Further insights are obtained by studying the power spectrums of the director fields  $|\phi|^2$  as shown in Figure 3.11.

Fourier transform, or power spectrum, is a common method of analyzing a set of numerical data points [80]. The goal is then to determine the periodic components of the set of data points with particular wavelengths. For example, Srajer *et al.* [13] used transient power spectrums of  $\phi$  to show that the wavelength of the transient periodic director configuration due to a magnetic field switches from a short wavelength to a longer one as the magnitude of  $\phi$  grows. The power spectrums in Figure 3.11 are for  $\lambda_b = 5.0 \times 10^{-6}$  m (top graph),  $\lambda_b = 1.5 \times 10^{-5}$  m (middle graph) and  $\lambda_b = 6.3 \times 10^{-5}$  m (bottom graph). They are obtained by squaring the moduli of the Fourier transforms [80,81] of the corresponding director fields at  $t = 14.3$  s in Figure 3.10. The fast Fourier transform operation in MATLAB [82] is used for this purpose. MATLAB [82] is a high-performance interactive software package for scientific and engineering numeric computation. Figure 3.11 shows that the director relaxation phenomenon is very different for each  $\lambda_b$ . There are only two modes at the shortest  $\lambda_b$ , four modes at the longest  $\lambda_b$ , but six modes at the intermediate  $\lambda_b$ . As mentioned previously, periodic director rotations create periodic backflows, which tend to increase the rate of director reorientation by reducing the magnitude of the rotational viscosity. Consequently, since the intermediate wavelength has the most modes of periodic director rotation, it is then expected that this  $\lambda_b$  be the optimal one. Since the longest  $\lambda_b$  has the second largest number of modes, it is then expected to be the second fastest growing wavelength. Lastly, since the shortest  $\lambda_b$  has only two modes, it is the slowest growing wavelength of the three. This is consistent with the results shown in the first row of Figure 3.9. The results for  $V_{y,m}^*$  shown in the second row of Figure 3.9 is then a manifestation of the intimate coupling between the multiple modes of periodic director rotation and flow.

### 3.3.2 Effects of the Base Value and Amplitude of the Initial Periodic Scalar Order

#### Parameter Spatial Variation on Pattern Formation

It has been established in Section 3.3.1 that the present model, along with the given physical material properties and initial and boundary conditions, predicts a periodic light intensity pattern that is believed to be ubiquitous banded texture nematic polymers exhibit after cessation of shear flow. This section examines the effects that the base value  $S_0$  and amplitude  $A_S$  of the initial periodic spatial variation in the scalar order parameter  $S$  have on the time for banded texture formation  $t_b$ , the resulting maximum orientation

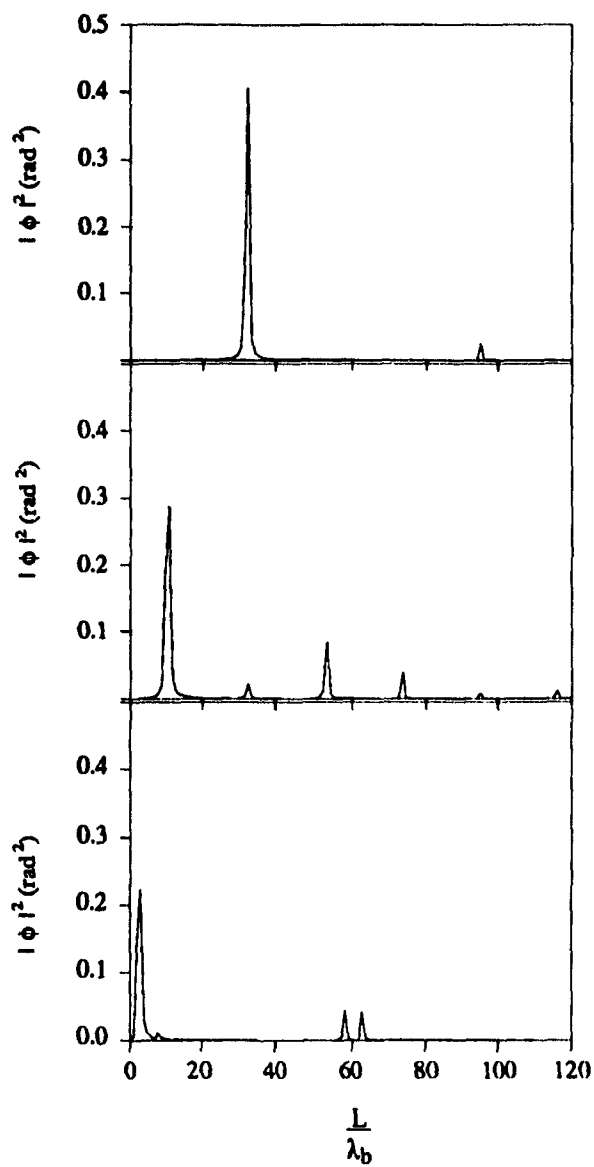


Figure 3.11. Power spectrums of the planar orientation angle at  $t = 14.3$  s for the following periodic director field wavelengths:  $\lambda_b = 5.0 \times 10^{-6}$  m (top graph),  $\lambda_b = 1.5 \times 10^{-5}$  m (middle graph) and  $\lambda_b = 6.3 \times 10^{-5}$  m (bottom graph).

angle in the banded texture  $\phi_m$ , and the time to reach this maximum angle  $t_{\phi_m}$  for the optimal wavelength determined above. Based on these results, several experimental observations reported in the literature on the banded texture are explained.

Figure 3.12 shows the dependence of  $t_b$  on  $S_0$  with  $A_S$  as the parameter. The region of interest for  $S_0$  is chosen as  $0.35 \leq S_0 \leq 0.75$ , because  $S_f < S_{eq}$  during shear flow [35,36]. The region of interest for  $A_S$  is chosen as  $0.080 \leq A_S \leq 0.108$ , because it represents a possible range for  $S$  spatial variations (see Section 3.3.1). A banded texture is deemed subjectively [56] to be present when  $I_r = 0.005$  (i.e.,  $\phi_m = 0.035$  rad). Figure 3.12 resembles very much like Figure 3.13, which shows the dependence of  $t_b$  on the shear rate  $\dot{\gamma}$  and with the shearing time  $t_s$  as the parameter [57]. It is known, from numerical predictions on monodomain and spatially invariant nematic polymer systems during shear flow, that  $S$  increases with  $\dot{\gamma}$  at sufficiently high shear rates [35,36] as shown schematically in Figure 3.14. This could then explain the fact that bands only appear when  $\dot{\gamma} \geq \dot{\gamma}_c$  [53,54,56-60]. In the decreasing region of Figure 3.14, the directors during shear flow are predicted to be oscillating between two orientations. Conversely, the directors are highly aligned in the flow direction in the increasing region, which is the prerequisite for banded texture formation after cessation of shear flow [44,54,56,57]. For instance, Farhodi [36] predicted for one set of conditions that the tilt angle (see Figure 2.1) is  $\theta \equiv 1.763$  rad. In addition, by making the plausible hypothesis that  $A_S$  increases with  $t_s$  during shear flow, several experimental observations can be explained. For instance, this model predicts that a minimum  $A_S$  is needed for banded texture formation. By this hypothesis, the minimum  $A_S$  is then related to the critical shearing time  $t_{sc}$  needed for banded texture formation [53,54,56-60]. Figure 3.12 can then be used to explain the experimental findings contained in Figure 3.13. Figure 3.12 demonstrates that, at a given  $A_S$ ,  $t_b$  decreases as  $S_0$  increases. The reason for this behavior is that any increase in  $S_0$  at  $t = 0$  s increases the initial stored free energy primarily through the second and third  $L_2$  terms in equation (1.25). Furthermore, this stored energy makes the system unstable after cessation of shear flow, and must be dissipated as fast as possible through director rotation and viscous backflow. Consequently, a system with a higher energy level will dissipate its stored energy faster than a system with a lower energy level; therefore, the banded texture appears faster. This figure also shows that, at a given  $S_0$ ,  $t_b$  decreases as  $A_S$  increases. This is due to the fact that the stored free energy, through the three  $L_2$  terms in equation (1.25), increases during flow as  $A_S$  increases. As explained above, the banded texture appears faster for a system with a higher energy level than one with a lower energy level.

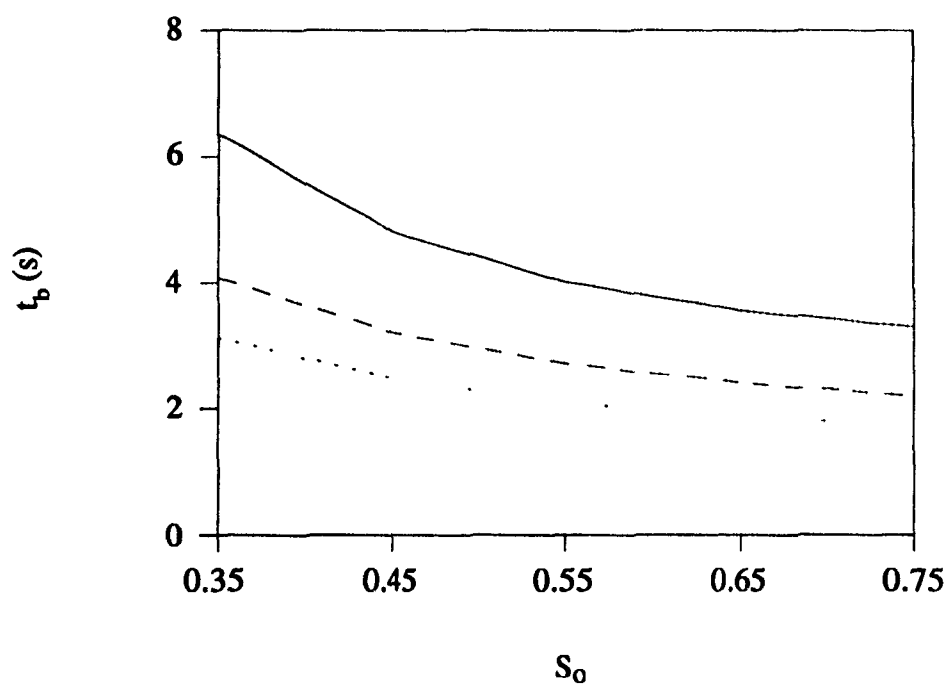


Figure 3.12. Time for banded texture formation  $t_b$  as a function of the base value of the initial periodic scalar order parameter spatial variation  $S_0$ . The amplitudes of the periodic variation are:  $A_S = 0.080$  (—),  $A_S = 0.095$  (- - - -) and  $A_S = 0.108$  (· · · ·).

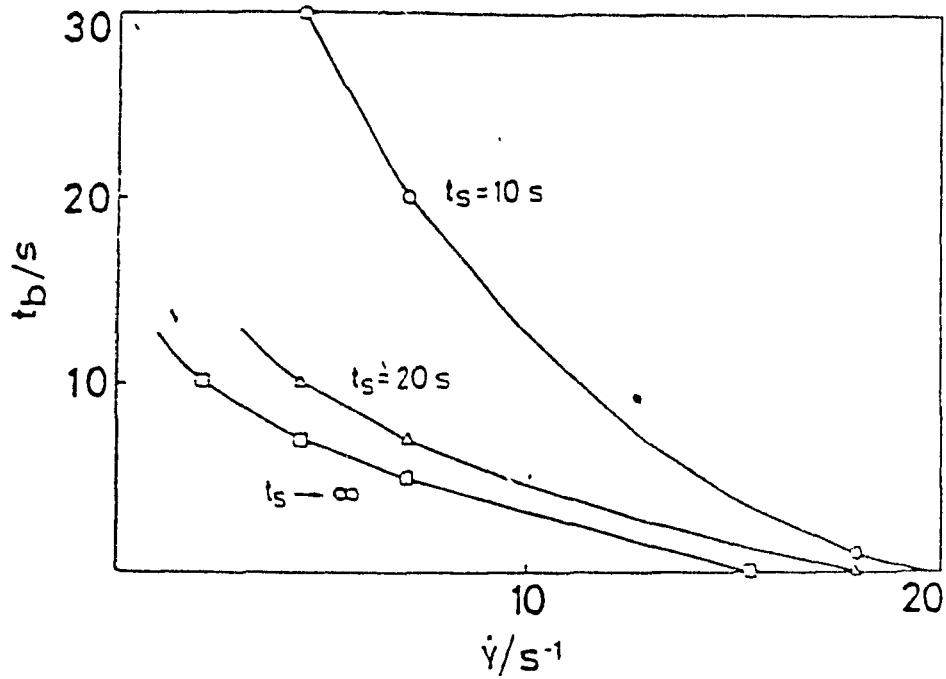


Figure 3.13. Experimentally determined dependence of the time for banded texture formation  $t_b$  on the prior shear rate  $\dot{\gamma}$ .  $t_s$  is the prior shearing time. (Reprinted from Marsano *et al.* [57].)

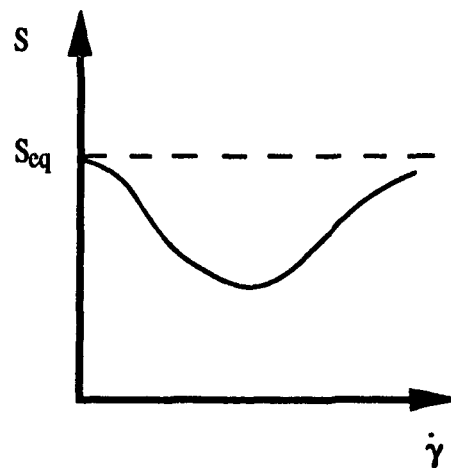


Figure 3.14. Schematic representation of the dependence of the scalar order parameter  $S$  on the shear rate  $\dot{\gamma}$  during shear flow.  $S_{eq}$  is the equilibrium value of  $S$ .

Figure 3.15 shows the dependence of  $\phi_m$  on  $S_0$  with  $A_S$  as the parameter. The results in this figure are used to explain the phenomenon that the contrast of the banded texture increases with increasing prior  $\dot{\gamma}$  or  $t_s$ . Examples of the contrast differentials are shown in Figure 3.16 for  $A_S = 0.108$  and (a)  $S_0 = 0.35$ , (b)  $S_0 = 0.55$  and (c)  $S_0 = 0.75$  at  $t = 14.3$  s, and in Figure 3.17 for  $S_0 = 0.75$  and (a)  $A_S = 0.080$ , (b)  $A_S = 0.095$  and (c)  $A_S = 0.108$  at  $t = 14.3$  s. It is noted that the contrast of the banded texture increases with  $S_0$  and  $A_S$ , which is consistent with the established fact that  $S_0$  is taken as  $\dot{\gamma}$  and the hypothesized fact that  $A_S$  is taken as  $t_s$ . It has been established that the stored free energy increases with either  $S_0$  or  $A_S$  through the  $L_2$  terms in equation (1.25), and that the system dissipates this energy through periodic director rotation and viscous backflow. To counter any increases in  $S$  (or, equivalently,  $S_0$ ) or  $\nabla S$  (or, equivalently,  $A_S$ ) in these  $L_2$  terms,  $\mathbf{n}$  rotates more away from the prior flow direction (or, equivalently, the magnitude of  $\phi_m$  increases). Consequently, the magnitude of  $\mathbf{n} \cdot \nabla S$  decreases, and by equation (3.12) the relative intensity (or, equivalently, contrast) increases.

Figure 3.18 shows the dependence of  $V_{y,m}^*$  on  $S_0$  with  $A_S$  as the parameter. The results in this figure are consistent with the fact that stronger (or more) director rotations produce stronger backflows. Figure 3.19 shows the dependence of the time to reach  $\phi_m$  ( $t_{\phi_m}$ ) on  $S_0$  with  $A_S$  as the parameter. Since backflow reduces the constraint for director rotation [72], it is then expected that for a given  $A_S$ ,  $t_{\phi_m}$  decreases as  $V_{y,m}^*$  increases.

### 3.4 Summary and Concluding Remarks

This chapter examined numerically the consequences that a spatially periodic scalar order parameter variation have on the relaxation phenomena after cessation of shear flow for the typical nematic polymer DDA9. The study was concentrated on the effects that the amplitude ( $A_S$ ) and base value ( $S_0$ ) of the initial periodic  $S$  spatial variation have on the time for pattern formation ( $t_b$ ) and the maximum planar director orientation ( $\phi_m$ ) in this pattern. The Ericksen and Landau-de Gennes continuum theories were used for this purpose. A plausible mechanism has been developed for the long sought causes of the formation of the mysterious and ubiquitous banded textures that nematic polymers exhibit between crossed polars after cessation of shear flow. The explanation for this nearly two decade old problem has been developed into a model, which was extensively studied.

The conclusions from this chapter are as follow:

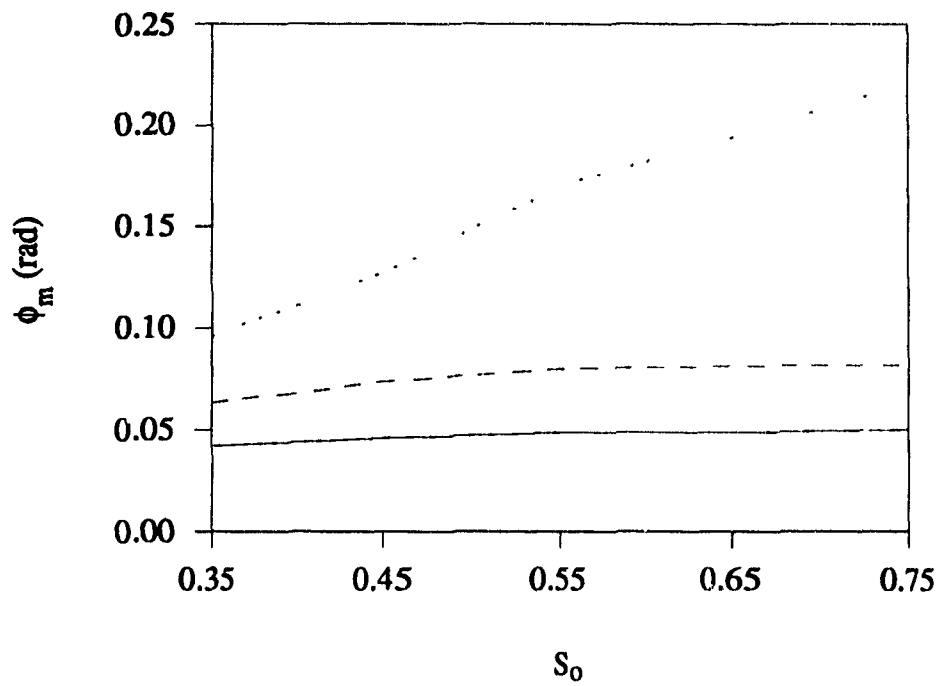


Figure 3.15. Maximum planar orientation angle  $\phi_m$  as a function of the base value of the initial periodic scalar order parameter spatial variation  $S_0$ . The amplitudes of the periodic variation are:  $A_S = 0.080$  ( ——— ),  $A_S = 0.095$  ( - - - - ) and  $A_S = 0.108$  ( ····· ).

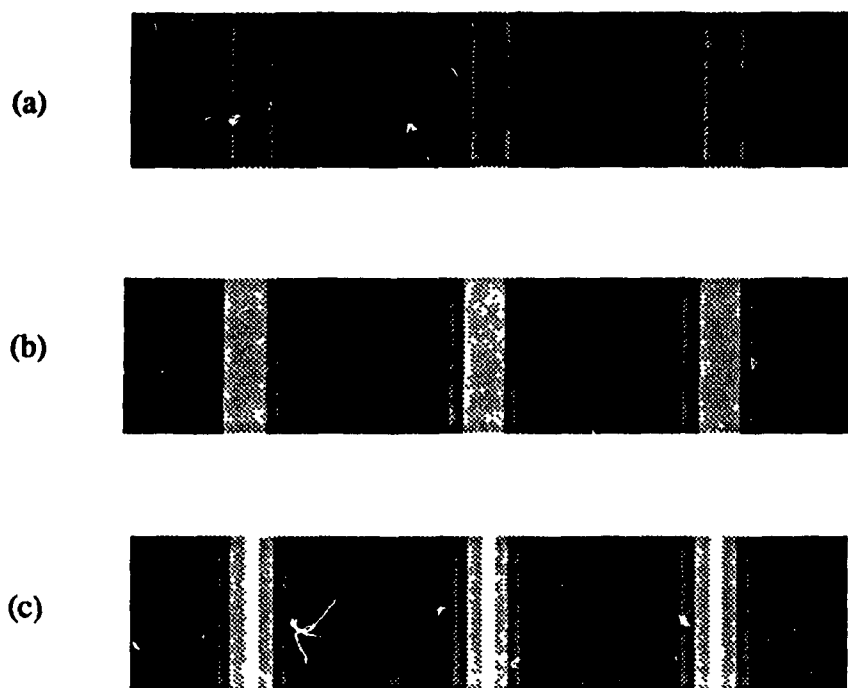


Figure 3.16. Digitized optical light patterns representing the patterns seen between crossed polars for the director fields at  $t = 14.3$  s. The amplitude of the initial periodic scalar order parameter variation is  $A_S = 0.108$ , and the base values of the variation are: (a)  $S_0 = 0.35$ , (b)  $S_0 = 0.55$  and (c)  $S_0 = 0.75$ . The relative maximum intensity is white and the relative minimum is black.

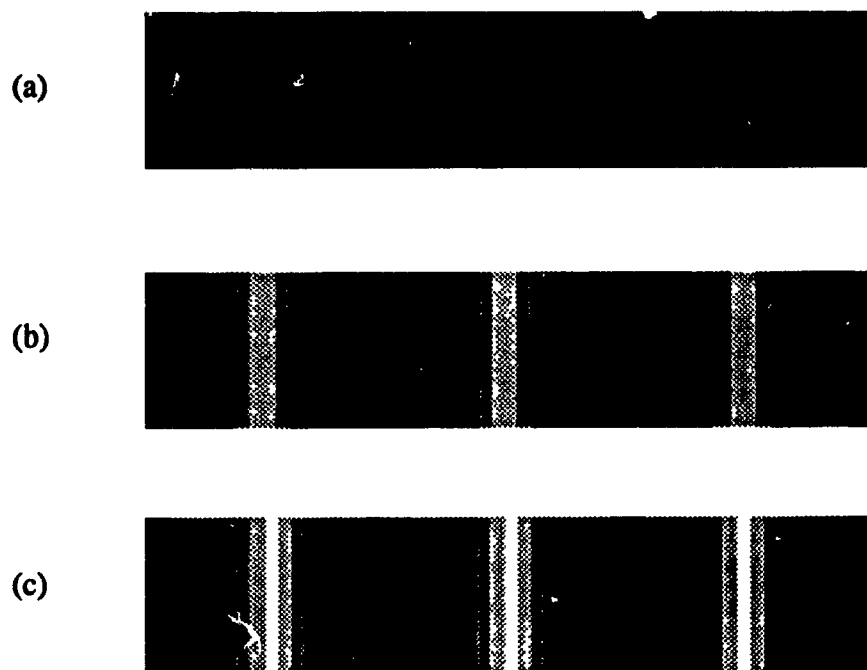


Figure 3.17. Digitized optical light patterns representing the patterns seen between crossed polars for the director fields at  $t = 14.3$  s. The base value of the initial periodic scalar order parameter variation is  $S_0 = 0.75$ , and the amplitudes of the variation are: (a)  $A_S = 0.080$ , (b)  $A_S = 0.095$  and (c)  $A_S = 0.108$ . The relative maximum intensity is white and the relative minimum is black.

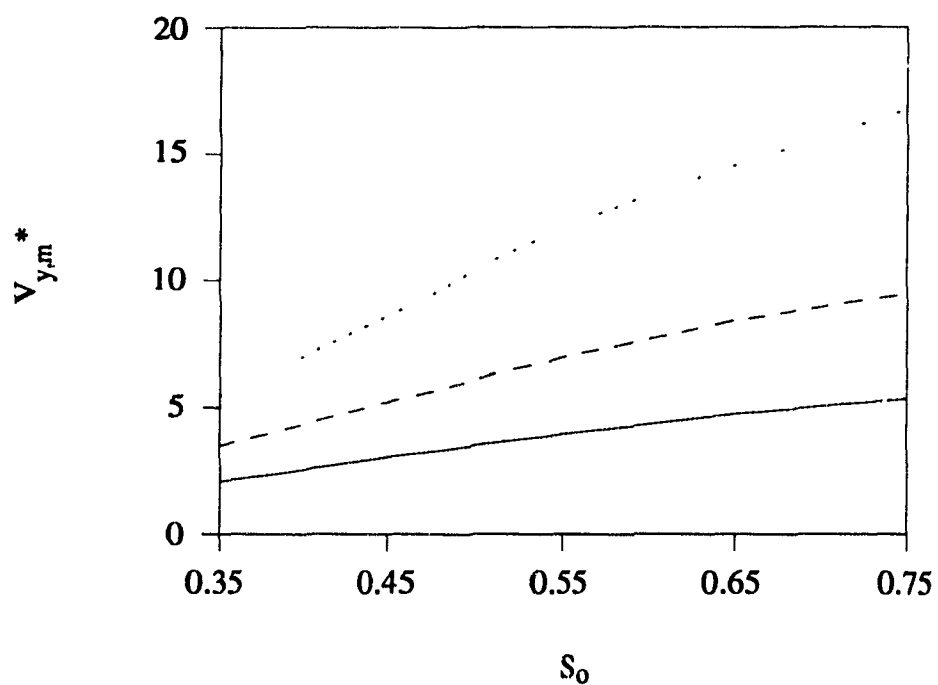


Figure 3.18. Maximum dimensionless velocity  $V_{y,m}^*$  as a function of the base value of the initial periodic scalar order parameter spatial variation  $S_0$ . The amplitudes of the periodic variation are:  $A_S = 0.080$  (—),  $A_S = 0.095$  (---) and  $A_S = 0.108$  (···).

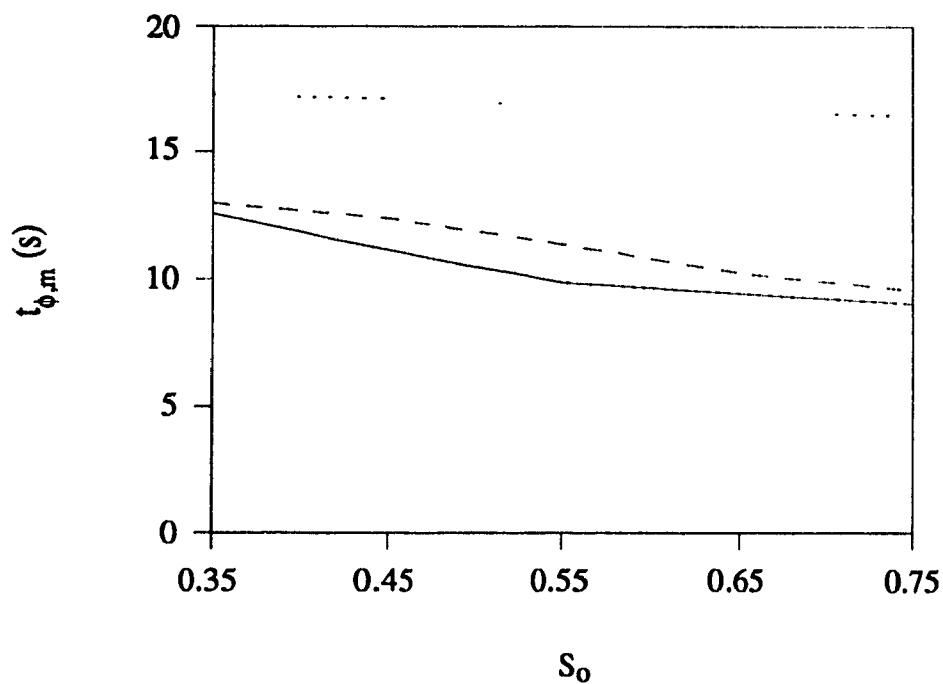


Figure 3.19. Time to reach the maximum planar orientation angle  $t_{\phi,m}$  as a function of the base value of the initial periodic scalar order parameter spatial variation  $S_0$ . The amplitudes of the periodic variation are:  $A_S = 0.080$  (—),  $A_S = 0.095$  (---) and  $A_S = 0.108$  (·····).

(1) The relaxation of stored elastic free energy due to periodic spatial variations in the scalar order parameter results in a transient periodic distortion of the director field, such that a banded texture is seen when the sample is viewed between crossed polars. Since any spatial variations in  $S$  due to shear flow relaxes very quickly in conventional nematic phases [30], these materials do not exhibit the banded texture after cessation of shear flow.

(2) The banded texture formed is energetically unstable.

(3) The wavelength of the periodic director pattern exhibiting the banded texture after cessation of shear flow optimizes the effects due to viscous flow and elasticity

(4) The power spectrums for the optimal wavelength, a shorter wavelength and a longer wavelength show that the director response is different for each wavelength. The optimal wavelength has the most number of modes.

(5) The following commonly reported experimental observations are explained by noting that the base value  $S_0$  of the initial periodic  $S$  spatial variation varies with the prior shear rate  $\dot{\gamma}$  and hypothesizing that the amplitude  $A_S$  of this variation varies with the prior shearing time  $t_s$ :

- (a) the time for banded texture formation  $t_b$  decreases as  $\dot{\gamma}$  or  $t_s$  increases, and
- (b) the contrast of the banded texture increases as  $\dot{\gamma}$  or  $t_s$  increases.

The relaxation phenomena exhibit these observations in response to the fact that the free energy increases as  $\dot{\gamma}$  or  $t_s$  increases.

## **Chapter 4**

### **Thesis Summary, Conclusions and Recommendations**

This final chapter is divided into three sections. The first section gives an overall summary of this thesis. The second section gives the conclusions to this thesis. Thirdly, the last section presents recommendations on further work that can be done on the subject matter contained in this thesis.

#### **4.1 Thesis Summary**

Nematic polymers are a new class of high performance materials. Since the invention of Kevlar nearly two decades ago, they have been replacing conventional materials in many applications. For example, they are used to manufacture bullet proof vests and pressure vessels. The main reason that these novel materials are gaining wide and popular usage is that they can have excellent mechanical properties if processed correctly. Shear flow deformations, such as in the injection molding of three dimensional objects, are invariably a part of nematic polymer processing. During these deformations, the molecules are highly aligned along the shear flow direction; it is this shear flow-induced molecular orientation that gives these materials their superior mechanical properties. In addition, however, once the flow has stopped and heat treatment has begun, the shear flow-induced molecular orientation decays away slowly. Consequently, the manufactured products will not have the desired excellent mechanical properties.

Therefore, it is of utmost importance to understand the relaxation phenomena of nematic polymers after cessation of shear flow in order to manufacture products from nematic polymers with superior mechanical properties. This was the goal of this thesis.

Chapter 1 presented briefly the fundamentals of liquid crystal physics that were needed in this thesis. This included the definition of liquid crystalline phases, orientational order, several nematic continuum theories, orientational slip, and liquid crystal optics. In addition, it contained a thorough description of the mysterious banded texture that nematic polymers exhibit when observed between crossed polars after cessation of shear flow.

Chapter 2 studied numerically the relaxation phenomena after cessation of simple shear flow for the typical nematic polymer PBG using the Leslie-Ericksen continuum theory and the Euler-Lagrange equation for surface motion. The major assumption made in this chapter was that the scalar order parameter  $S(\mathbf{x},t) = 1$ . This study was concentrated on the consequences that the surface conditions (i.e., surface viscosity  $\lambda^S$ ), defects (i.e., surface irregularities) and backflow (i.e., the director reorientation-induced transverse velocity  $V_y$ ) had on the director orientational relaxation time ( $\tau_\theta$  and  $\tau_\phi$ ) and equilibrium orientation ( $\theta_{eq}$  and  $\phi_{eq}$ ). Predictions from this chapter were thoroughly discussed, and concluded to be physically consistent.

The numerical study in Chapter 3 was on the relaxation phenomena and pattern formation after cessation of shear flow for the typical nematic polymer DDA9. This time, however, the more general Ericksen and Landau-de Gennes nematic continuum theories were used, and  $S = S(\mathbf{x},t)$ . In addition, this study examined specifically the effects that the base value  $S_0$  and amplitude  $A_S$  of an initial scalar order parameter  $S$  periodic spatial variation have on the time for pattern formation  $t_b$  and the maximum planar director orientation  $\phi_m$  in the resulting transient periodic director configuration. Results from this chapter were thoroughly discussed, and shown to be able to describe the cause and kinetics of the puzzling transient banded texture that nematic polymers exhibit when observed between crossed polars after cessation of shear flow.

## 4.2 Conclusions

### Chapter 2:

(1.1) The director reorientation induced-backflow relaxes the constraint for director rotation; the rotational viscosity is replaced by a lower effective one. Consequently, the

rate of director reorientation increases. Backflow, however, does not affect the equilibrium director field.

(1.2) The presence of surface disclinations along the width of the plates prevents the equilibrium director orientation from lying within the prior shear plane. At a given  $\lambda^S$ , the planar orientation angle relaxation time  $\tau_\phi$  decreases and the equilibrium planar orientation angle  $\phi_{eq}$  increases with increasing number of surface disclinations.

(2) A macroscopic wall slip model has been developed, implemented and solved to describe the transient nematic polymer orientation.  $\tau_\theta$ ,  $\tau_\phi$ ,  $\theta_{eq}$  and  $\phi_{eq}$  have been shown to vary with  $\lambda^S$ .

### Chapter 3:

(3) A model that studies the effects of S on nematic polymer orientation after cessation of shear flow has been developed, implemented and solved.

(4.1) The relaxation of stored elastic free energy due to periodic spatial variations in S results in a transient periodic distortion of the director field, such that a banded texture is seen when the sample is viewed between crossed polars. The wavelength of the periodic director configuration exhibiting the banded texture has been shown to optimize the effects due to elasticity and viscous flow.

(4.2) The banded texture was shown to be energetically unstable.

(5.1) Low molecular weight nematic phases do not exhibit the banded texture after cessation of shear flow, because any shear flow-effected S spatial variations relaxes very quickly in these phases.

(5.2) The following commonly reported experimental observations have been explained:

- (a) the time for banded texture formation  $t_b$  decreases as the prior shear rate  $\dot{\gamma}$  or prior shearing time  $t_s$  increases, and
- (b) the contrast of the banded texture increases as  $\dot{\gamma}$  or  $t_s$  increases.

The relaxation phenomena exhibit these observations in response to an increase in the free energy as  $\dot{\gamma}$  or  $t_s$  increases.

### 4.3 Recommendations

The model outlined in Chapter 3 contained many simplifying assumptions. Nevertheless, since this is the first known study on the relaxation phenomena of nematic polymers after cessation of shear flow, these assumptions were warranted. The following recommendations are offered for further work in the subject area of this thesis:

- (1) The simplifying assumption that the viscosities are not dependent on  $S$  should be removed.
- (2) The assumption that there is no variation in the thickness direction (i.e.,  $\frac{\partial(*)}{\partial z} = 0$ ) should be removed. By doing so, orientational slip can be incorporated into the model to better reflect the physics of the system.
- (3) The tilt angle  $\theta$  should be included in the model. Hence, the *serpentine sinusoidal* director configuration can be predicted from this model instead of simply a *sinusoidal* one. Furthermore, by doing this, the two velocities  $V_x$  and  $V_z$  must be included in the model.
- (4) The general flow problem of nematic polymers should be solved; i.e., the assumption of a spatially invariant and monodomain system ought to be lifted. This would give the director configuration during shear flow, and, consequently, the initial state of the system before it starts to decay (i.e., the relaxation phenomena).

## References

1. J.G. Aston, Physics and Chemistry of the Organic Solid State, edited by D. Fox, M.M. Labes and A. Weissberger, Interscience Publication, New York, Volume 1, Chapter 9, 1963.
2. G.W. Gray, Molecular Structure and the Properties of Liquid Crystals, Academic Press, New York, 1962.
3. G. Friedel, *Ann. Phys.*, **18**, 273 (1922).
4. S. Chandrasekhar and G.S. Ranganath, *Adv. Phys.*, **35**, 507 (1986).
5. P.J. Wojtowicz, Introduction to Liquid Crystals, edited by E.B. Priestley, P.J. Wojtowicz and P. Sheng, Plenum Press, New York, Chapter 3, 1974.
6. S. Jen, N.A. Clark, P.S. Pershan and E.B. Priestley, *Phys. Rev. Lett.*, **31**, 1552 (1973).
7. P. Sheng and E.B. Priestley, Introduction to Liquid Crystals, edited by E.B. Priestley, P.J. Wojtowicz and P. Sheng, Plenum Press, New York, Chapter 10, 1974.
8. C.W. Oseen, *Trans. Faraday Soc.*, **29**, 883 (1933).
9. H. Zocher, *Trans. Faraday Soc.*, **29**, 945 (1933).
10. R.C. Frank, *Discuss. Faraday Soc.*, **25**, 19 (1958).
11. J.L. Ericksen, *Arch. Rat. Mech. Anal.*, **23**, 266 (1966).
12. P. Sheng, Introduction to Liquid Crystals, edited by E.B. Priestley, P.J. Wojtowicz and P. Sheng, Plenum Press, New York, Chapter 8, 1974.
13. G. Srager, S. Fraden and R.B. Meyer, *Phys. Rev. A*, **39**, 4828 (1989).
14. P.G. de Gennes, The Physics of Liquid Crystals, Clarendon Press, Oxford, 1974.
15. R.G. Larson, Constitutive Equations for Polymer Melts and Solutions, Butterworths,

Boston, 1988.

16. V. Freedericksz and V. Zolina, *Trans. Faraday Soc.*, **29**, 919 (1933).
17. A.D. Rey, *Macromolecules*, **24**, 4450 (1991).
18. W.J.A. Goossens, *Mol. Cryst. Liq. Cryst.*, **124**, 305 (1985).
19. G. Vertogen and W.H. de Jeu, *Thermotropic Liquid Crystals. Fundamentals*, Springer-Verlag, New York, 1988.
20. R.B. Meyer, *Polymer Liquid Crystals*, edited by A. Ciferri, W.R. Krigbaum and R.B. Meyer, Academic Press, New York, Chapter 6 (1982).
21. C.R. Fincher, *Macromolecules*, **19**, 2431 (1986).
22. P.W. Morgan, *Macromolecules*, **10**, 1381 (1977).
23. M. Panar and L.F. Beste, *Macromolecules*, **10**, 1481 (1977).
24. M. Srinivasarao, Ph.D. Thesis, Department of Chemistry, Carnegie Mellon University, 1990.
25. V.G. Taratuta, G.M. Srajer and R.B. Meyer, *Mol. Cryst. Liq. Cryst.*, **116**, 245 (1985).
26. J.L. Ericksen, *Arch. Rat. Mech. Anal.*, **4**, 231 (1960).
27. J.L. Ericksen, *Trans. Soc. Rheol.*, **5**, 23 (1961).
28. F.M. Leslie, *Adv. Liq. Cryst.*, **4**, 1 (1979).
29. F.M. Leslie, *Phil. Trans. Soc. Lond.*, **A309**, 155 (1983).
30. G. Marrucci, *Liquid Crystallinity in Polymers: Principles and Fundamental Properties*, edited by A. Ciferri, VCH, New York, Chapter 11, 1991.
31. J.T. Jenkins, *Ann. Rev. Fluid. Mech.*, **10**, 197 (1978).
32. M. Doi and S.F. Edwards, *The Theory of Polymer Dynamics*, Oxford University, Oxford, 1986.
33. O. Parodi, *J. Phys.*, **31**, 581 (1970).
34. P.G. de Gennes, *Mol. Cryst. Liq. Cryst.*, **12**, 193 (1971).
35. R.G. Larson, *Macromolecules*, **23**, 3983 (1990).
36. Y. Farhoudi, Master Thesis, Dept. of Chemical Engineering, McGill University, 1992.
37. J.L. Ericksen, IMA Preprint Series No. 559 (1989).
38. B.J. Edwards, A.N. Beris and M. Grmela, *Mol. Cryst. Liq. Cryst.*, **201**, 51 (1991).
39. M. Born and E. Wolf, *Principles of Optics*, Pergamon Press, New York, 1980.
40. A.M. Donald, C. Viney and A.H. Windle, *Polymer*, **24**, 155 (1983).
41. C. Viney, A.M. Donald and A.H. Windle, *J. Mat. Sci.*, **18**, 1136 (1983).
42. C. Viney, A.M. Donald and A.H. Windle, *Polymer*, **26**, 870 (1985).
43. A.M. Donald and A.H. Windle, *J. Mat. Sci. Lett.*, **4**, 58, (1985).
44. G. Kiss and R.S. Porter, *Mol. Cryst. Liq. Cryst.*, **60**, 267 (1980).
45. G. Kiss and R.S. Porter, *J. Polym. Sci. Polym. Phys. Ed.*, **18**, 361 (1980).

46. M. Laus, A.S. Angeloni, P. Ferruti, G. Galli and E. Chiellini, *J. Polym. Sci. Polym. Lett. Ed.*, **22**, 587 (1984).
47. S. Chen, Y. Jin, R. Qian and L. Cai, *Makromol. Chem.*, **188**, 2713 (1987).
48. M. Kyotani and H. Kanetsuna, *J. Macromol. Sci.-Phys.*, **B26(3)**, 325 (1982).
49. Y. Nishio, T. Yamane and T. Takahashi, *J. Polym. Sci. Polym. Phys. Ed.*, **23**, 1943 (1985).
50. Y. Nishio, T. Yamane and T. Takahashi, *J. Polym. Sci. Polym. Phys. Ed.*, **23**, 1953 (1985).
51. P. Navard and A.E. Zachariades, *J. Polym. Sci. Polym. Phys.*, **25**, 1089 (1987).
52. A.E. Zachariades, P. Navard and J.P. Logan, *Mol. Cryst. Liq. Cryst.*, **110**, 93 (1984).
53. P. Navard, *J. Polym. Sci. Polym. Phys. Ed.*, **24**, 435 (1986).
54. B. Ernst and P. Navard, *Macromolecules*, **22**, 1419 (1989).
55. E. Peuvrel and P. Navard, *Macromolecules*, **24**, 5683 (1991).
56. E. Marsano, L. Carpaneto and A. Ciferri, *Mol. Cryst. Liq. Cryst.*, **158**, 267 (1988).
57. E. Marsano, L. Carpaneto, A. Ciferri and Y. Wu, *Liq. Cryst.*, **3**, 1561 (1988).
58. E. Marsano, L. Carpaneto and A. Ciferri, *Mol. Cryst. Liq. Cryst.*, **177**, 93 (1989).
59. G. Marrucci, N. Grizzuti and A. Buonauro, *Mol. Cryst. Liq. Cryst.*, **153**, 263 (1987).
60. P.L. Maffettone, N. Grizzuti and G. Marrucci, *Liq. Cryst.*, **4**, 385 (1989).
61. C.R. Fincher, *Mol. Cryst. Liq. Cryst.*, **155**, 559 (1988).
62. M. Horio, S. Ishikawa, K. Oda, *U.S.-Japan Seminar on Polymer Liquid Crystals*, Interscience Publication, New York, pages 269-292, 1985.
63. N.H. Hartshorne, *The Microscopy of Liquid Crystals*, Microscopic Publications, Chicago, 1974.
64. J.L. White, *U.S.-Japan Seminar on Polymer Liquid Crystals*, Interscience Publication, New York, pages 241-267, 1985.
65. Z. Tadmor and C. Gogos, *Principles of Polymer Processing*, John Wiley, New York, 1979.
66. A. Saupe, *Mol. Cryst. Liq. Cryst.*, **7**, 59 (1969).
67. Theorist <sup>TM</sup>, Prescience Corporation, San Francisco, Version 1.01, 1989.
68. C.A.J. Fletcher, *Computational Galerkin Methods*, Springer-Verlag, New York, 1984.
69. L. Lapidus and G. Pinder, *Numerical Solution of Partial Differential Equations in Science and Engineering*, John Wiley, New York, 1982.
70. J.P. Holman, *Experimental Methods for Engineers*, McGraw Hill, New York, 1984.
71. P.K. Currie and F.M. Leslie, *Arch. R. Mech.*, **87**, 35 (1984).
72. F. Brochard, *Mol. Cryst. Liq. Cryst.*, **23**, 51 (1973).
73. A.F. Martins, P. Esnault and F. Volino, *Phys. Rev. Lett.*, **57**, 1745 (1986).

74. J.H. Maddocks, Theory and Applications of Liquid Crystals, edited by J.L. Ericksen and D. Kinderlehrer, Springer-Verlag, New York, pages 255-269, 1987.
75. R.B. Meyer, F. Longberg, V. Taratuta, S. Fraden, S.-D. Lee and A.J. Hurd, *Faraday Discuss. Chem. Soc.*, **79**, 125 (1985).
76. A. Ciferri, Polymer Liquid Crystals, edited by A. Ciferri, W.R. Krigbaum and R.B. Meyer, Academic Press, New York, Chapter 3 (1982).
77. T.M. Nicholson, *Mol. Cryst. Liq. Cryst.*, **177**, 163 (1989).
78. M.F. Schiehel and K. Fahrenschon, *Appl. Phys. Lett.*, **19**, 391 (1971).
79. F. Longberg, S. Fraden, A.J. Hurd and R.B. Meyer, *Phys. Rev. Lett.*, **52**, 1903 (1984).
80. W.H. Press, B.P. Flannery, S. Teukolsky and W.T. Vetterling, Numerical Recipes, Cambridge University Press, Cambridge, 1985.
81. G.L. Baker and J.P. Gollub, Chaotic Dynamics: An Introduction, Cambridge University Press, Cambridge, 1990.
82. MATLAB™, The MathWorks Inc., South Natick, MA, Version 1.2a, 1989.

## Appendix A

### Equations for Chapter 2

The viscosity functions  $\{\eta_i\}$ ,  $i = 1, \dots, 23$ , in equation (2.4) are defined as follow:

$$\eta_1 = \alpha_2 \sin^2 \theta - \gamma_2 \sin^2 \theta \sin^2 \phi \quad (\text{A.1a})$$

$$\eta_2 = \frac{1}{4} \gamma_2 \sin(2\phi) \sin(2\theta) \quad (\text{A.1b})$$

$$\eta_3 = -\gamma_2 \sin(2\phi) \sin^2 \theta \quad (\text{A.1c})$$

$$\eta_4 = \frac{1}{2} \gamma_2 \sin(2\theta) \cos(2\phi) \quad (\text{A.1d})$$

$$\eta_5 = -\alpha_3 \sin(2\theta) + \gamma_2 \cos^2 \phi \sin(2\theta) \quad (\text{A.1e})$$

$$\eta_6 = \frac{1}{2} \gamma_2 \sin(2\phi) \cos(2\theta) \quad (\text{A.1f})$$

$$\eta_7 = \frac{1}{2} \alpha_2 \cos \phi \sin(2\theta) \quad (\text{A.1g})$$

$$\eta_8 = -\alpha_3 \sin \phi + \gamma_2 \sin \phi \cos^2 \theta \quad (\text{A.1h})$$

$$\eta_9 = -\frac{1}{2} \alpha_2 \sin(2\theta) \sin \phi \quad (\text{A.1i})$$

$$\eta_{10} = -\alpha_3 \cos \phi + \gamma_2 \cos \phi \cos^2 \theta \quad (\text{A.1j})$$

$$\eta_{11} = \alpha_2 \cos \phi \cos(2\theta) \quad (\text{A.1k})$$

$$\eta_{12} = -\gamma_2 \sin(2\theta) \sin \phi \quad (\text{A.1l})$$

$$\eta_{13} = \frac{1}{4} \alpha_1 \sin^2(2\phi) \sin^4 \theta - \gamma_2 \sin^2 \theta \cos^2 \phi + \frac{1}{2} (\alpha_3 + \alpha_6) \sin^2 \theta + \frac{1}{2} \alpha_4 \quad (\text{A.1m})$$

$$\eta_{14} = \alpha_1 \sin \phi \sin(2\phi) \cos \theta \sin^3 \theta + \frac{1}{2} (\alpha_5 - \alpha_2) \cos \phi \sin(2\theta) \quad (\text{A.1n})$$

$$\eta_{15} = \frac{1}{2} \alpha_1 \sin(4\phi) \sin^4 \theta + \gamma_2 \sin(2\phi) \sin^2 \theta \quad (\text{A.1o})$$

$$\eta_{16} = -\alpha_1 \cos \theta \sin \phi \sin^3 \theta + \frac{3}{2} \alpha_1 \cos \phi \sin(2\phi) \cos \theta \sin^3 \theta + \frac{1}{4} (\alpha_2 - \alpha_5) \sin(2\theta) \sin \phi \quad (\text{A.1p})$$

$$\eta_{17} = \alpha_1 \sin^2(2\phi) \cos \theta \sin^3 \theta - \gamma_2 \cos^2 \phi \sin(2\theta) + \frac{1}{2} (\alpha_3 + \alpha_6) \sin(2\theta) \quad (\text{A.1q})$$

$$\eta_{18} = -\frac{1}{2} \alpha_1 \sin(2\phi) \sin \phi \sin^4 \theta + \frac{3}{8} \alpha_1 \sin(2\phi) \sin \phi \sin^2(2\theta) + \frac{1}{2} (\alpha_5 - \alpha_2) \cos \phi \cos(2\theta) \quad (\text{A.1r})$$

$$\eta_{19} = \frac{1}{4} \alpha_1 \sin^2(2\theta) \sin^2 \phi + \frac{1}{2} (\alpha_5 - \alpha_2) \cos^2 \theta + \frac{1}{2} (\alpha_3 + \alpha_6) \sin^2 \phi \sin^2 \theta + \frac{1}{2} \alpha_4 \quad (\text{A.1s})$$

$$\eta_{20} = \frac{3}{2} \alpha_1 \cos \phi \sin(2\phi) \cos \theta \sin^3 \theta - \alpha_1 \cos \theta \sin \phi \sin^3 \theta + \frac{1}{4} (\alpha_2 - \alpha_5) \sin(2\theta) \sin \phi \quad (\text{A.1t})$$

$$\eta_{21} = \frac{1}{4} \alpha_1 \sin(2\phi) \sin^2(2\theta) + \frac{1}{2} (\alpha_3 + \alpha_6) \sin(2\phi) \sin^2 \theta \quad (\text{A.1u})$$

$$\eta_{22} = -\frac{1}{2}\alpha_1 \sin(2\phi) \sin\phi \sin^2\theta + \frac{1}{2}\alpha_1 \sin\phi \sin(2\phi) \sin^2(2\theta) + \frac{1}{2}(\alpha_5 - \alpha_2) \cos\phi \cos(2\theta) \quad (\text{A.1v})$$

$$\eta_{23} = \frac{1}{2}\alpha_1 \sin(4\theta) \sin^2\phi + \frac{1}{2}(\alpha_2 - \alpha_5) \sin(2\theta) + \frac{1}{2}(\alpha_3 + \alpha_6) \sin(2\theta) \sin^2\phi \quad (\text{A.1w})$$

The elastic functions  $\{\kappa_i\}$ ,  $i = 1, \dots, 29$ , and viscosity functions  $\{\eta_i\}$ ,  $i = 24, \dots, 30$ , in equations (2.5) and (2.6) are defined as follow:

$$\kappa_1 = -\frac{1}{2}K_{11} \cos\phi \sin(2\theta) + 2(K_{22} - K_{33}) \cos\phi \cos\theta \sin^3\theta + \frac{3}{2}(K_{33} - K_{22}) \sin(2\phi) \cos\theta \sin^3\theta \sin\phi \quad (\text{A.2a})$$

$$\kappa_2 = -\frac{1}{2}K_{11} \sin(2\theta) \sin\phi + \frac{1}{2}(K_{22} - K_{33}) \cos\phi \sin(2\phi) \cos\theta \sin^3\theta \quad (\text{A.2b})$$

$$\kappa_3 = \frac{1}{2}(K_{11} - K_{22}) \sin(2\phi) \sin^2\theta + \frac{1}{4}(K_{22} - K_{33}) \sin(2\phi) \sin^2(2\theta) \quad (\text{A.2c})$$

$$\kappa_4 = (K_{33} - 2K_{22}) \cos\phi \cos\theta \sin^3\theta - K_{33} \cos\phi \cos^3\theta \sin\theta \quad (\text{A.2d})$$

$$\kappa_5 = -\frac{1}{2}K_{22} \sin(2\theta) \sin\phi + (K_{22} - K_{33}) \cos^3\theta \sin\phi \sin\theta \quad (\text{A.2e})$$

$$\kappa_6 = \frac{1}{2}(K_{33} - K_{11}) \cos\phi \sin(2\theta) + \frac{1}{2}(K_{22} - K_{33}) \sin(2\phi) \sin(2\theta) \sin\phi \quad (\text{A.2f})$$

$$\kappa_7 = (K_{11} - K_{33}) \cos\phi \cos^2\theta + \frac{1}{2}(K_{22} - K_{33}) \sin(2\phi) \sin^2\theta \sin\phi + K_{33} \cos\phi \quad (\text{A.2g})$$

$$\kappa_8 = (K_{33} - \frac{1}{2}K_{22} - \frac{1}{2}K_{11}) \cos^2\phi \sin(2\theta) + \frac{1}{2}(K_{22} - K_{11}) \sin(2\theta) \quad (\text{A.2h})$$

$$\kappa_9 = \frac{1}{2}(K_{11} - K_{33}) \cos\phi \sin(2\theta) \quad (\text{A.2i})$$

$$\kappa_{10} = (K_{11} - K_{33}) \cos\phi \sin^2\theta + K_{33} \cos\phi \quad (\text{A.2j})$$

$$\kappa_{11} = (K_{11} - 2K_{22} + K_{33}) \cos^2\phi \sin^2\theta + \frac{5}{4}(K_{22} - K_{33}) \cos^2\phi \sin^2(2\theta) + \frac{1}{4}(K_{33} - K_{22}) \sin^2(2\theta) \quad (\text{A.2k})$$

$$\kappa_{12} = -2 K_{11} \cos^2 \theta \sin \phi + (K_{22} - K_{33}) \cos \phi \sin (2\phi) \sin^2 \theta + \frac{1}{2} (K_{22} - K_{33}) \cos \phi \sin (2\phi) \sin^2 (2\theta) \quad (\text{A.2l})$$

$$\kappa_{13} = \frac{1}{4} (K_{11} + 3 K_{22} - K_{33}) \sin (2\phi) \sin (2\theta) + \frac{1}{2} (K_{33} - 4 K_{22}) \sin (2\phi) \cos \theta \sin^3 \theta - \frac{3}{2} K_{33} \sin (2\phi) \cos^3 \theta \sin \theta \quad (\text{A.2m})$$

$$\kappa_{14} = \frac{1}{4} (K_{11} - K_{22}) \sin (2\phi) \sin (2\theta) + 2 (K_{22} - K_{33}) \sin (2\phi) \cos^3 \theta \sin \theta \quad (\text{A.2n})$$

$$\kappa_{15} = -2 K_{33} \cos^2 \theta \sin \phi + (K_{33} - K_{22}) \sin \phi \sin^2 (2\theta) \quad (\text{A.2o})$$

$$\kappa_{16} = (K_{33} - K_{11}) \cos^2 \theta + (K_{11} - K_{33}) \cos^2 \phi \sin^2 \theta + 2 (K_{22} - K_{33}) \cos^2 \theta \sin^2 \phi \quad (\text{A.2p})$$

$$\kappa_{17} = \frac{1}{2} (K_{11} - K_{22}) \sin (2\phi) \sin^2 \theta + \frac{1}{2} (K_{22} - K_{33}) \sin (2\phi) \sin^4 \theta \quad (\text{A.2q})$$

$$\kappa_{18} = K_{33} \sin^2 \theta + (K_{11} - K_{33}) \sin^2 \phi \sin^2 \theta + \frac{1}{4} (K_{22} - K_{33}) \sin^2 (2\theta) \cos^2 \phi \quad (\text{A.2r})$$

$$\kappa_{19} = 2 (K_{33} - K_{22}) \cos \phi \cos \theta \sin^3 \theta \quad (\text{A.2s})$$

$$\kappa_{20} = K_{22} \sin^2 \theta + \frac{1}{4} (K_{33} - K_{22}) \sin^2 (2\theta) \quad (\text{A.2t})$$

$$\kappa_{21} = \frac{1}{2} (K_{33} + K_{11} - 2 K_{22}) \sin (2\phi) \sin^2 \theta \quad (\text{A.2u})$$

$$\kappa_{22} = \frac{1}{4} (K_{22} - K_{11}) \sin (2\phi) \sin (2\theta) \quad (\text{A.2v})$$

$$\kappa_{23} = (K_{11} - K_{22}) \sin \phi \sin^2 \theta \quad (\text{A.2w})$$

$$\kappa_{24} = (K_{22} - K_{33}) \cos \theta \sin \phi \sin^3 \theta \quad (\text{A.2x})$$

$$\kappa_{25} = K_{22} \sin (2\theta) + (K_{11} - K_{22}) \sin (2\theta) \sin^2 \phi + 4 (K_{33} - K_{22}) \cos^2 \phi \cos \theta \sin^3 \theta \quad (\text{A.2y})$$

$$\kappa_{26} = \frac{3}{4} (K_{33} - K_{22}) \cos \phi \sin^2 (2\theta) + (K_{22} - K_{33}) \cos \phi \sin^4 \theta \quad (\text{A.2z})$$

$$\kappa_{27} = (K_{22} - K_{33}) \cos \phi \sin^4 \theta + \frac{3}{4} (K_{33} - K_{22}) \sin^2 (2\theta) \cos \phi \quad (\text{A.2aa})$$

$$\kappa_{28} = K_{33} \sin (2\theta) + 4 (K_{22} - K_{33}) \sin^3 \theta \cos \theta \quad (\text{A.2bb})$$

$$\kappa_{29} = \frac{1}{2} (K_{11} - 2 K_{22} + K_{33}) \sin (2\theta) \sin \phi \quad (\text{A.2cc})$$

$$\eta_{24} = \gamma_1 \cos \phi \quad (\text{A.2dd})$$

$$\eta_{25} = \frac{1}{2} \gamma_1 \sin (2\theta) \sin \phi \quad (\text{A.2ee})$$

$$\eta_{26} = -\frac{1}{4} (\gamma_1 + \gamma_2) \sin \phi \sin (2\theta) \quad (\text{A.2ff})$$

$$\eta_{27} = \frac{1}{4} (\gamma_1 + \gamma_2) \sin (2\phi) \sin^2 \theta \quad (\text{A.2gg})$$

$$\eta_{28} = \gamma_1 \sin^2 \theta \quad (\text{A.2hh})$$

$$\eta_{29} = \frac{1}{2} \gamma_1 \sin^2 \theta - \frac{1}{2} \gamma_2 \cos (2\phi) \sin^2 \theta \quad (\text{A.2ii})$$

$$\eta_{30} = \frac{1}{4} (\gamma_1 - \gamma_2) \cos \phi \sin (2\theta) \quad (\text{A.2jj})$$

The elastic functions  $\{ \kappa_i \}$ ,  $i = 30, \dots, 35$ , in equation (2.7) are defined as follow:

$$\kappa_{30} = K_{11} \sin^2 \theta + K_{33} \cos^2 \theta \quad (\text{A.3a})$$

$$\kappa_{31} = K_{11} \sin \phi \sin^2 \theta \quad (\text{A.3b})$$

$$\kappa_{32} = \frac{1}{2} (K_{33} - K_{11}) \cos \phi \sin (2\theta) \quad (\text{A.3c})$$

$$\kappa_{33} = K_{22} \sin^4 \theta + \frac{1}{4} K_{33} \sin^2 (2\theta) \quad (\text{A.3d})$$

$$\kappa_{34} = \frac{1}{2} (K_{33} - K_{22}) \sin^2 \theta \sin (2\theta) \cos \phi \quad (\text{A.3e})$$

$$\kappa_{35} = -K_{22} \sin^2 \theta \sin \phi \quad (\text{A.3f})$$

The dimensionless equations are obtained by scaling the elastic terms with  $K_{22}$ , the viscosity terms with  $|\gamma_2|$ , the distances  $x$  and  $z$  with  $h$ , the velocity with  $\frac{K_{22}}{|\gamma_2| h}$ , and the time with  $\frac{\gamma_1 h^2}{K_{22}}$ . By doing this, the angle-dependent viscosity and elastic functions become:  $\eta_i^* = \frac{\eta_i}{|\gamma_2|}$  and  $\kappa_i^* = \frac{\kappa_i}{K_{22}}$ . A superscript asterisk denotes a dimensionless variable. Equations (2.4) to (2.6) then become the following set of dimensionless nonlinear partial differential equations:

$$\begin{aligned}
0 = & \eta_1^* \frac{\partial}{\partial x^*} \frac{\partial \phi}{\partial t^*} + \eta_2^* \frac{\partial}{\partial x^*} \frac{\partial \theta}{\partial t^*} + \eta_3^* \frac{\partial \phi}{\partial x^*} \frac{\partial \phi}{\partial t^*} + \eta_4^* \frac{\partial \phi}{\partial x^*} \frac{\partial \theta}{\partial t^*} + \eta_5^* \frac{\partial \theta}{\partial x^*} \frac{\partial \phi}{\partial t^*} + \\
& \eta_6^* \frac{\partial \theta}{\partial x^*} \frac{\partial \theta}{\partial t^*} + \eta_7^* \frac{\partial}{\partial z^*} \frac{\partial \phi}{\partial t^*} + \eta_8^* \frac{\partial}{\partial z^*} \frac{\partial \theta}{\partial t^*} + \eta_9^* \frac{\partial \phi}{\partial z^*} \frac{\partial \phi}{\partial t^*} + \\
& \eta_{10}^* \frac{\partial \phi}{\partial z^*} \frac{\partial \theta}{\partial t^*} + \eta_{11}^* \frac{\partial \theta}{\partial z^*} \frac{\partial \phi}{\partial t^*} + \eta_{12}^* \frac{\partial \theta}{\partial t^*} \frac{\partial \theta}{\partial z^*} + \eta_{13}^* \frac{\partial}{\partial x^*} \frac{\partial \partial V_y^*}{\partial x^*} + \\
& \eta_{14}^* \frac{\partial}{\partial x^*} \frac{\partial \partial V_y^*}{\partial z^*} + \eta_{15}^* \frac{\partial \partial V_y^*}{\partial x^*} \frac{\partial \phi}{\partial x^*} + \eta_{16}^* \frac{\partial \partial V_y^*}{\partial z^*} \frac{\partial \phi}{\partial x^*} + \eta_{17}^* \frac{\partial \partial V_y^*}{\partial x^*} \frac{\partial \theta}{\partial x^*} + \\
& \eta_{18}^* \frac{\partial \partial V_y^*}{\partial z^*} \frac{\partial \theta}{\partial x^*} + \eta_{19}^* \frac{\partial}{\partial z^*} \frac{\partial \partial V_y^*}{\partial z^*} + \eta_{20}^* \frac{\partial \partial V_y^*}{\partial x^*} \frac{\partial \phi}{\partial z^*} + \\
& \eta_{21}^* \frac{\partial \partial V_y^*}{\partial z^*} \frac{\partial \phi}{\partial z^*} + \eta_{22}^* \frac{\partial \partial V_y^*}{\partial x^*} \frac{\partial \theta}{\partial z^*} + \eta_{23}^* \frac{\partial \partial V_y^*}{\partial z^*} \frac{\partial \theta}{\partial z^*} +
\end{aligned} \tag{A.4a}$$

$$\begin{aligned}
\eta_{24}^* \frac{\partial \theta}{\partial t^*} = & \kappa_1^* \left( \frac{\partial \phi}{\partial x^*} \right)^2 + \kappa_2^* \frac{\partial}{\partial x^*} \frac{\partial \phi}{\partial x^*} + \kappa_3^* \frac{\partial}{\partial x^*} \frac{\partial \phi}{\partial z^*} + \kappa_4^* \left( \frac{\partial \phi}{\partial z^*} \right)^2 + \\
& \kappa_5^* \frac{\partial}{\partial z^*} \frac{\partial \phi}{\partial z^*} + \kappa_6^* \left( \frac{\partial \theta}{\partial x^*} \right)^2 + \kappa_7^* \frac{\partial}{\partial x^*} \frac{\partial \theta}{\partial x^*} + \kappa_8^* \frac{\partial}{\partial x^*} \frac{\partial \theta}{\partial z^*} + \\
& \kappa_9^* \left( \frac{\partial \theta}{\partial z^*} \right)^2 + \kappa_{10}^* \frac{\partial}{\partial z^*} \frac{\partial \theta}{\partial z^*} + \kappa_{11}^* \frac{\partial \phi}{\partial x^*} \frac{\partial \phi}{\partial z^*} + \kappa_{12}^* \frac{\partial \phi}{\partial x^*} \frac{\partial \theta}{\partial x^*} + \\
& \kappa_{13}^* \frac{\partial \phi}{\partial z^*} \frac{\partial \theta}{\partial x^*} + \kappa_{14}^* \frac{\partial \phi}{\partial x^*} \frac{\partial \theta}{\partial z^*} + \kappa_{15}^* \frac{\partial \phi}{\partial z^*} \frac{\partial \theta}{\partial z^*} + \\
& \kappa_{16}^* \frac{\partial \theta}{\partial x^*} \frac{\partial \theta}{\partial z^*} + \eta_{25}^* \frac{\partial \phi}{\partial t^*} + \eta_{26}^* \frac{\partial \partial V_y^*}{\partial x^*} + \eta_{27}^* \frac{\partial \partial V_y^*}{\partial z^*}
\end{aligned} \tag{A.4b}$$

$$\begin{aligned}
\eta_{28}^* \frac{\partial \phi}{\partial t^*} = & \kappa_{17}^* \left( \frac{\partial \phi}{\partial x^*} \right)^2 + \kappa_{18}^* \frac{\partial}{\partial x^*} \frac{\partial \phi}{\partial x^*} + \kappa_{19}^* \frac{\partial}{\partial x^*} \frac{\partial \phi}{\partial z^*} + \kappa_{20}^* \frac{\partial}{\partial z^*} \frac{\partial \phi}{\partial z^*} + \\
& \kappa_{21}^* \left( \frac{\partial \theta}{\partial x^*} \right)^2 + \kappa_{22}^* \frac{\partial}{\partial x^*} \frac{\partial \theta}{\partial x^*} + \kappa_{23}^* \frac{\partial}{\partial x^*} \frac{\partial \theta}{\partial z^*} + \kappa_{24}^* \frac{\partial \phi}{\partial x^*} \frac{\partial \phi}{\partial z^*} + \\
& \kappa_{25}^* \frac{\partial \phi}{\partial x^*} \frac{\partial \theta}{\partial x^*} + \kappa_{26}^* \frac{\partial \phi}{\partial z^*} \frac{\partial \theta}{\partial x^*} + \kappa_{27}^* \frac{\partial \phi}{\partial x^*} \frac{\partial \theta}{\partial z^*} + \kappa_{28}^* \frac{\partial \phi}{\partial z^*} \frac{\partial \theta}{\partial z^*} + \\
& \kappa_{29}^* \frac{\partial \theta}{\partial x^*} \frac{\partial \theta}{\partial z^*} + \eta_{29}^* \frac{\partial V_y^*}{\partial x^*} + \eta_{30}^* \frac{\partial V_y^*}{\partial z^*}
\end{aligned} \tag{A.4c}$$

Furthermore, the dimensionless initial and boundary conditions are as follow:

$$\theta = \theta_i(x^*, z^*) \text{ at } t^* = 0, 0 \leq x^* \leq 1.5, 0 \leq z^* \leq 1 \tag{A.5a}$$

$$\phi = \phi_i(x^*, z^*) \text{ at } t^* = 0, 0 \leq x^* \leq 1.5, 0 \leq z^* \leq 1 \tag{A.5b}$$

$$V_y^* = 0 \text{ at } t^* = 0, 0 \leq x^* \leq 1.5, 0 \leq z^* \leq 1 \tag{A.5c}$$

$$\frac{\partial \theta}{\partial x^*} = 0 \text{ at } t^* > 0, x^* = 0, 0 \leq z^* \leq 1 \tag{A.5d}$$

$$\frac{\partial \theta}{\partial x^*} = 0 \text{ at } t^* > 0, x^* = 1.5, 0 \leq z^* \leq 1 \tag{A.5e}$$

$$\frac{\partial \phi}{\partial x^*} = 0 \text{ at } t^* > 0, x^* = 0, 0 \leq z^* \leq 1 \tag{A.5f}$$

$$\frac{\partial \phi}{\partial x^*} = 0 \text{ at } t^* > 0, x^* = 1.5, 0 \leq z^* \leq 1 \tag{A.5g}$$

$$V_y^* = 0 \text{ at } t^* > 0, x^* = 0, 0 \leq z^* \leq 1 \tag{A.5h}$$

$$V_y^* = 0 \text{ at } t^* > 0, x^* = 1.5, 0 \leq z^* \leq 1 \tag{A.5i}$$

$$-2\lambda^s \frac{\partial \theta}{\partial t^*} = \kappa_{30}^* \frac{\partial \theta}{\partial z^*} + \kappa_{31}^* \frac{\partial \phi}{\partial x^*} + \kappa_{32}^* \frac{\partial \theta}{\partial x^*} \text{ at } t^* > 0, 0 \leq x^* \leq 1.5, z^* = 0 \tag{A.5j}$$

$$2 \lambda^{s*} \frac{\partial \theta}{\partial t^*} = \kappa_{30}^* \frac{\partial \theta}{\partial z^*} + \kappa_{31}^* \frac{\partial \phi}{\partial x^*} + \kappa_{32}^* \frac{\partial \theta}{\partial x^*} \text{ at } t^* > 0, 0 \leq x^* \leq 1.5, z^* = 1 \quad (\text{A.5k})$$

$$-2 \lambda^{s*} \frac{\partial \phi}{\partial t^*} \sin^2 \theta = \kappa_{33}^* \frac{\partial \phi}{\partial z^*} + \kappa_{34}^* \frac{\partial \phi}{\partial x^*} + \kappa_{35}^* \frac{\partial \theta}{\partial x^*} \text{ at } t^* > 0, \quad (\text{A.5l})$$

$$0 \leq x^* \leq 1.5, z^* = 0$$

$$2 \lambda^{s*} \frac{\partial \phi}{\partial t^*} \sin^2 \theta = \kappa_{33}^* \frac{\partial \phi}{\partial z^*} + \kappa_{34}^* \frac{\partial \phi}{\partial x^*} + \kappa_{35}^* \frac{\partial \theta}{\partial x^*} \text{ at } t^* > 0, \quad (\text{A.5m})$$

$$0 \leq x^* \leq 1.5, z^* = 1$$

$$V_y^* = 0 \text{ at } t^* > 0, 0 \leq x^* \leq 1.5, z^* = 0 \quad (\text{A.5n})$$

$$V_y^* = 0 \text{ at } t^* > 0, 0 \leq x^* \leq 1.5, z^* = 1 \quad (\text{A.5o})$$

## Appendix B

### Equations for Chapter 3

The relations for the dependence of the Leslie viscosities on the scalar order parameter  $S$  are as follow [38]:

$$\alpha_1^S = \beta_1^m S^2 \cdot \frac{(\gamma_2^S)^2}{\gamma_1^S} + \frac{(\beta_1^S)^2}{\beta_2^S} \quad (\text{B.1a})$$

$$\alpha_2^S = \frac{1}{2} (\gamma_2^S - \gamma_1^S) \quad (\text{B.1b})$$

$$\alpha_3^S = \frac{1}{2} (\gamma_1^S + \gamma_2^S) \quad (\text{B.1c})$$

$$\alpha_4^S = \beta_4^m + \frac{2}{3} \beta_2^m (1 - S) + \frac{2}{9} \beta_3^m (1 - S)^2 + \frac{1}{9} \beta_1^m (1 - S)^2 \quad (\text{B.1d})$$

$$\alpha_5^S = \frac{1}{3} \beta_1^m S (1 - S) + \beta_2^m S + \alpha_2^S \frac{\gamma_2^S}{\gamma_1^S} \quad (\text{B.1e})$$

$$\alpha_6^S = \gamma_2^S + \alpha_5^S \quad (\text{B.1f})$$

where

$$\beta_2^S = -\frac{(\alpha_2 - \alpha_3)}{(3 + 6S^2)} \quad (\text{B.1g})$$

$$\beta_1^S = -\beta_2^S \frac{(\alpha_2 + \alpha_3)}{(\alpha_2 - \alpha_3)} (2S + 1) (1 - S) \quad (\text{B.1h})$$

$$\gamma_1^S = -S^2 (\alpha_2 - \alpha_3) \quad (\text{B.1i})$$

$$\gamma_2^S = -\gamma_1^S \frac{(\alpha_2 + \alpha_3)(2 + S)}{(\alpha_2 - \alpha_3) 3S} \quad (\text{B.1j})$$

$$\beta_1^m = \alpha_1 + \alpha_2 - \alpha_3 + 4 \frac{\alpha_2 \alpha_3}{(\alpha_2 - \alpha_3)} \quad (\text{B.1k})$$

$$\beta_2^m = \frac{1}{2} \alpha_2 \quad (\text{B.1l})$$

$$\beta_3^m = 2 \frac{\alpha_2 \alpha_3}{(\alpha_2 - \alpha_3)} + \frac{1}{2} (\alpha_2 + \alpha_5) \quad (\text{B.1m})$$

$$\beta_4^m = \alpha_4 \quad (\text{B.1n})$$

The viscosity functions  $\{ \eta_i \}$ ,  $i = 31, \dots, 34$ , in equation (3.5) are defined as follow:

$$\eta_{31} = \alpha_2 \cos^2 \phi - \alpha_3 \sin^2 \phi \quad (\text{B.2a})$$

$$\eta_{32} = -(\alpha_2 + \alpha_3) \sin(2\phi) \quad (\text{B.2b})$$

$$\eta_{33} = \frac{1}{2} \alpha_1 \sin(4\phi) + (\alpha_2 + \alpha_3) \sin(2\phi) \quad (\text{B.2c})$$

$$\eta_{34} = \frac{1}{4} \alpha_1 \sin^2(2\phi) + \frac{1}{2} (\alpha_5 + \alpha_4 - \alpha_2) \cos^2 \phi + \frac{1}{2} (\alpha_3 + \alpha_6 + \alpha_4) \sin^2 \phi \quad (\text{B.2d})$$

The elastic functions  $\{ \kappa_i \}$ ,  $i = 36, \dots, 44$ , and viscosity functions  $\{ \eta_i \}$ ,  $i = 35, \dots, 38$ , in equations (3.6) and (3.7) are defined as follow:

$$\kappa_{36} = -K S \quad (\text{B.3a})$$

$$\kappa_{37} = -\frac{1}{2} K S^2 \quad (\text{B.3b})$$

$$\kappa_{38} = \frac{1}{2} K_6 S \sin(2\phi) \quad (\text{B.3c})$$

$$\kappa_{39} = \frac{1}{2} K S \quad (\text{B.3d})$$

$$\kappa_{40} = -K_5 \quad (\text{B.3e})$$

$$\kappa_{41} = K_6 \sin(2\phi) \quad (\text{B.3f})$$

$$\kappa_{42} = -K_6 \cos^2 \phi \quad (\text{B.3g})$$

$$\kappa_{43} = K_6 S \cos(2\phi) \quad (\text{B.3h})$$

$$\kappa_{44} = \frac{1}{2} K_6 S \sin(2\phi) \quad (\text{B.3i})$$

$$\eta_{35} = -\gamma_1 \quad (\text{B.3j})$$

$$\eta_{36} = \frac{1}{2} [\gamma_2 \cos(2\phi) - \gamma_1] \quad (\text{B.3k})$$

$$\eta_{37} = -\beta_2 \quad (\text{B.3l})$$

$$\eta_{38} = \frac{1}{2} \beta_1 \sin(2\phi) \quad (\text{B.3m})$$

where the relations

$$K = 9 L_1 + \frac{9}{2} L_2 \quad (\text{B.3n})$$

$$K_5 = \frac{3}{2} L_1 + \frac{1}{4} L_2 \quad (\text{B.3o})$$

$$K_6 = \frac{3}{4} L_2 \quad (\text{B.3p})$$

have been used.

The dimensionless equations are obtained by scaling the elastic terms with  $K$ , the viscosity terms with  $\gamma_1$ , the length  $x$  with  $L$ , the velocity with  $\frac{K}{\gamma_1 L}$ , and the time with

$\frac{\gamma_1 L^2}{K}$ . By doing this, the angle-dependent viscosity and elastic functions become:  $\eta_i^* = \frac{\eta_i}{\gamma_1}$

and  $\kappa_i^* = \frac{\kappa_i}{K}$ . The superscript asterisk denotes a dimensionless variable. Equations (3.5)

to (3.7) then become the following set of dimensionless nonlinear partial differential equations:

$$0 = \eta_{31}^* \frac{\partial}{\partial x^*} \frac{\partial \phi}{\partial t^*} + \eta_{32}^* \frac{\partial \phi}{\partial x^*} \frac{\partial \phi}{\partial t^*} + \eta_{33}^* \frac{\partial \phi}{\partial x^*} \frac{\partial V_y^*}{\partial x^*} + \eta_{34}^* \frac{\partial}{\partial x^*} \frac{\partial V_y^*}{\partial x^*} \quad (\text{B.4a})$$

$$\eta_{35}^* \frac{\partial \phi}{\partial t^*} = \kappa_{36}^* \frac{\partial S}{\partial x^*} \frac{\partial \phi}{\partial x^*} + \kappa_{37}^* \frac{\partial}{\partial x^*} \frac{\partial \phi}{\partial x^*} + \kappa_{38}^* \frac{\partial}{\partial x^*} \frac{\partial S}{\partial x^*} + \eta_{36}^* \frac{\partial V_y^*}{\partial x^*} \quad (\text{B.4b})$$

$$\begin{aligned} \eta_{37}^* \frac{\partial S}{\partial t^*} = & \frac{\kappa_B \vartheta T L^2}{K} \left[ \left(1 - \frac{1}{3} U\right) S - \frac{1}{3} U S^2 + \frac{2}{3} U S^3 \right] + \kappa_{39}^* \left(\frac{\partial \phi}{\partial x^*}\right)^2 + \\ & \kappa_{40}^* \frac{\partial}{\partial x^*} \frac{\partial S}{\partial x^*} + \kappa_{41}^* \frac{\partial \phi}{\partial x^*} \frac{\partial S}{\partial x^*} + \kappa_{42}^* \frac{\partial}{\partial x^*} \frac{\partial S}{\partial x^*} + \kappa_{43}^* \left(\frac{\partial \phi}{\partial x^*}\right)^2 + \\ & \kappa_{44}^* \frac{\partial}{\partial x^*} \frac{\partial \phi}{\partial x^*} + \eta_{38}^* \frac{\partial V_y^*}{\partial x^*} \end{aligned} \quad (\text{B.4c})$$

Furthermore, the dimensionless initial and boundary conditions are as follow:

$$\phi = A_\phi \sin \left( \kappa_\phi^* \pi x^* + \frac{1}{2} \pi \right) \text{ at } t^* = 0, 0 \leq x^* \leq 1 \quad (\text{B.5a})$$

$$S = S_0 + A_S \sin \left( \kappa_S^* \pi x^* + \frac{1}{2} \pi \right) \text{ at } t^* = 0, 0 \leq x^* \leq 1 \quad (\text{B.5b})$$

$$V_y^* = 0 \text{ at } t^* = 0, 0 \leq x^* \leq 1 \quad (\text{B.5c})$$

$$\frac{\partial \phi}{\partial x^*} = 0 \text{ at } t^* > 0, x^* = 0 \quad (\text{B.5d})$$

$$\frac{\partial \phi}{\partial x^*} = 0 \text{ at } t^* > 0, x^* = 1 \quad (\text{B.5e})$$

$$\frac{\partial S}{\partial x^*} = 0 \text{ at } t^* > 0, x^* = 0 \quad (\text{B.5f})$$

$$\frac{\partial S}{\partial x^*} = 0 \text{ at } t^* > 0, x^* = 1 \quad (\text{B.5g})$$

$$V_{y^*} = 0 \text{ at } t^* > 0, x^* = 0 \quad (\text{B.5h})$$

$$V_{y^*} = 0 \text{ at } t^* > 0, x^* = 1 \quad (\text{B.5i})$$